Two-Dimensional Raman-THz Spectroscopy: a Novel Spectroscopic Tool for the Characterization of the Liquid Phase

Dissertation
zur
Erlangung der naturwissenschaftlichen Doktorwürde
(Dr. sc. nat.)

vorgelegt der
Mathematisch-naturwissenschaftlichen Fakultät
der
Universität Zürich

von
Gustavo Ciardi
aus
Italien

Promotionskommission
Prof. Dr. Peter Hamm (Vorsitz)
Prof. Dr. Jürg Hutter
Prof. Dr. Jürg Osterwalder

Zürich, 2019

List of Publications

- *Signatures of Intra- and Intermolecular Vibrational Coupling in Halogenated Liquids Revealed by Two-dimensional Raman-THz Spectroscopy.*

  Gustavo Ciardi, Arian Berger, Peter Hamm, Andrey Shalit

  The Journal of Physical Chemistry Letters (2019)

- *Impact of Nuclear Quantum Effects on the Structural Inhomogeneity of Liquid Water.*

  Arian Berger*, Gustavo Ciardi*, Peter Hamm, Andrey Shalit

  Proc. Natl. Acad. Sci. U. S. A. (2019)

  *the authors contributed equally to this work.

- *Aqueous Solvation from the Water Perspective.*

  Saima Ahmed, Andrea Pasti, Ricardo J. Fernandez Teràn, Gustavo Ciardi, Andrey Shalit, Peter Hamm.

  The Journal of Chemical Physics (2018)

Contents

List of Figures

Abstract

The spectral properties of liquids in the terahertz (THz) region play an important role in chemistry, as they reflect motions of large molecules and molecular complexes which, in turn, govern chemical reactivity and processes like solvation. This frequency regime is dominated by the weak and elusive *inter*molecular forces (hydrogen bonds, ion-dipole interactions), which interchange on ultrafast time scales. Despite the large amount of potential information present in the low frequency window (0-300 cm^{-1}), the proper extraction of these spectral signatures does not rely yet on solid spectroscopic tools, since 1D spectra (both in Raman and THz) turn out to be exceptionally blurred and indistinct.

In this work, we demonstrate the potential and the capabilities of two-dimensional Raman-THz spectroscopy to address and successfully disentangle properties like couplings and broadening mechanisms of the intra-/intermolecular modes. This novel spectroscopic technique is an extension of the concept of 2D spectroscopy in other frequency regimes (NMR, infrared, optical) to the THz frequency window.

Specifically, the inhomogeneity of the hydrogen bond networks in liquid water has been investigated in the context of the Nuclear Quantum effects (NQE). By measuring the THz photon echoes of different water isotpologues at different temperatures, we have shown that the extended echo components present in the 2D Raman-THz responses relate directly to the structural lifetime of the hydrogen bond networks. This observation, together with precious insights about the structure of water, proves that our technique can indeed distinguish between homogenous and inhomogeneous broadening, key

features of well established 2D techniques.

Another crucial aspect of multidimensional spectroscopies is the ability to identify couplings. To this end, we recorded the 2D Raman-THz responses of simple halogenated liquids, which serve as perfect model systems with their well-defined intramolecular modes. The spectra reveal cross peaks which we attribute to the coupling between the sharp intramolecular modes and the much broader intermolecular degrees of freedom of these solvents.

The information retrieved with 2D Raman-THz spectroscopy demonstrates the ability of our technique to grasp in detail the fundamental properties of the low-frequency spectra of liquids.

Chapter 1

Introduction

The properties of electromagnetic radiation that spans the frequency range from 0.1 to 10 terahertz (THz=10^{12} Hz, 3 cm^{-1} - 330 cm^{-1}, 3 mm-30 μm) and, in turn, the properties of materials that can be investigated with such light have drawn a lot of attention in recent years. This spectral region lies between the electronic regime of millimeter or microwave radiation and the photonic regime of optical/infrared light (Fig 1.1); this middle ground, where the development of technologies to emit, detect and manipulate THz light turns out to be quite challenging, is often referred as the *Terahertz gap*. Nevertheless, countless and fundamental properties of all the states of matter can be addressed in this frequency window such as collective modes in solids and liquids, rotational dynamics in gas phase and plasma dynamics. This is the reason why, in the past 20 years, THz technologies and its applications have developed significantly, trying to bridge the above-mentioned gap.

The energy of THz photons (4 meV at 1 THz) is too low to ionize atoms (in contrast, for example, to X-rays) and, as a consequence, damage biological tissues. At the same time, many materials that are usually opaque at optical and infrared frequencies are transparent to THz light as, for example, paper, plastics, and textiles. The unique combination of these properties makes such radiation really appealing, for example, for biomedical[9, 10] (tissue imaging, pharmaceutical quality control), security applications[11] (screening and detection of hidden threats and weapons) and conservation of historical

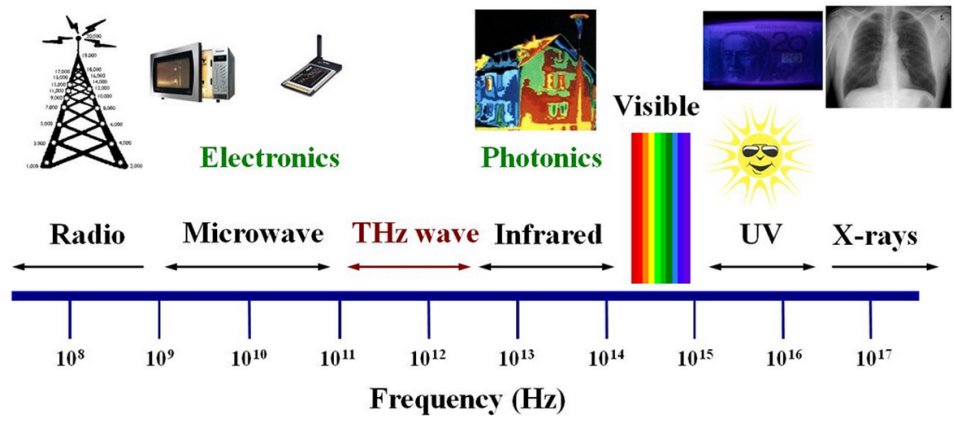

Figure 1.1: Differnt regions of the electromagnetic spectrum. Highlighted in red the frequency range spanned by THz radiation.

arts[12] (different composition of historical inks). The degree of applicability of THz technology goes together with the development of reliable and cost-effective sources that emit THz radiation and, consequently, with systems that can detect and make possible to perform spectroscopy with this radiation; at the current stage, however, the still significant technological limits of these devices do not allow yet THz science to go mainstream to the same extent as its electronic and photonic counterparts.

Obviously, all possible applications are based on the ability of retrieving some form of spectroscopic information from the investigated objects. For this reason, it is important to understand how THz spectroscopy works and spell out the specific information we can address when one performs such spectroscopy.

1.1 Linear Terahertz Spectroscopy and Raman spectroscopy

The advent of ultrafast laser sources and semiconductor science in the late 1980's set the stage for the development of THz time domain spectroscopy(THz-TDS)[13]. THz transients obtained by shining ultrashort laser pulses onto

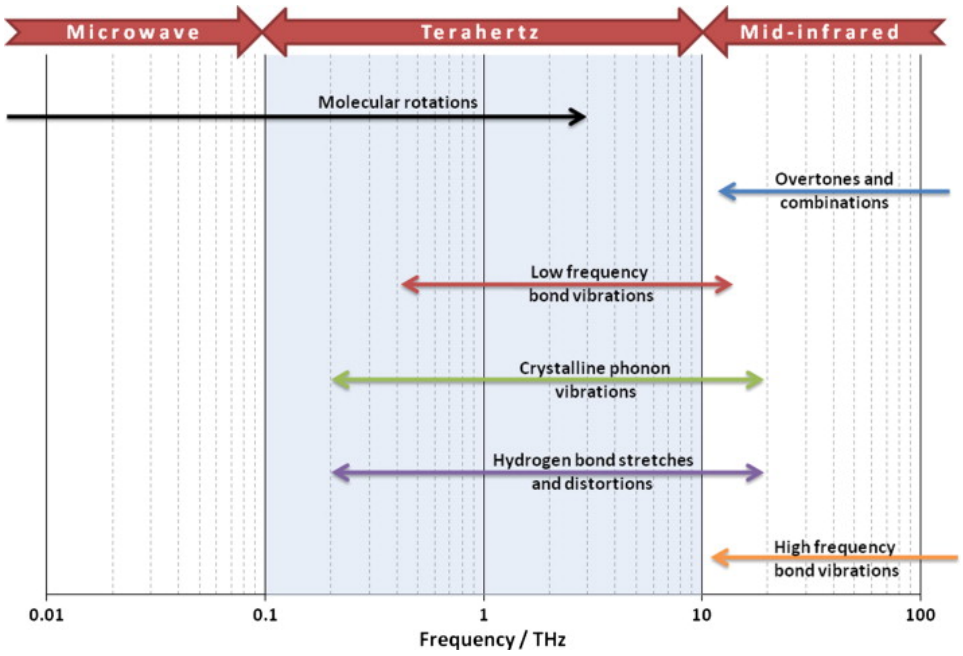

Figure 1.2: A summary of the properties of matter that can be addressed with THz light. Figure adapted from Ref [1].

nonlinear crystals and dipole antennas have enhanced and extended the accessibility to the low-frequency spectroscopic features of matter.

In the THz frequency window the electric field of a pulse can be fully characterized without the use of an interferometer, and the subpicosecond pulses allow time-resolved experiments with hundreds of femtosecond time resolution. The basic idea of THz-TDS is that THz radiation is focused on a sample and, subsequently, the reflected or transmitted light is sampled in the time domain. In these techniques, one can simultaneously reconstruct the amplitude and phase (and hence real and imaginary part of complex optical constants at each frequency component) of the detected THz waveform. The direct access to all this information, simultaneously, is one of the greatest advantages with respect to infrared or optical spectroscopy, where one measures only the intensity of the light.

Most of the accessible excitations in the THz region of the spectrum

are thermally populated degrees of freedom - k_BT at room temperature is $\sim$6 THz - which are responsible for many of the macroscopic properties in various systems. A great deal of spectroscopic features can be addressed with THz spectroscopy and Fig 1.2 displays the typical dynamics that one can learn about; for example, we have molecular rotations in gases[14, 15], semiconductor dynamics and phonon vibrations[16] and low-frequency bond vibrations in liquids[17, 18] and biological system[19]. The degree to which a THz pulse can perturb a system is directly related to the amplitude of the pulses' electric fields and to the ability of such a field to displace charges (i.e the transition dipole moment of the corresponding transitions). For example, low-lying delocalized electronic states in solids and optical phonons have very large transition dipole moments ($\sim$150 Debye) whereas the ones for liquids and gases are, generally, much smaller (3 to 4 orders of magnitude)[20].

In general, information about low-frequency modes in matter can be addressed "nonresonantly" also using optical and near infrared light sources through Raman interactions, specifically, with low-frequency Raman spectroscopy [21, 22]. Raman spectroscopy excites the sample with visible or near infrared light and takes advantage of virtual levels to access the vibrational level of a system. It consists on irradiating a sample with a monochromatic source to excite molecules to a virtual state from which they instantaneously relax back to a higher (Stokes scattering) or lower (anti-Stokes scattering) vibrational level, resulting in inelastic scattered light being lower or higher in frequency than the exciting photons, respectively. Even though removing intense Rayleigh scattering line was an issue, Raman scattering has been used extensively in the past[23, 8, 24] to study low-frequency properties of liquids, when the THz technology was not yet developed.

Spectroscopically, the specific type of information one measures with Raman and THz spectroscopy are, however, not exactly the same. Direct far-infrared excitations are sensitive to the change of the dipole moment whereas nonresonsant ones to the change in polarizability of the system, that is, it probes the Raman active modes. This means that, depending on the symmetries of the molecules, not all transition might be allowed for both type of excitations and strong bands in the IR spectrum of a compound

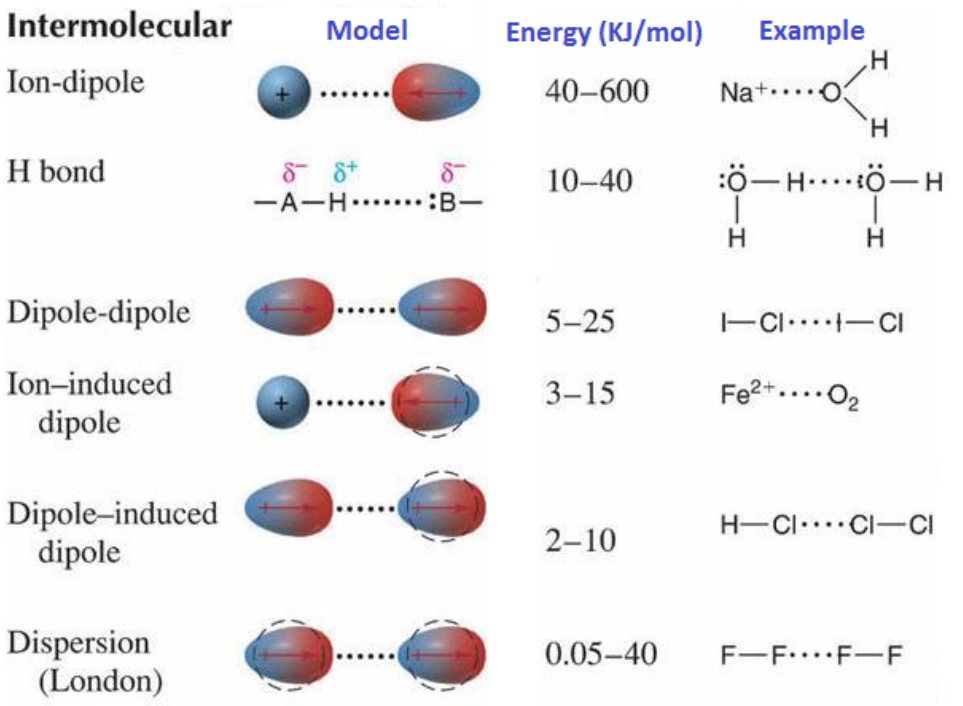

Figure 1.3: Summary of the various intermolecular forces in the liquid phase. Figure retrieved and adapted from the websitr `www.chem.fsu.edu/chemlab/chm1046course/interforces.html`

might correspond to weak bands in the Raman and vice versa.

In this work, we will be focusing, in detail, on the spectroscopic properties of liquids, taking advantage of both Raman and THz interactions.

1.1.1 Low-frequency interactions in liquids

A deep understanding of the liquid phase still poses a significant challenge to today's science. The properties of liquids lie somewhat in the middle between the ones of gases and solids, but closer to solids. The *inter*molecular forces, i.e. forces among different molecules - to be distinguished from the much stronger *intra*molecular forces - can be thought as the "glue" that holds molecules together. They determine many of the macroscopic bulk properties of the liquids such as, for example, boiling point and viscosity. In contrast

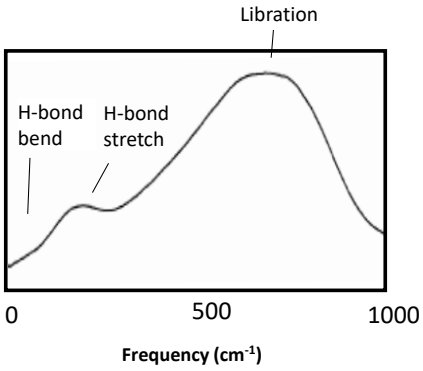

Figure 1.4: Low-frequency absorption spectrum of water. Figure adapted from Ref[2].

to solids, these interactions are more dynamic and happen on much shorter timescales in the case of liquids.

The nature of the intermolecular forces is mostly electrostatic and dispersive (van der Waals). They are the result of mutual interaction of charged species, and thus they exist between all molecules in the universe. Nonetheless, since Coulomb attraction and repulsion wears off as the distance increases, these forces are much more pronounced in liquids and solids where molecules are close together. A summary of the different type of intermolecular interactions in liquids is presented in Fig 1.3. In this list a special place is held by ion-dipole interactions and hydrogen bond; the reason for this is essentially twofold: first, they are the strongest in term of bond energies and second, they are crucial for the properties of water, the most important liquid on Earth. It is fair to say, that the reason why water plays a crucial role in all biological processes is mostly due to the interplay between the two above-mentioned intermolecular forces. The ability of hydrogen and oxygen atoms to form strong hydrogen bonds gives water an innumerable amount of anomalous macroscopic properties with respect to simple liquids, such as density maximum at 4°C, decreased viscosity under pressure and many others. Furthermore, the structure of proteins and DNA, their conformational changes, their biological activity and basically all the interaction with solvents are mediated by the intermolecular forces.

Raman and linear THz spectroscopy belong to the class of one dimensional spectroscopy, where the spectroscopic information is displayed on a single frequency axis. Normally, in one dimensional experimental spectra, due the ultrafast timescales at which the intermolecular forces exchange, the results of these interactions are seen as featureless, broad peaks in the range from $\sim$5-100 cm^{-1}(up to 600 cm^{-1} in the case of water and strongly hydrogen bonded systems) both in Raman[25, 26, 27] and linear THz spectroscopy[18, 17, 28]. This very fact can be clearly observed in the one dimensional THz spectrum of water in Fig 1.4. This is why, in order to resolve ambiguities about interpretation of these spectra, there is the need to thin out the information content onto additional frequency dimensions, with the help of multidimensional spectroscopy.

Chapter 2

Multidimensional spectroscopy

2.1 Concept of Two-Dimensional Spectroscopy

To set the stage, it is important to understand why it is beneficial to explore beyond one dimensional spectroscopy. In general, multidimensional spectroscopy can provide a wealth of spectroscopic information which is intrinsically missing in the lower rank 1D techniques[29]. It can help to distinguish between homogeneous and inhomogeneous line-broadening mechanisms of the interrogated transition, measure its anharmonicity and observe couplings among different transitions. Such couplings, whose signature are cross-peaks in a frequency-frequency correlation map, can reveal important structural information about spatial correlations of two coupled transitions. The first examples of multidimensional spectroscopies were developed in the field of Nuclear Magnetic Resonance (2D NMR)[30] and, subsequently, in the infrared spectral region (2D-IR)[31, 32, 33], investigating nuclear spins and intramolecular vibrations (down to $\sim$1000 cm^{-1}), respectively; nowadays, these experiments are well-established and routinely performed in many laboratories.

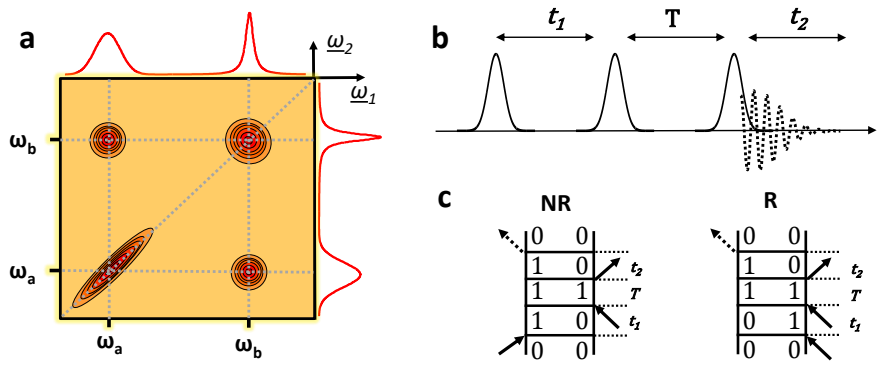

Figure 2.1: In (a) a schematic representation of a 2D spectrum. Panel (b) shows the typical pulse sequence (in black the excitation pulses and in red the emitted signal) and (c) examples of possible rephasing and non-rephasing Fyenman diagrams.

In the prototype 2D experiment in the IR or visible spectral range, three pulses (3-in-1-out) interact with the sample in a four wave mixing process[29], as depicted in Fig 2.1(b). The three pulses are separated by variable time delays: the first and the last (t_1 and t_2 in Fig 2.1) are called coherence times (since the system is in a coherence state) whereas the one between the second and the third pulse (T) is called population time. Taking the Fourier transform along t_1 and t_2, one can plot the resulting frequency-frequency two dimensional map where, in general, the signal will consist of diagonal and/or cross peaks. Many interesting properties can be revealed by looking at the frequency position of the peaks, their shape and their evolution during the population time T. Below, a summary of the insights one can learn about.

Diagonal Peaks:

- Homogeneous vs. Inhomogenous broadening
- Anharmonicities

Cross-peaks:

- Couplings
- Chemical exchange
- Energy transfer

In general, any four wave mixing process is a nonlinear light-matter

interaction based on a third-order optical nonlinearity[34]. This means that one addresses the 3-rd order susceptibility $\chi^{(3)}$ of the system:

$$P^{(3)} \propto \chi^{(3)} E_1 \cdot E_2 \cdot E_3 \tag{2.1}$$

where P is the macroscopic polarization created by the electric fields E_n of the incident laser pulses. The 3-rd order nonlinearity is the lowest order nonlinearity for isotropic media, such as liquids, since all even-order susceptibilities vanish.

A useful and compact representation of the possible pathways that a certain pulse sequence can induce on a system is given by the double sided Feynman diagrams(Fig 2.1(c)). The Feynman diagrams' language originates from the density matrix formalism and a perturbative expansion of the Liouville–von Neumann equation, which describe the time evolution of a particular system interacting with multiple laser pulses. A thorough discussion about these topics can be found at Ref[29]. The notations of the states in the diagram denote various levels of different modes of the system; time runs from bottom to top and the each line indicates the state in which the system is after an interaction with a laser pulse. Arrows represent the interaction with the electric field of the laser pulse; an arrow pointing towards the system represents a change to a higher-excited state and an arrow pointing away represents a change to a lower-excited state. The side of the diagram where the arrow appears relates to an interaction with the *ket*(left) or with the *bra*(right) of the systems' density matrix. The last interaction is connected with emission of the signal and always points away from the system. In principle, two kind of diagrams are possible, namely rephasing and non-rephasing diagrams. The former are related to a very important special case: the *photon echo* pulse sequence, which gives one the tool to disentangle homogeneous from inhomogeneous broadening. If we have an inhomogeneous set of oscillators (i.e. some oscillators which sit in a slightly different environment with respect to one another), the vibrational modes of such molecules will keep memory of the oscillation frequency for a certain time, ultimately the time at which the surrounding environment changes.

If we excite these molecules and they remember their oscillation frequency long enough, i.e. the environment does not rearrange in the time scale of the experiment, they will run out of phase after the first excitation during time t_1 but they may "rephase" as a result of the interaction with the second and third pulse and give rise to an echo whenever $t_1 = t_2$. Hence, rephasing diagrams, which describe the pathways leading to photon echoes, evidence the presence of inhomogeneous broadening in a system and can be visually distinguished by the non-rephasing ones by looking at the swap of sign of the coherences during time t_1 and t_2.

2.2 2D Spectroscopy in the low-frequency regime

The extension of the above mentioned concept to the far IR part of the electromagnetic spectrum (i.e. below 500 cm^{-1}) can be, in principle, realized either by means of 3-rd order THz techniques[35] (the low-frequency version of 2D IR) or by fifth-order(or seventh-order) Raman spectroscopy[36] where vibrational coherences are excited via pairs of two nonresonant field interactions. These two approaches are sensitive to the change of the dipole moment and polarizability of the system, respectively.

2.2.1 2D THz spectroscopy

Following the advances in the generation of tabletop strong THz pulses (with electric field up to ∼MV/cm) required for nonlinear interactions[37], 2D THz techniques have emerged, but their applicability is still currently limited to systems with very large transition dipole moments, like semiconductor solids[38, 39] and molecules in the gas phase[40]. To date, no 2D THz experiment of liquids has been realized. Fig 2.2 shows the pulse sequence for 2D THz experiments, equivalent to the one in Fig 2.1(b) with three input THz pulses and one emitted THz field[41].

Sometimes, in order to simplify the experimental setup, from the perspective of generation and recombination of multiple THz pulses, the second

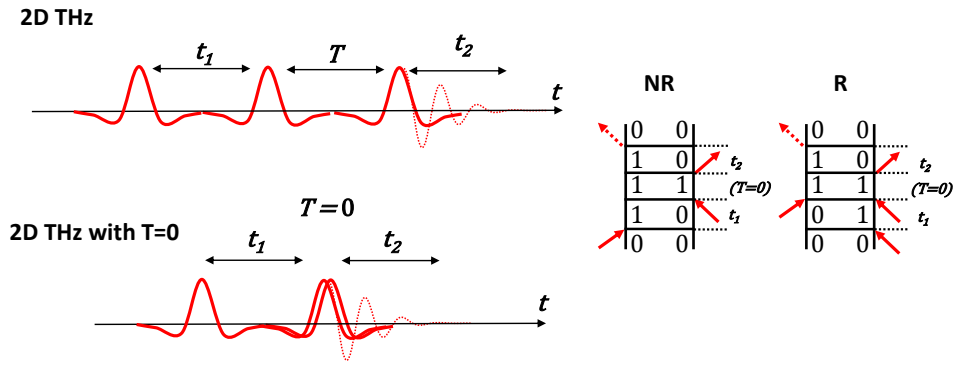

Figure 2.2: Pulse sequences for and 2D THz, the classical approach and the version without population time, and corresponding examples of Feynman diagrams.

and third field interactions are coming from one and the same laser pulse, forcing to zero the population time T. This simplification comes with the price of not being able to monitor processes like spectral diffusion or chemical exchange[42].

2.2.2 Raman-Echo and 2D Raman spectroscopy

To overcome the limited energies of available THz pulses, each resonant THz field interaction could be, in principle, exchanged with two nonresonant field interactions from a laser pulse in the VIS/NIR spectral range, which induces a Raman process. The Raman effect is, generally, weak but that might be overcompensated by the much higher available intensities of visible or near-infrared laser pulses. By replacing every single THz interaction with a pair of Raman interaction, one ends up with what is called Raman-Echo spectroscopy[43], based on a seventh-order nonlinear signal. Despite the incredible difficulty of this experiment, there have been attempts in literature to implement this scheme[44, 45]. In order to lower the high nonlinearity of the signal, Tanimura and Mukamel proposed 2D Raman spectroscopy[36], a version of the Raman-Echo spectroscopy with a one Raman process less

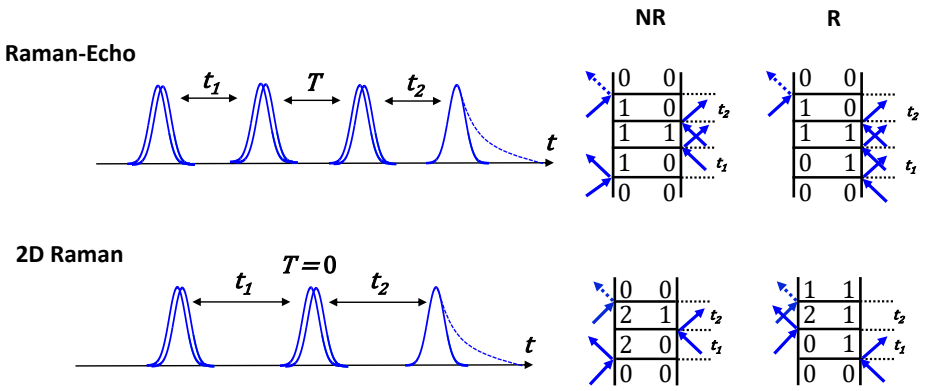

Figure 2.3: Pulse sequences for 2D Raman and Raman Echo spectroscopy and corresponding examples of Feynman diagrams.

with respect to Raman-Echo spectroscopy, consisting of three nonresonant interactions and thus based on a fifth-order signal, again with the population time T forced to zero. Despite the lower nonlinearity, 2D Raman spectroscopy turns out to be an exceptionally difficult experiment, due to the strong contamination from third-order cascading effects[46, 47, 48, 49, 50]. Only recently, schemes employing a pulse shaper have overcome this issue[51].

The 2-pulses-in-1-out approaches like 2D Raman and the version of 2D THz spectroscopy wiht $T = 0$ imply that one of the interactions must induce a two-quantum (or a zero-quantum) transition[42], which would be forbidden in the pure harmonic case. However, it reasonable to assume that this is not an issue in the case of the intermolecular modes of liquids which, presumably, bear quite large anharmonicities. In the Feynman diagrams shown in Fig 2.3, the two-quantum transition happen when a specific interactions forces a quantum number to increase more than one unit (for example the first interactions in the repahsing diagram of 2D Raman spectroscopy).

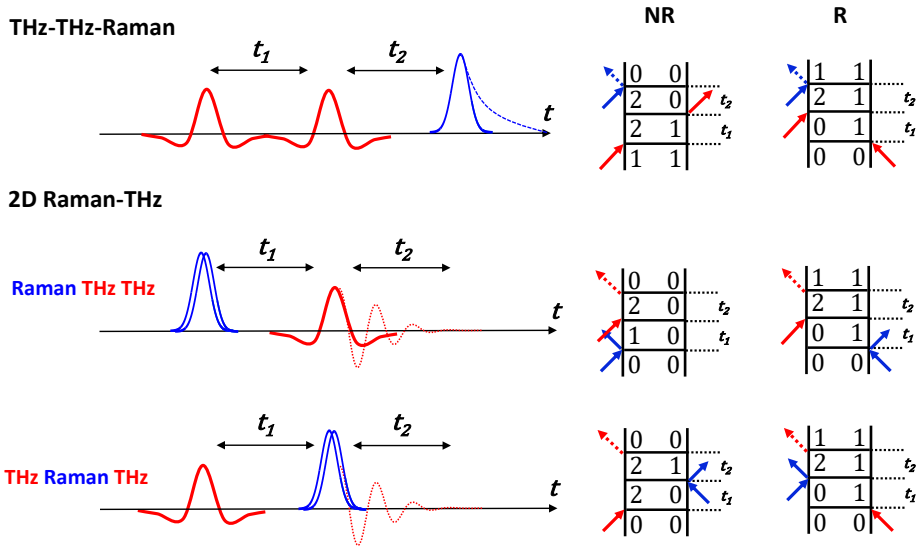

Figure 2.4: Pulse sequences for 2D Raman-THz and THz-THz-Raman spectroscopy and corresponding examples of possible Feynman diagrams.

2.2.3 Hybrid Raman-THz pulse sequences

The experimental challenges described for Raman and THz based 2D spectroscopy have set the stage for the development of experimental methods relying on hybrid pulse sequences, combining both Raman and THz excitations to generate the nonlinear signal[52]. Third-order based 2D-Raman-THz hybrid methods were theoretically proposed by Cho[53] and they encompass three different possible time orderings: THz-THz-Raman, Raman-THz-THz and THz-Raman-THz. As both dipole and polarizability interactions are comprised, the hybrid methods can provide increased sensitivity to study low-frequency vibrational modes and their interactions. The reasoning concerning the number of total input and output pulses spelled out in the previous paragraph applies to the same degree for hybrid pulse sequences with only two exciting pulses. Also here, one of the Raman or THz interaction must induce a two-quantum transition[42]. After having developed the theory[54], the

first experimental realization of hybrid Raman-THz spectroscopy came, quite recently, from our group[55, 54]. It is called 2D Raman-THz spectroscopy and it combines Raman and THz excitations to generate two distinct pulse sequences: Raman-THz-THz and THz-Raman-THz. Owing to the linear dependence on the applied THz electric field of the measured signal in 2D Raman-THz spectroscopy, one can employ spectrally broad THz pulses with weak electric fields. This new approach demonstrated the ability to report on the extent of inhomogeneity of low-frequency intermolecular modes of pure liquid water and in various salt solutions, providing a glance into the correlation between macroscopic viscosity and structuring of hydrogen-bond networks on the molecular level[4]. Later on, Blake and coworkers introduced the complementary THz-THz-Raman pulse sequence which originated from the THz-Kerr-effect[56, 57, 58, 59] by separating its nonlinear THz interaction into two pulses. They used that pulse sequence to study the couplings in halogenated liquids[60, 61], whose 1D spectrum shows sharp intramolecular modes in the range 1-10 THz.

2.3 Dissertation outline

A detailed description of 2D Raman-THz spectroscopy, together with the experiments that have been performed with it, are given in the next chapters. In particular, we will be focusing on two aspects which are schematically depicted in Fig 2.5; firstly, we will analyze the 2D Raman-THz response of water, and in particular the features that are connected to the previously described photon echo sequence, as function of temperature and isotope substitution. This comes as a continuation of previous works[55, 4] and will help to shed more light on the amount of inhomogeneity and the broadening mechanism of the modes (and hence the structure) of the hydrogen bond networks. On the left side of Fig 2.5, the low-frequency 1D infrared spectrum of liquid water and an exaggerated example of the different possible scenarios for the broadening mechanism of the low-frequency modes. If the collective hydrogen bond network were perfectly homogeneous system on the timescales of our experiment, ideally no photon echo would appear in the 2D response;

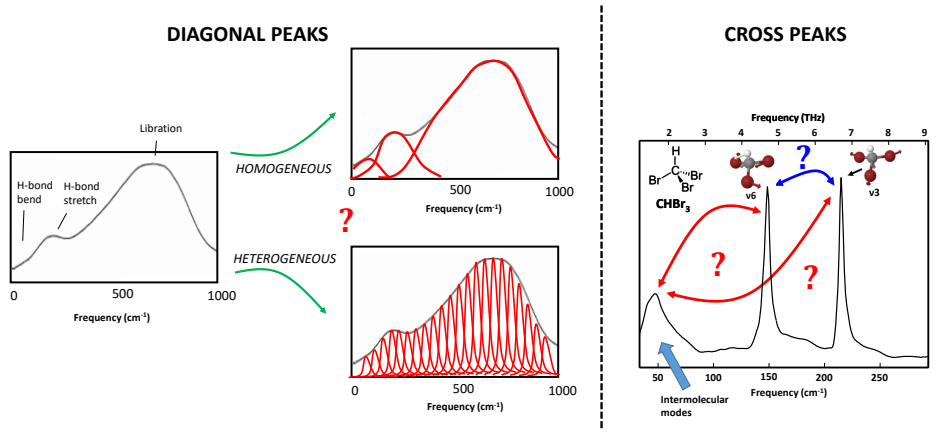

Figure 2.5: The topics on which this dissertation will be focusing on.

on the contrary, a long lived photon echo feature would be expected for large inhomogeneous broadening, whose extent would be directly proportional to the persistence of these extended molecular networks.

Secondly, we will investigate the response of different halogenated liquids (the same type as Blake and co-workers studied[60, 61]), whose sharp intramolecular modes are key to understanding possible coupling patterns that might arise between different molecular vibrations(right-hand side of Fig2.5) and, in turn, reveal the real capabilities of 2D Raman-THz spectroscopy.

Chapter 3

2D Raman-THz spectroscopy

3.1 Concept

As already mentioned in the previous chapter, 2D Raman-THz spectroscopy exploits both near-infrared and THz pulses as excitations to generate the non-linear signal in the investigated sample. In particular, two complementary pulse sequences are used: the Raman-THz-THz (RTT) and the THz-THz-Raman (TRT) sequences (Fig 2.4 bottom)[55, 54].

In a 2D Raman-THz experiment, a nonresonant near infrared pulse and a resonant half-cycle THz pulse interact with the sample. The first laser pulse excites a coherence of an intermolecular (or intramolecular) vibrational mode through either a nonresonant Raman or a resonant THz interaction, depending on which of the pulses hits the sample first. After time t_1, the second pulse (THz or Raman, respectively) interacts with these modes a second time, and the resulting intermolecular coherence is read out at time $t_1 + t_2$ by the emission of a THz field from the sample. The magnitude of the emitted signal is proportional to the THz electric field strength and to the intensity of the Raman pump[54, 55]:

$$SIGNAL \propto E_{THz} \cdot I_{Raman} \tag{3.1}$$

3.2 Experimental Techniques

The main laser beam used for the experiments comes from the output of a commercial Ti:Sapphire amplified system (Spitfire Pro). The s-polarized pulses are emitted at a wavelength of 800 nm, with an energy of ∼0.8 mJ/pulse at 5 kHz repetition rate. The pulse duration is ∼110 fs. Different copies of the main beam are used in the setup to generate/detect the THz pulses and as the Raman pump. The signals that we aim to measure are small, about 10^{-5}-10^{-4} of the exciting THz field, which translates in long measurement times, in the order of days. Therefore, an important requirement, together with optimized detection sensitivity, is that the system must be stable enough in order to be reliable for long averaging times. This stability is inherently achieved by the relative simplicity of the experimental setup, where the only non-linear processes are generation and detection of THz pulses; as such, issues like, for example, beam pointing or sensitivity to pulse compression are not so detrimental as they could be for systems with more delicate and unstable non-linear processes like optical parametric amplification or white light generation. Furthermore, since generation and detection arise from the same laser pulse, timing jitter between the gate and the THz pulses is marginal.

3.2.1 Generation and detection of THz pulses in Gallium Phosphide

The THz excitation pulses are generated and detected through two equivalent 0.1 mm thick gallium phosphide crystals, cut along the ⟨110⟩ plane (GaP-110). Fig 3.1 shows a schematic view of the crystal with highlighted the crystallographic directions. Both processes of generation and detection originate from the nonlinear nature of GaP, which lacks of inversion symmetry and as such, possesses a non-vanishing second order $\chi^{(2)}$ susceptibility. The choice of the crystal thickness depends on th experiment and the desired performance; generally, THz emission strength and detection sensitivity are proportional to the thickness of the crystal. At the same time, the emission

and detection bandwidth are inversely proportional to the thickness: this reciprocal condition requires a trade-off between strength/sensitivity and bandwidth that can be adjusted depending on the circumstances. Thin crystals also limit the accessible temporal window due to etaloning effects. For our experiments, we chose a 0.1 mm thick crystal (i.e. as thin as possible) for both crystal because the aim is to maximize both the excitation and detection bandwidth, at the expense of the strength of the electric field.

It is worth mentioning that, in order to achieve higher THz transients, one could resort to another zincblende type nonlinear crystal: zinc telluride (ZnTe). THz pulses generated via optical rectification in ZnTe are about 10 times stronger than the ones obtained with GaP (∼1 kV/cm and ∼10 kV/cm, respectively) but the available bandwidth of the pulses is limited to ∼2.5 THz by the self-absorption of the optical phonon resonances in the material[62]. In GaP, the available bandwidth is about 7 THz.

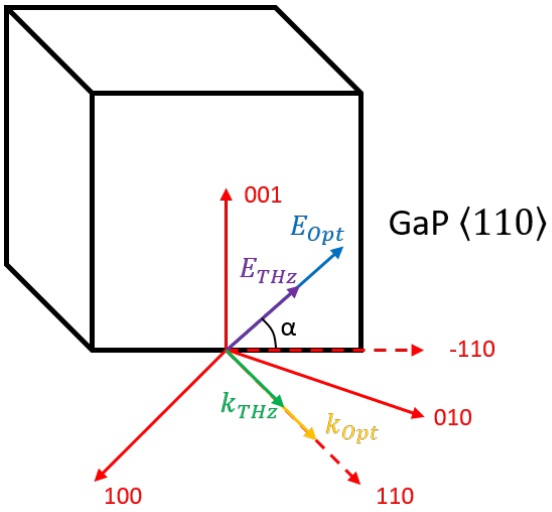

Figure 3.1: GaP crystallographic directions(red), polarization and propagation directions of the THz and optical beams. The angle alpha is the angle between the [-1,1,0] axis and the polarizations of the fields. See text for details.

Generation

For the THz generation, we focus part of the main beam (∼10 μJ) onto the GaP crystal which emits THz via optical rectification[63]. In order to give a brief overview of the process, we can start by writing electric field of the impinging infrared pulse as the product of a carrier wave oscillating at frequency ω times an envelope: $E(t) = E_0(t)\cos(\omega t)$. This intense electric field will induce a second order non-linear polarization inside the crystal that can be expressed as[62]

$$P^{(2)} = \chi^{(2)}E^2 = \chi^{(2)}E_0(t)\frac{1+\cos(2\omega t)}{2}. \tag{3.2}$$

The two terms relate to the second harmonic field, that oscillates at a frequency 2ω, and a 'rectified' DC field. The latter represents the emitted THz field, which - since the pulse has a duration of about 100 fs and consequently a bandwidth $\Delta\omega \approx$10 THz - is the result of difference frequency mixing between the frequencies inside the laser's pulse bandwidth. As a consequence of this mixing, the rectified component roughly reflects the envelope of the generating laser pulse. The difference among these frequencies falls in the THz range[62]. The overall conversion efficiency of this process is extremely low, $\approx 10^{-7}$ of the incident pulse energy[20], which translates in quite weak THz electric fields.

In order to maximize the efficiency of the generation process, it is important to place the crystal with the right orientation with respect to the polarization of the incoming laser field. In Fig 3.1 the yellow arrow indicates the propagation direction of the infrared field and the emitted THz field which are both perpendicular to the $\langle 110 \rangle$ plane. The azimuthal angle alpha between the polarization direction and the [-1,1,0] direction at which the non-linear response of the material is maximized is around 60 degrees[64].

Detection

The method used for the detection is a conventional electro-optic sampling scheme[62] and it is depicted in Fig 3.2. It is based on the Pockels effect in

which an applied field causes the detector crystal to become birefringent. The induced change in the refractive index of the material can be expressed as

$$\Delta n \simeq \frac{1}{2}\chi^{(2)} E_{THz} \tag{3.3}$$

where E_{THz} is the THz electric field co-propagating with the optical beam. When the s-polarized 800 nm sampling pulse (energy of few nJ) travels through the crystal at the same time as one point in the THz pulse, a phase-retarded p-polarization component is generated, resulting in a slightly elliptically polarized beam.

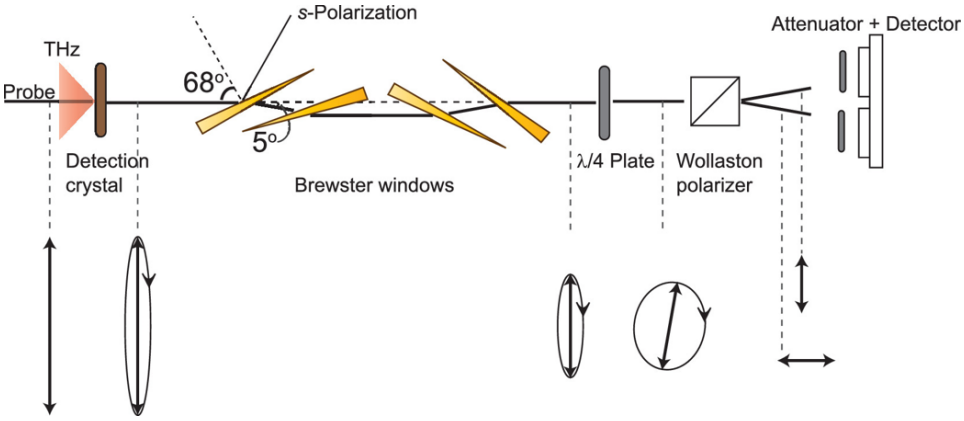

Figure 3.2: Electro-optic sampling scheme used in the 2D Raman-THz setup. Figure adapted from Ref[3].

The magnitude of the induced p-polarization is proportional to the magnitude of the co-propagating THz field, and the direction of rotation is proportional to the sign of the field. The infrared light is then passed through a quarter wave-plate which results in a distorted circularly polarized beam; this polarization modulation is subsequently converted to an intensity modulation by a Wollaston prism, whose function is to spatially divide the beams with perpendicular polarization and send them to a balanced photodetector. Such intensity difference between the two orthogonally polarized components is proportional to the THz electric field:

$$\frac{I_{\leftrightarrow} - I_{\updownarrow}}{I_{\leftrightarrow} + I_{\updownarrow}} \propto \Delta n \propto E_{THz}. \tag{3.4}$$

In this manner, the entire pulse amplitude as a function of time is mapped out by scanning the delay line that determines when the readout pulse arrives at the detector crystal relative to the THz pulse. In order to further reduce the s-polarization component relative to the p-polarization one and thus increase the overall sensitivity of the system, a sequence of zinc-selenide (ZnSe) Brewster windows is placed between the crystal and the quarter-wave plate[3]. As with the generation process, the rotation of the detection crystal with respect to the gating beam and THz pulse polarization (parallel to one another) is crucial to achieve maximum detection efficiency. In this case the best angle alpha(Fig 3.1) for maximum sensitivity is 0 degrees[65].

THz pulses

The THz pulses generated and detected with the above-mentioned methods are shown in Fig 3.3. They are "half-cycle" pulses with a duration of 140 fs(FWHM of the positive spike) and with a spectrum that extends from 0.2 to ∼7 THz peaked at 1.3 THz.

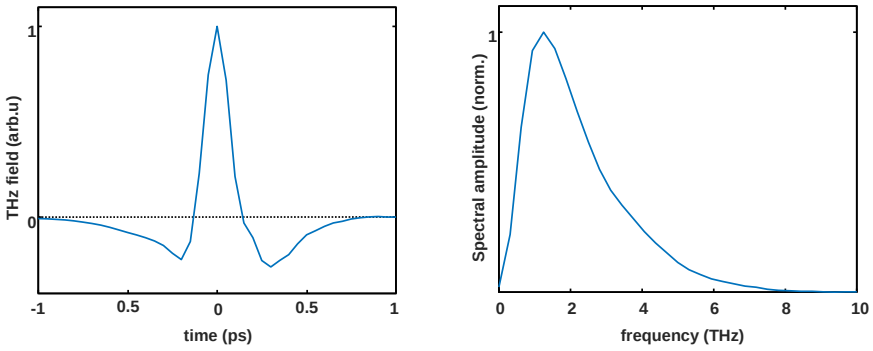

Figure 3.3: THz pulse in time domain (left-hand side) and corresponding spectral amplitude (right-hand side)

3.2.2 2D Raman-THz experimental setup

The setup for the 2D Raman-THz experiment is based on a conventional THz-probe setup[66] and is sketched in Fig 3.4. With the help of beam splitters, the main beam is split into three branches: Raman pump, THz generation and THz detection. As already described in the previous section, the generation and detection beams are focused with a lens (f=750 mm and f=400 mm respectively) to a spot size of $\sim$50 μm onto two equivalent GaP crystal. The generated THz pulses are then focused onto the sample and subsequently collected on the detection crystal via two custom made aluminum elliptical mirrors (f=83 mm), whose position on the optical table is fixed; the mirrors are built such that the geometrical position of the four theoretical foci, two of which coincide in the sample position, is known. Due to the large area of the mirror, the numerical aperture of such a system is close to unity which means that the THz pulses are focused to an almost diffraction limited spot in the focus.

Precise positioning of the optical elements (sample, generation and detection crystals) in the elliptical mirrors foci is made possible through the help of an aluminum alignment tool and a precision measurement tool, the latter of which can measure relative distances with a precision up to $\sim$100 μm. It is important to place the elements in the foci as precise as possible to both maximize the efficiency of the processes and to avoid artifacts that might arise from a wrong Gouy phase[67]. The detection beam is controlled by a fast-scanning delay stage (see next section for details) labeled as t_2 and fed into the detection crystal through a small hole drilled in the elliptical mirrors. The pump beam, with energies ranging from 8 to 150 μJ, is passed through a conventional optical delay stage (t_1), chopped at half the frequency of the laser's repetition rate, focused (f=1 m) onto the sample, and subsequently coupled out of the elliptical mirrors. The actual focal point is placed after the sample, such that the spot size of the optical beam is matched with the spot size of the focused THz pulses (250 μm) at the sample position. All the THz section of the setup is enclosed in a nitrogen purged box, to avoid absorption from water vapor. The sample can be either a 50 μm windowless

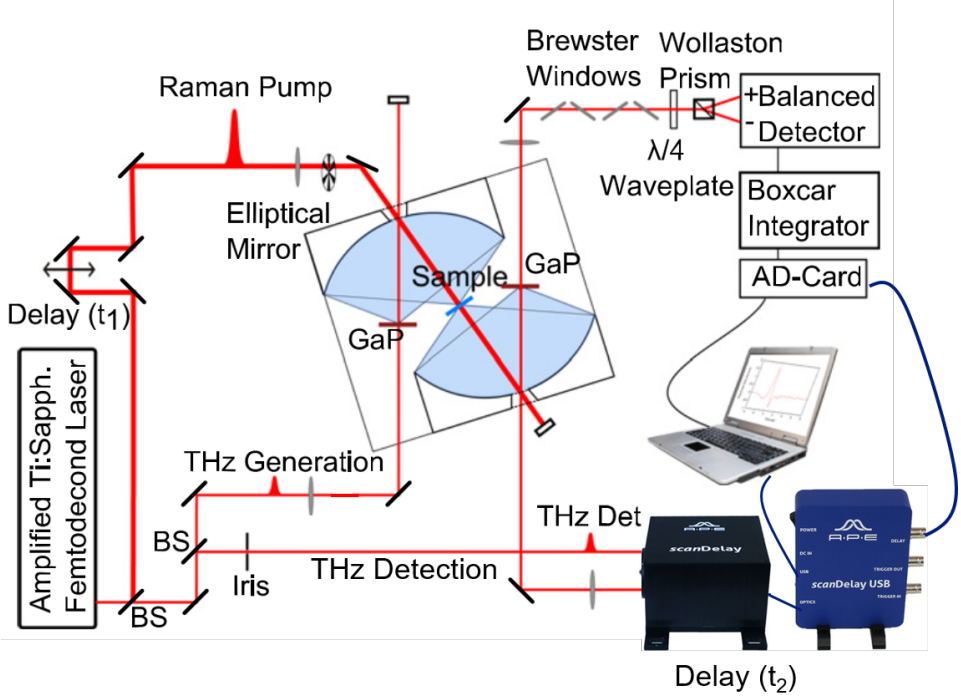

Figure 3.4: Experimental setup for 2D Raman-THz spectroscopy

free falling jet (when the sample is liquid water)[55, 68] or a sealed static cuvette made of two thin (∼100 μm) sapphire windows separated by a teflon spacer (50-500 μm)[69].

3.2.3 Fast Scan delay stage

In a previous version of the setup[55], an additional chopper to modulate the generation beam at a quarter of the laser's repetition rate (two pulses on, two pulses off) and a stepper motor on the detection branch were part of the setup. The total measured signal was composed of four states (two from the pump chopper and two from the generation chopper):

S_{11}=Pump$_{ON}$ THz$_{ON}$

S_{10}=Pump$_{ON}$ THz$_{OFF}$

S_{01}=Pump$_{OFF}$ THz$_{ON}$

S_{00}=Pump$_{OFF}$ THz$_{OFF}$

In our experiment, the signal of interest is defined as the pump-induced time evolution of the change in the THz pulse wavefront transmitted through the sample; therefore, the signal at the detector with double chopping modulation can be written as function of the four states:

$$S_{step} = (S_{11} - S_{10}) - (S_{01} - S_{00}) \tag{3.5}$$

The idea behind chopping the generation beam comes from the need of taking care of the intensity fluctuations of the laser beam during the acquisition time of the entire THz front. In this way, the correlated shot to shot intensity variations and slow drifts (on the order of $\sim$1 second for these laser systems), are removed via subtraction of subsequent pulses. This procedure comes at the price of an increased measurement time, since half of the shots are "wasted" to take care of the laser noise. Measurement times are extremely long, thus faster acquisition methods are crucial for a more practical implementation of this spectroscopy.

Currently and for all the results shown in this dissertation, the delay stage on the detection beam path consists of self-referenced continuously moving retroreflector (FastScan APE), which has replaced both the detection stepper motor and the additional chopper on the generation beam path. Now, the total signal is simply:

$$S_{fast} = S_{11} - S_{01} \tag{3.6}$$

The settings on the motor controller allow to acquire an entire THz front in one second, that is a 1 Hz scanning frequency. In an ideal experiment, one would acquire the entire THz front with few sampling pulses as possible (ideally on a single shot basis[70]), in order to simultaneously handle both shot to shot and slow fluctuations.

In figure Fig 3.5 the noise performances of the FastScan versus the step scan are compared. On the left side, we can see how, qualitatively, the two

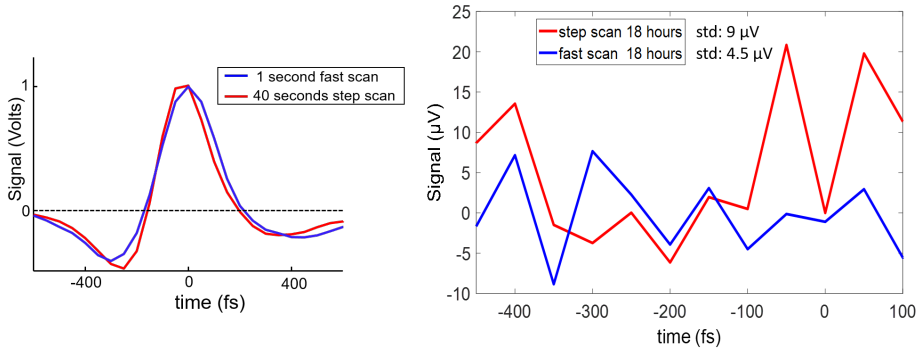

Figure 3.5: Noise comparison of Fast scan vs Step scan.

wavefronts acquired with the two methods look very similar, although they differ by a factor 40 in the acquisition time. For a more quantitative analysis, we compare the noise of a 2D map (right-hand side of Fig3.5) with the same averaging times, but with a difference of a factor 2 in the number of laser shots (because in the fast scanning setup the generation chopper is removed), for the two scanning methods. The comparison of the standard deviation shows an improvement of a factor 2 in the signal to noise ratio (SNR) which translates in a factor 4 in the actual acquisition time. This results indicates that, evidently, we have two components contributing to the improvement of the SNR: a $\sqrt{2}$ factor just from removing the generation chopper and hence doubling of the amount of laser shots used to acquire the signal (the SNR goes as $\sqrt{N}$, where N is the number of laser shots). Another $\sqrt{2}$ factor comes from the fact that with fast scanning, apparently, we get rid of intensity fluctuations of our laser system that happen on a time scale that is slower than 1 second, since the scanning frequency of the motor is 1 Hz.

3.3 Instrument response function and pulse sequences

In general, any signal is convoluted with the instrument response function (IRF) of the system that measures it. The total measured response is given

by the convolution of the not infinitesimally short excitation pulses with the molecular response[29], the latter being the quantity that one ultimately wants to extract.

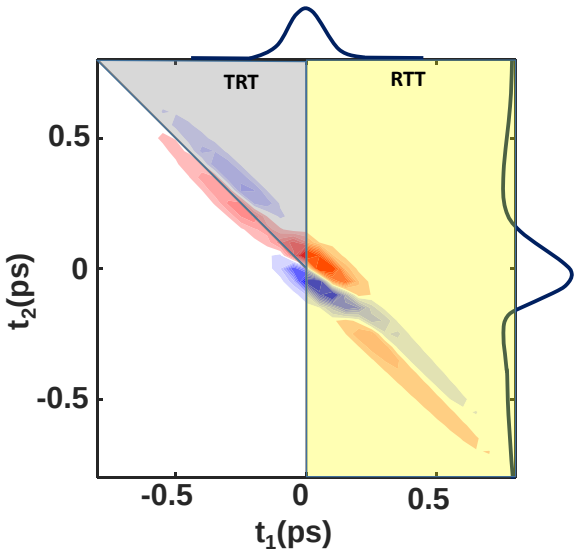

Figure 3.6: The time-domain 2D plot of the IRF with the THz and Raman pulses shown along the right and upper axis; the RTT quadrant is shaded in yellow and the TRT in grey. Black dashed lines highlight where the echo signal would show up for both quadrant.

For our experiment, for a given molecular response $R(t'', t')$, the 3^{rd} order non-linear emitted electric field can be written as[55]:

$$E^{(3)}(t_1, t_2) = \frac{d}{dt_2} \int_0^\infty \int_0^\infty dt' dt'' \, E_{THz}(t_2 - t'') \cdot I_{Raman}(t_2 + t_1 - t'' - t') R(t'', t') \tag{3.7}$$

where E_{THz} is the field of the THz pulse and I_{Raman} is the intensity profile of the Raman pump pulse. This equation assumes that the mixing process is quasi phase-matched, and that absorption and dispersion effects in the propagation of the THz pulse from the sample to the detection are small (for a thorough discussion of these effects, see Ref. [55]). If we now assume an

hypothetical instantaneous (i.e. δ-shaped) molecular response of the form $R(t'', t') = \delta(t'')(t')$, we obtain an expression for the IRF:

$$IRF(t_1, t_2) = \frac{d}{dt_2}[E_{THz}(t_2) \cdot I_{Raman}(t_2 + t_1)], \tag{3.8}$$

where the argument $t_2 + t_1$ accounts for the arrangement of the delay lines in our experimental setup. The 2D time-domain plot of the IRF is shown in Fig. 3.6a. For Eq 3.8, we used the THz pulse in Fig 3.3, and an Gaussian-shaped intensity profile for the Raman pulse I_{Raman} with a fitted FWHM of 110 fs (the pulses are shown along the right and upper axis in Fig. 3.6a, respectively).

The delay lines' arrangement in our 2D Raman-THz experimental setup allows to generate two distinct pulse sequences: the (RTT) and the (TRT) sequence. Delay t_1 is defined as the time between the first (Raman for RTT sequence and THz for TRT sequence) and the second THz for the RTT and Raman for the TRT) excitation pulses, whereas t_2 as the time between the THz excitation pulse and the emitted THz field, so not necessarily between the second pulse and the emitted field. On a 2D map, RTT quadrant defines the region of space where t_1,$t_2 > 0$ whereas TRT where t_1+$t_1 > 0$ with $t_1 < 0$. The two quadrants are highlighted in yellow and gray respectively on Fig 3.6.

3.4 Echo pulse sequences

In chapter 2, we described the case of a photon echo signal, whose presence is the signature of an inhomogenously broadened system and it describes the timescale at which an heterogenous system evolves into an homogenous one. The concept of an "echo" in spectroscopy has been established in many different frequency regimes, and the first example traces back to NMR[71], with spin echoes arising from the refocusing of the magnetisation of a two-level spin system. Later on, the concept was extended to infrared and optical frequencies where the echo stems from the inhomogeneous nature of vibrational[72] or electronic absorption resonances[73]. Regardless of the

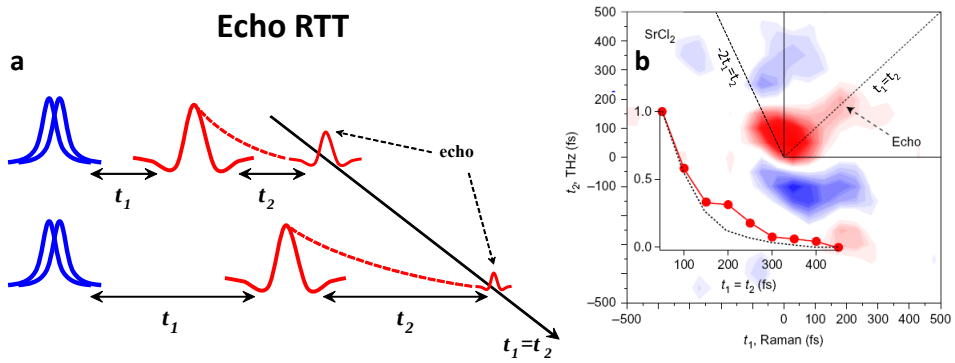

Figure 3.7: In panel (a) the echo pulse sequence for the RTT quadrant and in panel (b) an example of an echo measured with 2D Raman-THz spectroscopy (in the specific case, the sample was a 3M aqueous solution of $SrCl_2$) on the right-hand side. Figure adapted from Ref[4].

specific frequency regime, the mechanism that leads to the build-up of an echo is basically the same: two laser pulses (or three depending on the specific technique) impinge on a sample, the first generates a *coherence* that oscillates and then dephases as time proceeds; the second pulse then might revert this coherence giving rise to an echo, provided that the investigated transition is inhomogeneously broadened. Given the reciprocity of time and frequency domain, the observation of an echo in a 2D response is the time-domain equivalent of an elongated diagonal peak in a 2D spectrum and therefore has the same ability to distinguish between inhomogeneous and homogenous dephasing. Obviously, the time and frequency representation withhold the exact same amount of information and thus the choice reduces to which of the two representations is more intuitive.

With 2D Raman-THz spectroscopy, and in general with all the low frequency multidimensional spectroscopy methods, we are after THz photon echoes, which arise from the inhomogeneity of the intermolecular degrees of freedom of the system. The decay of an echo directly correlates with the lifetime of the intermolecular modes, or, in other words, the lifetime of local structures on a length scale that equals the delocalization length of the intermolecular modes. In particular, we are interested in echoes in liquids

which, given the ultrafast dynamics of the intermolecular forces, are expected to be on ultrafast timescales.

In a typical 2D Raman-THz response, as the one shown in Fig 3.7b, a THz photon echo would show up in the RTT quadrant along the diagonal line where $t_1 = t_2$, whereas for the TRT quadrant along the $-2t_1 = t_2$. Despite the complicated and extended shape of the IRF in the time domain, we can identify the upper right quadrant(where the $t_1 = t_2$ diagonal lies) in the RTT sequence as less affected by the convolution of the pulses and thus well suited for the detection of a possible echo signature(Fig 3.7b). Conversely, the TRT quadrant is more susceptible to the pulses' overlap region, making harder to identify a possible echo signature.

Chapter 4

2D Raman-THz spectroscopy of water isotopologues

This work has been published in Proceedings of the National Academy of Sciences, see Ref[68].

Contribution to the paper

Gustavo Ciardi and Arian Berger performed the measurements and analyzed the data together with Dr. Andrey Shalit.

4.1 Introduction

The measurable variations in the different dynamical and thermodynamic properties of light (H_2O) and heavy (D_2O) water, which have been noted almost a century ago [74], are considered to be a clear manifestation of the quantum-mechanical nature of water [75]. Due to the small mass of the proton, nuclear quantum effects (NQE) such as delocalization, zero point energy, and tunneling, modify the hydrogen bond strength/length and consequently the structure and dynamics of the hydrogen-bond networks, which in turn are considered to be the source of the anomalous behavior of water [76, 77]. The most prominent isotope effects include the elevation in the melting point

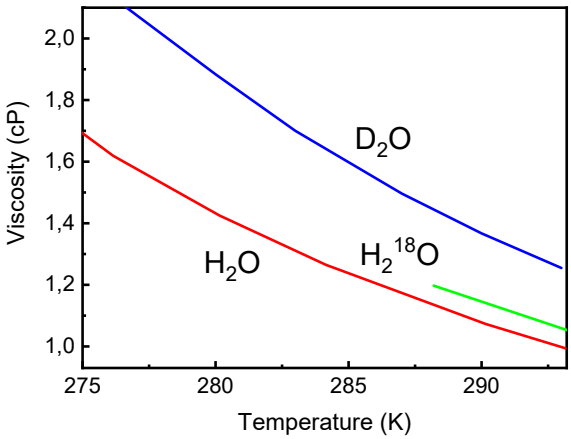

Figure 4.1: Viscosity of H_2O (red), D_2O (blue) and $H_2^{18}O$ (green) in the temperature range relevant to this study. Data are compiled from Refs.[5, 6, 7]

and temperature of maximum density by 3.8 K and 7.2 K, respectively [78], and the increase in viscosity of about 23 % at room temperature upon deuteration of water [74, 79, 80, 5]. The higher structural stability and slowdown in dynamics in D_2O are commonly explained by the stronger hydrogen bonds due to the reduced delocalization of the more classically behaving deuterium. For example, X-ray and neutron scattering confirmed that the oxygen-oxygen and oxygen-hydrogen radial distribution functions of D_2O are more structured than those of H_2O [81, 82]. However, more elaborate models of competing quantum effect were put forward recently [83]. That is, the anharmonicity of the OH-stretch potential renders the quantum-mechanical expectation value of the bond length longer in H_2O, thereby increasing the Coulombic interactions of the proton to a hydrogen-bonded water. This effect causes the lattice constant of H_2O ice Ih to be smaller than that of D_2O ice Ih [84, 85], and the question whether hydrogen bonding is stronger or weaker in H_2O does depend on the structure of the hydrogen bond networks [86]. Also the inversion of the liquid-vapor isotope fractionation ratio at a certain temperature has been attributed to that effect [87].

The temperature-dependent viscosity is a particularly revealing observable

to discuss isotope effects (Fig. 4.1). Robinson and coworkers [79] and later Harris and coworkers [80, 5] demonstrated that the temperature dependent viscosity η of D_2O (Fig. 4.1, blue) can be mapped onto that of H_2O (Fig. 4.1, red) by the following semi-empirical expression:

$$\eta_{D_2O}(T) = \sqrt{\frac{m_{D_2O}}{m_{H_2O}}} \cdot \eta_{H_2O}(T - \Delta T), \tag{4.1}$$

where m is the mass of the two isotopologues. This mapping works remarkably well with an accuracy of 1% in a wide temperature range from T=243-323 K when assuming an effective temperature shift of ΔT=6.5 K. The physical reasoning for this expression is the following: if classical mechanics would apply, it can be shown on very general grounds that any thermodynamic property (e.g., melting point, density maximum, or the distribution of hydrogen bond networks as a function of temperature, etc.) would be the same for all isotopologues. This is since kinetic energy and potential energy partition functions separate, the latter of which being independent of nuclear mass [88]. Dynamical properties (hydrogen-bond vibrational frequencies, self-diffusion or viscosity, etc.), on the other hand, scale with the square-root of mass (i.e., the first term in Eq. 4.1) both in classical and in quantum mechanics. Consequently, the second term in Eq. 4.1 accounts for NQEs. To that end, it is commonly assumed that H_2O at a given temperature is structurally very similar to D_2O at a somewhat elevated temperature, the idea being that enhanced thermal fluctuations in the latter case mimic zero-point fluctuations in the former case [89, 90, 91, 83, 92]. We stress though that the exact number of the temperature shift ΔT varies depending on observable (e.g., 3.8 K for the melting point vs 7.2 K for the density maximum), reflecting the fact that a temperature shift is of course only an effective (empirical) way to account for NQEs.

In this regard, the temperature dependent viscosity of $H_2^{18}O$, whose mass is the same as that of D_2O, is very instructive. It is only $\sim$5% larger than

that of H_2O (Fig. 4.1, green) [7] and can be described as:

$$\eta_{H_2^{18}O}(T) = \sqrt{\frac{m_{H_2^{18}O}}{m_{H_2O}}} \cdot \eta_{H_2O}(T), \tag{4.2}$$

i.e., with the mass factor but without any temperature shift. $H_2^{18}O$ exhibits the same NQEs as H_2O, since the major source of NQEs is the light proton in both cases. For example, the melting point and the density maximum of $H_2^{18}O$ differ by only 0.2-0.3 K from those of H_2O [78]. Nevertheless, the mass factor does appear in Eq. 4.2 and accounts for the dynamical aspect of viscosity.

Conversely, Nilsson and coworkers have presented X-ray scattering results deep into the supercooled regime [93], and concluded that the D_2O data can be mapped onto the H_2O by applying the analogue of Eq. 4.1 with a temperature shift of ΔT=5 K, but without any mass factor. In light of the discussion above, that is expected, since scattering experiments measure essentially instantaneous snapshots of molecular structure, i.e., a purely thermodynamic aspect.

The hydrogen-bonding capability of water supports locally distinct structures that might live for a certain, relevant time span. If one were to instantaneously freeze all motion of liquid water, similar to amorphous ice, one would obtain structurally very heterogeneous snapshots, which would result in inhomogeneously broadened bands in all types of vibrational spectroscopies that are sensitive to molecular structure (e.g., dielectric relaxation and THz [94], IR [95, 96, 97, 98], or Raman spectroscopy [99]). However, liquid water is of course very dynamic and those structures interconvert on very fast timescales, which has a tendency to render the spectroscopic response homogeneous. Being able to discriminate homogeneous from inhomogeneous broadening therefore will tell a lot about the amount of structuring in water and the lifetime of those structures.

However, conventional (1D) spectroscopic techniques cannot make the distinction between homogeneous and inhomogeneous broadening [100]; that is the realm of photon echo and/or 2D spectroscopy [29]. 2D IR spectroscopy

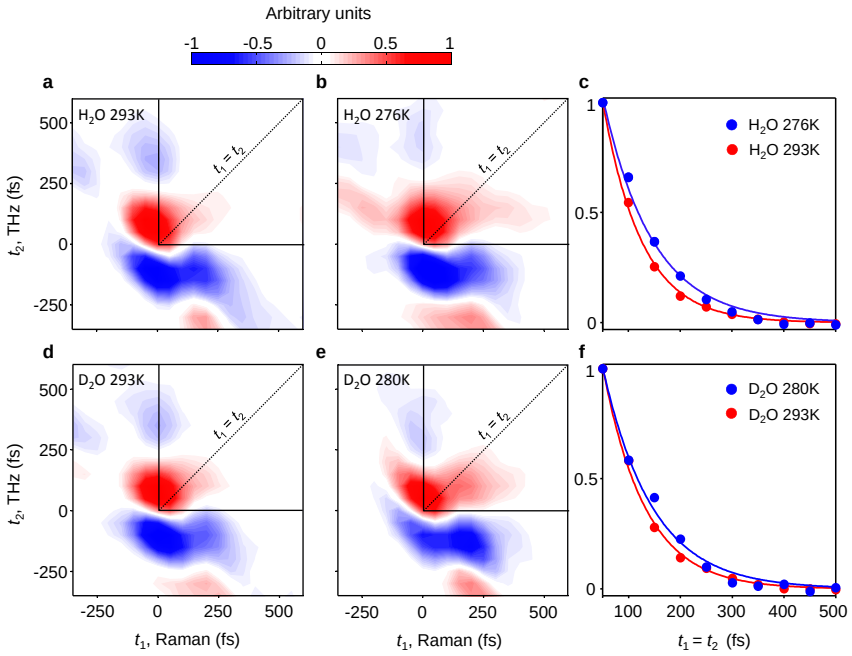

Figure 4.2: 2D Raman–THz–THz responses of neat H_2O and D_2O at different temperatures. Full 2D signals for H_2O at (a) 293 K and at (b) 276 K, as well as for D_2O at (d) 293 K and at (e) 280 K. The upper-right quadrants, which correspond to the Raman–THz–THz pulse sequence, and the main diagonals $t_1 = t_2$ (dashed line) are indicated. Panel (c) compares 1D cuts along the $t_1 = t_2$ diagonal for H_2O at 293 K (dashed red line) and at 276 K (solid blue line), and panel (f) compares those for D_2O at 293 K (dashed red line) and at 280 K (solid blue line), in either case together with single-exponential fits (dashed lines). The 1D and 2D data are normalized to the maximum signal, and the 1D cuts start at 50 fs, after which time the effects of the pump-probe-pulse overlap can be neglected.

has been applied widely to study the time-dependent inhomogeneity of the OH (or OD) stretch vibration of liquid water [101, 102, 103, 104, 105], revealing a typical lifetime of hydrogen bonds in the order of 1 ps. Furthermore, 2D THz-IR-VIS spectroscopy has been demonstrated recently that focuses on the coupling between inter- and intra-molecular modes [106]. However, the intramolecular OH stretch vibration is a high-frequency mode with $\hbar\omega \gg$

k_BT, which is completely frozen at room temperature. A 2D spectroscopy fully in the THz regime would therefore be desired, where the intermolecular modes are found that are thermally excited and hence render liquid water a liquid.

Both 2D-Raman [36, 48, 50, 107] as well as 2D-THz [40, 39] spectroscopy have been developed, but as of today, these experiments have not been feasible for liquid water. We [54], as well as Blake and coworkers [60, 61], have therefore proposed 2D Raman-THz hybrid spectroscopies, which did result in the first 2D response of liquid water in the THz spectral range [55]. We concentrate on the Raman-THz-THz pulse sequence with THz pulses peaking at $\approx$50 cm^{-1}, i.e., in the region of the hydrogen-bond bend vibration of liquid water, and spectrally extending into the hydrogen-bond stretch band at $\approx$200 cm^{-1}. In such an experiment, the Raman pump excites an intermolecular vibrational coherence, which after time t_1 is switched to another coherence state by a THz pump pulse. This coherence evolves as a function of time t_2 and emits a THz field that is detected. Among the many possible coherence pathways, there is a rephasing pathway that switches the sign of the coherence, which requires that the first Raman interaction induces a single-quantum transition, while the second THz interaction induces a two-quantum transition [42, 108]. If the mode under consideration is inhomogeneously broadened on the time-scale of the pulse sequence, that coherence pathway will result in an echo, which peaks at a time t_2 that equals the time-separation t_1 between the two excitation pulses.

In pure water, we found that the signal is indeed slightly extended in the echo-direction $t_1 = t_2$ [55]. Modelling the data base on a very simple model (a single anharmonic oscillator), we suggested that the echo originates mainly from the hydrogen-bond bend vibration at $\approx$200 cm^{-1}, and that a large fraction of its linewidth is attributed to quasi-inhomogeneous broadening in the slow-modulation limit with a correlation time of 370 fs [108]. However, the echo is masked to a significant extent by the instrument response function, hence we set out in a subsequent publication [4] to artificially increase the amount of inhomogeneity by adding salts to the solution. This addition indeed extended the echo, and we found a strong correlation of the echo-

decay time with the viscosity increase induced by a particular cation. For $MgCl_2$, which is characterized as a strong "structure maker", the echo decay starts to exceed the free induction decay time along the t_1 axis, thereby establishing the concept of an echo in these experiments.

In the present paper, we explore how NQEs affect the lifetimes of structural inhomogeneities by directly comparing the extent of the echo signal of the 2D Raman-THz responses for H_2O and D_2O. We follow the temperature dependence and isotope shift of the echo lifetime from room temperature down to their freezing points. We furthermore consider $H_2^{18}O$ in order to disentangle NQEs from trivial (classical) mass effects, in analogy to viscosity (Fig. 4.1). Along with a gradual increase in sample inhomogeneity with decreasing temperature for a given isotopologue, the observed isotope effects on the echo lifetime is attributed to NQEs.

4.2 Results

First, we measured the 2D Raman-THz signal of H_2O in a temperature range of 293 K-276 K. Fig. 4.2a,b serves to demonstrate the qualitative differences in the 2D response at the extreme temperatures considered in this study. As has been discussed previously [55, 109, 108], the measured signals in 2D Raman-THz spectroscopy are governed by the quite evolved instrument response function (IRF), which significantly smears out the real molecular signatures. We will focus our analysis on those parts of the 2D response that are less susceptible to such contaminations from the IRF , i.e., the diagonal t_1=t_2 in upper right quadrant (dotted lines in Fig. 2), along which an echo is expected in the Raman-THz-THz pulse sequence. Figs. 2a,b show that the relaxation dynamics along this diagonal becomes slower with decreasing temperatures. Fig. 4.2c presents 1D cuts along the diagonal together with single exponential fits (dashed lines), for which this trend is more clearly visible. Fig. 4.3 confirms that observation on a more quantitative level by plotting the relaxation times of H_2O (red) derived from the single exponential fits to the 1D cuts along t_1=t_2 against temperature. Overall, the decay can be modelled extremely well assuming a single-exponential function, and it

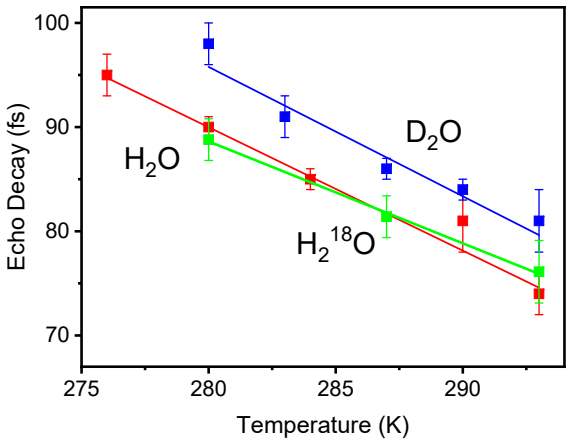

Figure 4.3: Echo decay times of H_2O (red), D_2O (blue) and $H_2^{18}O$ (green) as a function of temperature. While H_2O and D_2O have been measured under absolutely comparable conditions and post-processed identically, $H_2^{18}O$ has been measured differently. For a direct comparison with the H_2O and D_2O data, the $H_2^{18}O$ data were up-scaled by 5%, as discussed in Materials and Methods. The lines are linear fits to guide the eyes.

slows down by almost 20% from 74±2 fs at room temperature to 95±2 fs at 276 K.

Next, we obtained the 2D Raman-THz responses for D_2O in the temperature range of 293-280 K. Figs. 2d,e show the full 2D signals observed at room temperature and close to the freezing point of D_2O, respectively, and Figs. 2f 1D cuts along the diagonal t_1=t_2. As in the case of H_2O, the signal along the diagonal is clearly extending with decreasing temperature. Fig. 4.3 reveals that the decay times for D_2O (blue) are consistently slower than for H_2O (red), ranging from 81±3 fs at room temperature to 98±2 fs at 280 K.

Analyzing the H_2O and D_2O results in the context of Eq. 4.1, we find that either one of the two correction factors could explain the difference in the echo decay time, but it turns out that both at the same time would overestimate the effect. That is, the difference in the echo decay time is $6.5 \pm 1\%$; within signal-to-noise the same as the factor $\sqrt{m_{D_2O}/m_{H_2O}} = 1.054$. In that scenario, the difference in the echo decay time would reflect a (trivial) dynamical effect.

Conversely, given the identical slope of the two plots, one may also shift the D_2O data onto the H_2O data by introducing an effective temperature shift of $\Delta T = 4.5 \pm 1$ K. Such a temperature shift is well within the range of what would be considered a reasonable value for a NQE; e.g., it is about the same as the shift of the melting point (3.8 K). If that is the explanation for the difference, one would conclude that the echo lifetime measures the different degree of hydrogen bond structuring of H_2O vs D_2O.

From the results of H_2O and D_2O alone, we cannot decide which one of the two explanations is correct. We therefore now turn to $H_2^{18}O$, whose mass is the same as that of D_2O, which however equals H_2O in terms of NQEs. Fig. 4.4 compares the echo decay along the diagonal $t_1 = t_2$ for $H_2^{18}O$ (green) with those of H_2O (red) and D_2O (blue) at 293 K, all of which are measured under directly comparable conditions, and Fig. 4.3 (green) plots the echo decay time of $H_2^{18}O$ as a function of temperature. In either case, the result for $H_2^{18}O$ and H_2O are indistinguishable within error, while the echo decay of D_2O is clearly slower. This in turn evidences that the difference of H_2O vs D_2O is due to NQEs, and not due to a dynamical mass factor:

$$\tau_{D_2O}(T) = \tau_{H_2O}(T - \Delta T). \tag{4.3}$$

We therefore propose that the echo decay time indeed reflects NQEs.

4.3 Discussion and Conclusion

In light of the discussion of Eq. 4.1, it might seem puzzling that the square-root-mass factor is not observed in the echo decay time; after all, that is a dynamical aspect. We think of dephasing in a liquid like water in terms of "spectral diffusion", i.e. an ensemble of modes, whose frequencies fluctuate as a function of time with a characteristic correlation time τ_c [29]:

$$\langle \delta\omega(t)\delta\omega(0)\rangle = \Delta\omega^2 e^{-t/\tau_c} \tag{4.4}$$

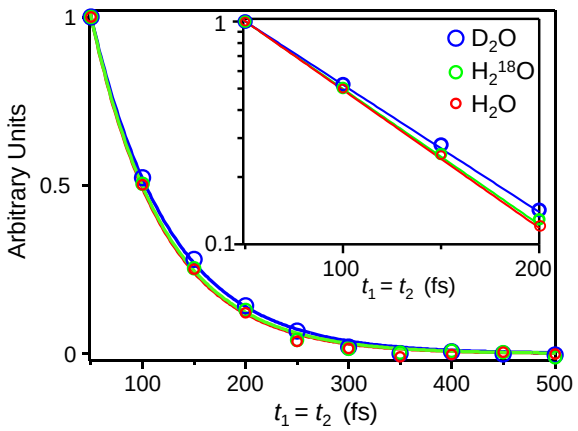

Figure 4.4: 1D scan of the echo decay signal measured along the diagonal $t_1 = t_2$ for H_2O (red), D_2O (blue) and $H_2^{18}O$ (green) at 293 K, in either case together with single-exponential fits (dashed lines). The insert shows the same data on a log-scale. While these data have been measured slightly differently than those in Fig. 4.2 (see Materials and Methods for details), they are directly comparable among each other. The data are normalized to the maximum signal, and the cuts start at 50 fs, after which time the effects of the pump-probe-pulse overlap can be neglected.

where $\delta\omega(t) = \omega(t) - \langle\omega(t)\rangle$ is the deviation from the mean of the transition frequency, and $\Delta\omega$ is the standard deviation of the frequency distribution. On the timescale τ_c, an instantaneously inhomogeneous ensemble converts into a homogeneous one. In the limes $\Delta\omega\tau_c \ll 1$, one would obtain purely homogenous dephasing with $T_2^* = (\Delta\omega^2\tau_c)^{-1}$, and in the limes $\Delta\omega\tau_c \gg 1$ statically inhomogenous broadening with an absorption band, whose width is $\Delta\omega$. In the inhomogenous limes, $\Delta\omega$ is the dominating factor determining the echo decay time, while the effect of τ_c is minor (which can be seen when calculating a rephasing coherence pathway in second order perturbation theory starting from Eq. 4.4, see Ref. [110]). While τ_c is a dynamical property, for which one would indeed expect to observe a square-root-mass factor, the distribution of frequencies is a purely thermodynamic property, which is mass-independent. Since we do not observe a difference in the echo decay time between H_2O vs $H_2^{18}O$, we conclude that we are in the inhomogenous

limes, and indeed, a fit of the experimental data of H_2O at room temperature has revealed $\Delta\omega\tau_c \approx 5$ (i.e., τ_c=370 fs, $\Delta\omega$=75 cm^{-1}) [108].

Other aspects might however contribute as well to that issue. For example, any hydrogen-bond rearrangement requires the rotation of a water molecule [111, 98], which is governed by its moment of inertia and not its translational mass. The moment of inertia of $H_2^{18}O$, averaged over the three principal axes, is only 0.5% larger than that of H_2O, thereby providing another possible explanation for the mass-independence of the echo decay time. The D_2O results however speak against that scenario, since its moment of inertia is almost twice that of H_2O, yet the effect on the echo decay time is only 5%. Hence, hydrogen-bond switching events don't seem to be rate-determining for the echo-decay time. And indeed, the rotational diffusion times of H_2O and D_2O have been calculated using ring polymer molecular dynamics (RPMD) simulations, revealing a significantly larger difference of $\sim$30% at 298 K [98]. About 1/3 of that effect has been attributed to the classical mass effect and the remainder to NQEs.

The discussion in the previous two paragraph emphasizes that our strict separation of Eq. 4.1 into a dynamical mass factor and NQEs is probably a bit of an oversimplification. In particular, both the effective mass (e.g., translational mass vs moment of inertia) and the effective temperature shift needed to mimic NQEs depend on the degrees of freedom that are relevant for a given process. At the same time, the two correction factors cause similar shifts and are experimentally very difficult to disentangle, in particular when the considered temperature range is small. It appears that viscosity shown in Fig. 4.1 is a particularly straight-forward to interpret observable in this regard. We nevertheless think that our discussion of Eq. 4.1 is a valid starting point to set the stage, and that the comparison of H_2O vs D_2O vs $H_2^{18}O$ does contain the information needed to disentangle NQE from trivial (classical) mass effects.

A reasonable agreement of response calculations based on classical MD simulations with experimental 2D Raman-THz signals has been obtained when a proper force field is used [109]. Combining these simulations with RPMD, thereby including NQEs, will be computationally very expensive,

but is not out of reach. That is, while RPMD simulations of water have been connected to various spectroscopic observables, such as IR [96, 97, 98] or X-ray absorption spectroscopy [112], they required the calculation of only a two-timepoint correlation function, as they simulated one-dimensional responses. Converging a three-timepoint correlation function required for 2D-Raman-THz spectroscopy will be computationally much more expensive, but efficient concepts to perform this task have already be proposed [113]. In any case, such simulations will be needed to test to what extent the very idea of Eq. 4.1 describes the 2D-Raman-THz echo of liquid water properly.

Methods A 50 μm thick wire-guided gravity-driven water jet was used for the measurements to avoid any signal contribution from a window material. The temperature of the water jet was controlled by an external water-ethanol bath, which cooled the water reservoir just above the jet. The temperature was measured in close proximity to the intersection region of Raman and THz pulses in the jet with an accuracy of $\pm$0.5 K.

Due to the small signal size, a substantial acquisition time is needed, typically on the order of 24 h per full 2D data set. The stability of the laser system and the water jet is a concern on that timescale. An active beam stabilization scheme was used to correct for beam walking of the laser system. To reduce drifts in the water jet thickness (e.g., due to evaporation of water), an active jet stabilization has been implemented, where the thickness of the jet was measured based on the time-delay of the transmitted THz pulse and was corrected by adjusting the water flow. Moreover, during the post-processing, the data, which consists of typically 300-500 individual 2D Raman-THz scans, were corrected for temporal drifts by adjusting the signal maxima in sequential data subsets with a typical size of 100 scans.

The diagonal signal shown in Fig. 4.2c,f were constructed by averaging over the main diagonal $t_1 = t_2$ and the first upper and lower off-diagonals, and their decay times were determined from single exponential fits. The major source of error in the decay time is the offset level for large times $t_1 = t_2$, which has been subtracted. To determine its uncertainty, the standard deviation of the background signal in the response-free quadrant ($t_1 < 0$ and $t_2 < 0$) has been estimated, from which the error in the decay time has been calculated. Great care was taken to measure H_2O and D_2O subsequently and under exactly the same conditions, and to post-process the data the same way, in order to be able to compare decay times with an accuracy of $\approx$1-2 fs.

To reduce the measurement time for the quite expensive $H_2^{18}O$, only the diagonal $t_1 = t_2$ has been measured, which results in a larger uncertainty of the time zeros $t_1 = t_2 = 0$, since one misses the peak of the 2D signal. Therefore, H_2O and D_2O have been measured as well along with $H_2^{18}O$ under exactly the same conditions. Fitting these H_2O and D_2O data revealed 5% faster time constants compared to those in Fig. 4.2. Consequently, the $H_2^{18}O$ data shown in Fig. 4.3 (green line) are up-scaled by that factor to facilitate a direct comparison.

Chapter 5

2D Raman-THz spectroscopy of slightly supercooled water

Contribution to this chapter

Gustavo Ciardi performed the experiments and analyzed the data together with Arian Berger and Dr. Andrey Shalit.

5.1 Introduction

The intricate structure of hydrogen-bond networks makes water a highly complex liquid and it is generally accepted that these intermolecular networks are responsible for many water's anomalous properties, as for example the density maximum at 4 °C. The structure, lifetime and spatial extent of such extended networks might change depending on the temperature, especially below the freezing point. At room temperature the magnitude of the anomalies is relatively small but upon cooling, the significance of such unusual properties increases sharply. For this reason, the metastable supercooled regime (i.e. liquid water below the freezing point) is particularly interesting[114, 115] yet not easily accessible with experiments due to its extremely precarious equilibrium.

Water normally becomes a solid at 273.15 K (0 °C), but it can be

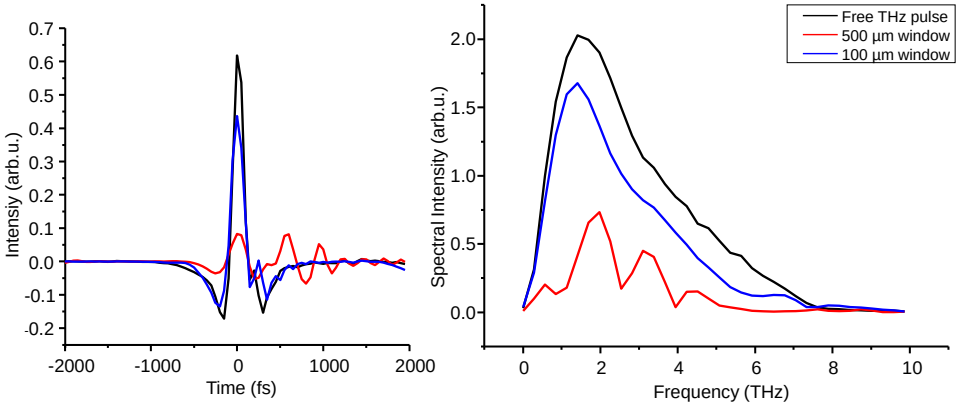

Figure 5.1: THz transmission of sapphire windows, temporal shape (left-hand side) and corresponding spectrum (right-hand side).

supercooled at standard pressure down to its crystal homogeneous nucleation temperature at almost 232 K (∼-41 °C). The process of supercooling requires water to be extremely pure and free of potential heterogeneous nucleation sites but the cooling itself does not require any special technique. This means that a small quantity of water is easier to supercool, since the amount of nucleation sites is drastically reduced.

In order to perform a 2D Raman-THz experiment of supercooled water, the windowless liquid jet approach used in references[55, 4, 68] is not feasible due to the rather limited ability to affect the temperature of jet: the only other accessible way is to employ a sealed cell filled with a small volume of water and a cooling channel built around it.

5.2 Window material and sample cell

The requirements that make a window material suitable for a 2D Raman-THz experiment are demanding to meet. At first, trivially, it must show good transmission in both THz and near infrared frequency range since the resulting signal is proportional both to the THz electric field magnitude and the intensity of the Raman pump. Secondly, and most crucially, due to the

high near infrared energy regimes of the experiment (10-100 μJ), windows must not become THz absorber when undergoing such high irradiance: the gap between valence and conduction band of the chosen window material must be large enough to avoid the promotion of carriers in the conduction band via multiphoton absorption, where, being now free carriers, would absorb THz radiation.

Thin sapphire plates turn out to have good performances for both requirements. Fig 5.1 presents static THz transmission measurement through sapphire windows of different thicknesses. For thin enough window (100 μm), the shape of the pulse is preserved, with a sufficiently good transmission of about 75% of the input THz field. On the right-hand side of Fig 5.1, the corresponding magnitude of the Fourier transform of the data on the left-hand side is plotted. Importantly, we see that, for the thin window, the spectral intensity of the free THz pulse spectrum is decreased but the shape is preserved, hinting to the fact that windows, when thin enough, induce only reflection (and thus not absorption) losses. Increasing the thickness to 500 μm leads to a drastic reduction of the transmitted light and to significant distortion of the temporal and spectral shape of the transmitted pulse, probably due to strong etaloning inside the sapphire. The resulting cell is ultimately composed of two 100 μm windows separated by a spacer and filled with the water sample. Therefore, the total THz transmission of the empty cell is about 50% and transmission of 800nm light is around 70%.

The next step is to characterize the THz absorption of the cell when pumped with near infrared light. Fig 5.2 shows THz transmission through the empty cell for three different pump energies. Dealy t_1 indicates the delay between the 800nm pump and the maximum of the THz electric field (i.e. $t_2 = 0$). For negative t_1 delay times the THz pulse comes before the near infrared one and thus no transient absorption signal is observed. As we cross $t_1 = 0$ (i.e. pulses' overlap) and for positive t_1 times, we observe a transient THz absorption that kicks in as we increase the energy of the near infrared pump. As we will see in the next sections, the size of the signal from water is about one order of magnitude less than the transient THz absorption of the sapphire window. For this reason we need to perform the experiments in

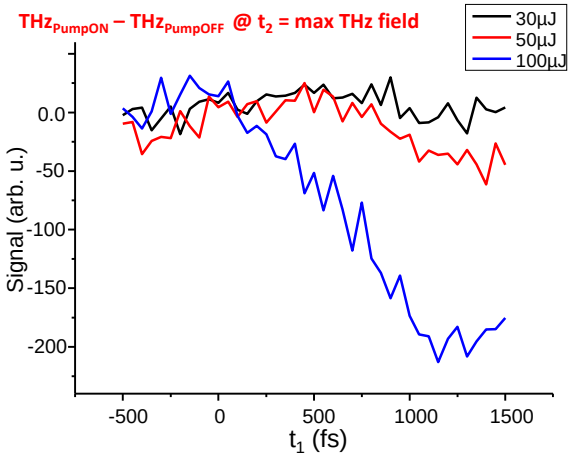

Figure 5.2: THz absorption of the window as function of the Raman pump energy. For energies higher than 30 μJ sapphire starts to become more opaque to THz light.

a regime where is certain that no THz is absorbed by the windows. The plot of Fig 5.2 indicates that the safe threshold is below 30 μJ. The reduction of the Raman pump energy for the cell with respect to the windowless water jet system of about one order of magnitude (from $\sim$30 μJ to $\sim$200 μJ) brings along a reduction of the signal of roughly the same amount.

The final design of the sample cell and cooling system is depicted in Fig 5.3: two sapphire windows intermediated by a 50 μm teflon spacer and filled with 3-4 μL of double-distilled water. The body of the cell is made of an heat conductive brass frame with an embedded cooling channel and the coolant is a mixture of water and ethanol, whose flow and temperature are controlled by an external chiller. The cell with the water sample is assembled in a nitrogen-purged glovebox to reduce dust deposition and consequent freezing due to heterogeneous nucleation. With this precaution, the lowest achievable temperature is around 263 K (measured at the sample position through a thermocouple with an accuracy of $\pm$1 K) before freezing occurs.

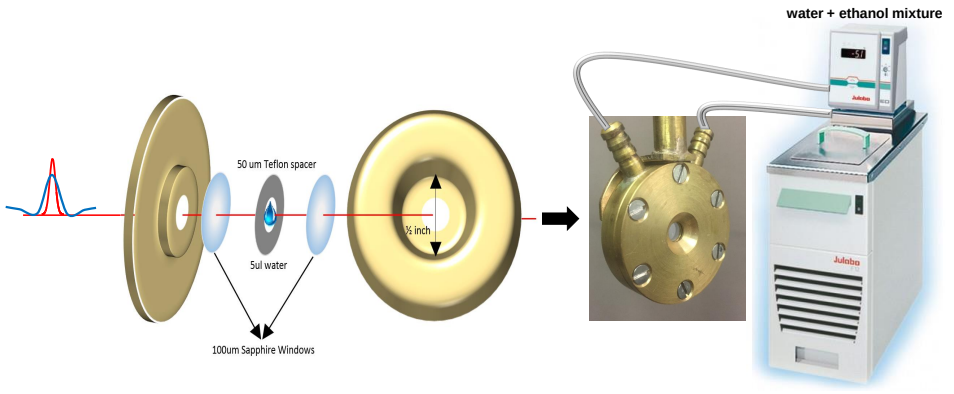

Figure 5.3: Design of the sample cell and cooling channel.

5.2.1 THz transmission as function of temperature

As the temperature in the cell is varied, the amount of THz light transmitted through the water sample changes accordingly. In particular, as shown in figure Fig 5.4, the wavefront slightly shifts to the left and intensity increases as sample is cooled. The inset shows the peak intensity of the THz pulse as function of temperature together with a linear fit (red line) that reveals a slope $\Delta T/T = -7.5 \cdot 10^{-3}$ K^{-1}. This data and the slope of the fit have been used to estimate the temperature change in water for the solvation experiment of Ref[116].

5.2.2 Window response

With the introduction of sapphire windows in the focus of our system, it is important to fully characterize the material and understand how its 2D Raman-THz response, if present, might affect the actual signal from water. To this end, the first step is to measure the 2D Raman-THz response of a single sapphire window. Fig 5.5 shows the 2D Raman-THz response of an 100 μm sapphire plate. On the left-hand side we have the full 2D time response and the signal is mostly concentrated in the pulses overlap region. In order to analyze the response in detail, we take a one dimensional cut of

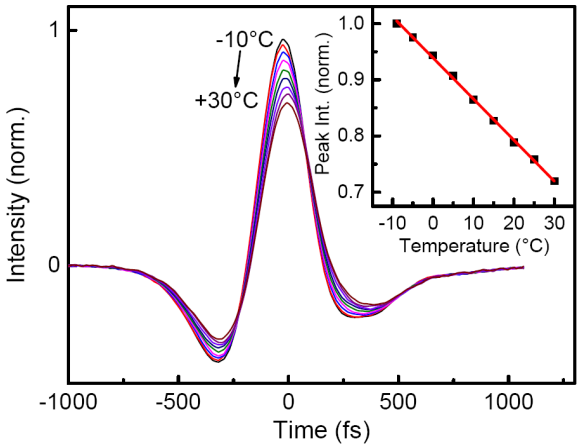

Figure 5.4: THz transmission through the thermalized cuvette as function od temperature. Figure adapted with permission from Ref[116]

the 2D response along the t_1 axis where the signal is maximum (right-hand side of Fig 5.5). It is a square-like response that extends for about 500 fs, whose peculiar shape arises from propagation effects, specifically, from the temporal walk-off between 800nm and probe during propagation inside the material[117]. Indeed, the refractive index of sapphire is 3.08 at 1 THz and 1.76 at 800nm thus, after propagating through 0.1 mm of sapphire, the THz pulse lags behind the probe by about 500 fs. This large velocity mismatch between 800nm and THz gives rise to the square shape response, whose temporal length is proportional to the thickness of the material. Another way to describe it is by thinking about it as the main lobes of the IRF (Fig 3.6) stretched along the length of the window. The change of sign along the t_2 axis follows the change of sign of the IRF, arising from the derivative in Eq 3.7.

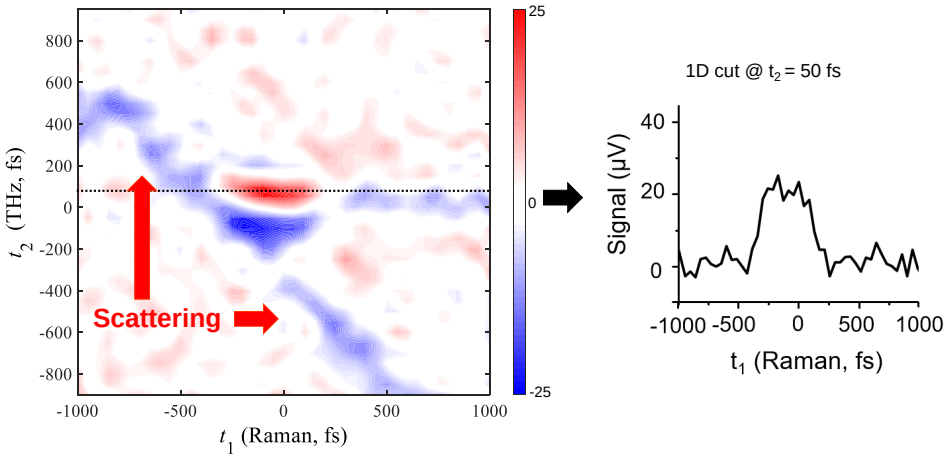

Figure 5.5: 2D Raman-THz response of 100 μm sapphire window. On the left a 1D cut at $t_2 = 50$ fs (black dashed line), where the response is maximum.

5.3 2D Raman-THz spectroscopy of water in the cell

After the characterization of the response from the window, we measure the 2D Raman-THz response of water in the cell. The size of the signal turns out to be about one order of magnitude smaller than the one whit the jet and thus, to be able to achieve acceptable SNR, the measurement time increases significantly.

5.3.1 Scattering

Before analyzing the actual response from water, we observe a new signal showing up on the 2D map, labeled as 'scattering' in Fig 5.5. It is about the same intensity of the window response and it extends antidiagonally, like the IRF(see Fig 3.6). This new feature is an artifact stemming from the Raman beam and it is consequence of two factors: first, the introduction of the cell and second, the removal of the generation beam chopper described in chapter 3. We use the word 'scattering' to describe the 800 nm light that is

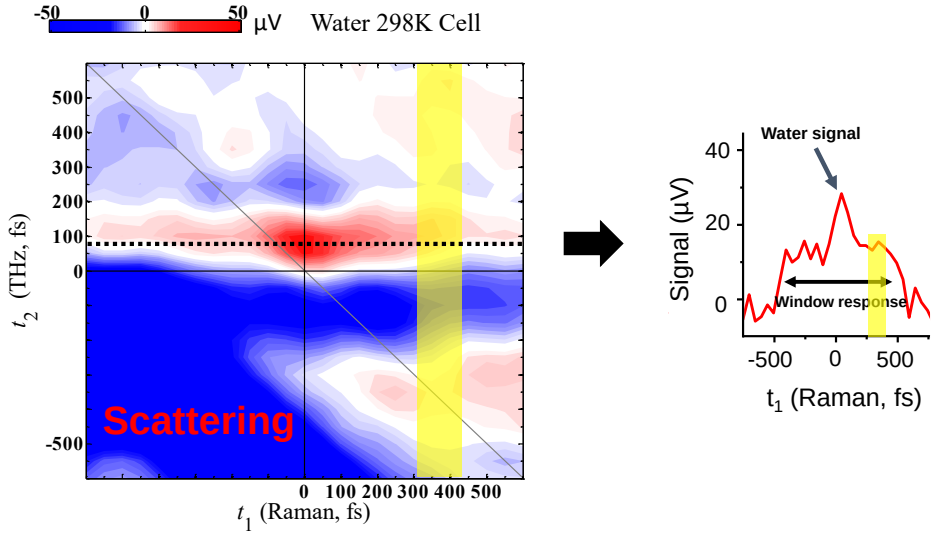

Figure 5.6: 2D Raman-THz response of room temperature water in the cell and 1D cut at $t_2 = 50$ fs to show the window response and the water signal.

scattered forward when there is a refractive index mismatch, in our specific case the air-sapphire or water-sapphire interface. Delay t_1 is adjusted such that the Raman and THz pulses are temporally overlapped on the sample; this means that, since 800nm light travels faster than THz light in sapphire, the Raman pump lags behind when the THz pulse hits the first window. Since THz travels slower in water as well, the opposite is true for the second window, that is THz will lag behind with respect to 800 nm light. Most of the Raman pump, after interaction with the sample, is coupled out of the system through a hole on the second elliptical mirror but the light that underwent scattering from the different interfaces on the beam path does not propagate in a straight line and therefore will be collected and focused on the detection crystal, exactly like the THz pulses. Provided that travel time of scatterd 800 nm light is shorter than THz through the whole sample cell, it will hit the detection crystal before the real signal triggering some nonlinear effects when interacting with the detection beam inside the detection crystal, which we detect as a negative transient signal. It extends along the antidiagonal,

as for the IRF, because delays t_1 and t_2 move in opposite direction in our specific experimental layout. This temporal walk-off between scattering and water signal is about 700 fs, sufficiently large to, tentatively state that one does not affect the other and thus just neglect the lower left quadrant in the analysis of the water response. Interestingly, if one were to employ the double chopping approach, scattering would not be an issue as it would be one of the four state of the system (specifically S_{10} in Eq 3.5 of chapter 3) and thus would be subtracted directly in the calculation of the transient signal. This direct subtraction, however, would come at the price of a significant increase in measurement times. That is why, given that the scattering is far enough from the main water response and therefore can be neglected, we chose to employ the single chopper approach.

5.3.2 Room temperature water

In Fig 5.6 is presented the 2D Raman-THz response of water in the cell at room temperature. Around $t_1 = t_2 = 0$ of the 2D response, we can identify the characteristic positive and negative lobes of the IRF. In the lower left quadrant, we recognize the quite intense scattering contribution: its intensity is higher in the case of the entire sample cell,. since we have more scattering interfaces (air-sapphire, sapphire-water, water-sapphire, sapphire air). Provided that electro-optic sampling measures the electric field of the emitted signal from the sample, we expect the window response of Fig 5.5 and the signal from water to be additive, that is, they will be on top of one another. Indeed, if we now take a 1D cut along where the signal intensity is maximum (horizontal dashed line in Fig 5.6), we observe that on top of the square-like shape window response sits the sharp signal from water. The first important test for the measurement of the water in the cell is to compare the echo decay of the diagonal feature along $t_1 = t_2$ to the reference measurement of the windowless water jet. Once the comparison is somewhat reliable, we can be confident that the two sample systems are equivalent and carry, qualitatively, the same information. In order to adequately compare the diagonal decay with the jet measurement we need to take out the window

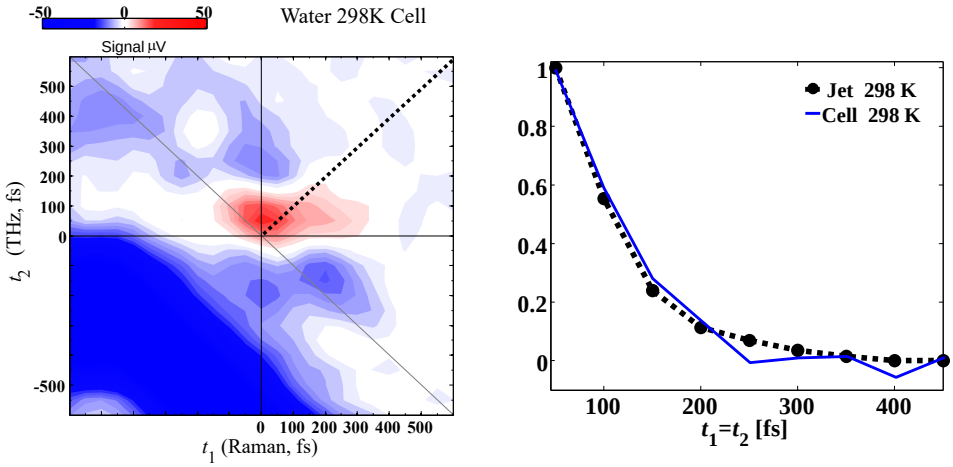

Figure 5.7: 2D Raman-THz response of water in the cell at room temperature and comparison of the diagonal decay with the one of Ref [4].

response. It is important to note that the temporal length of the window response, in the case of the cell, is doubled because we have now two windows, one in the front and one in the back. The easiest and more straightforward approach, but also the less rigorous, is to physically subtract the window response from the 2D response. To do so, we take a vertical slice of the 2D response, far enough from the maximum of the water signal but still within the 'box' of the window response (yellow shaded rectangle in Fig 5.6), and we subtract it from the whole map. The result is shown in Fig 5.7 on the left-hand side. Qualitative similarities with the 2D Raman-THz jet response of water of Fig4.2a can be observed: for example, the main positive and negative lobes of the IRF. We can now take a diagonal cut along the dashed line and compare the normalized decay with the one of the jet measurement of Ref[4] (right-hand side of Fig 5.7). We observe a good qualitative agreement between the two, although the trailing part of the decay related to the cell shows, as expected, worse noise performance. Despite a predictable drop in the data quality, the evidence is that the two sample systems are equivalent to a sufficient extent and thus we conclude that the measurement at different temperatures can be trusted, although only to a qualitative degree.

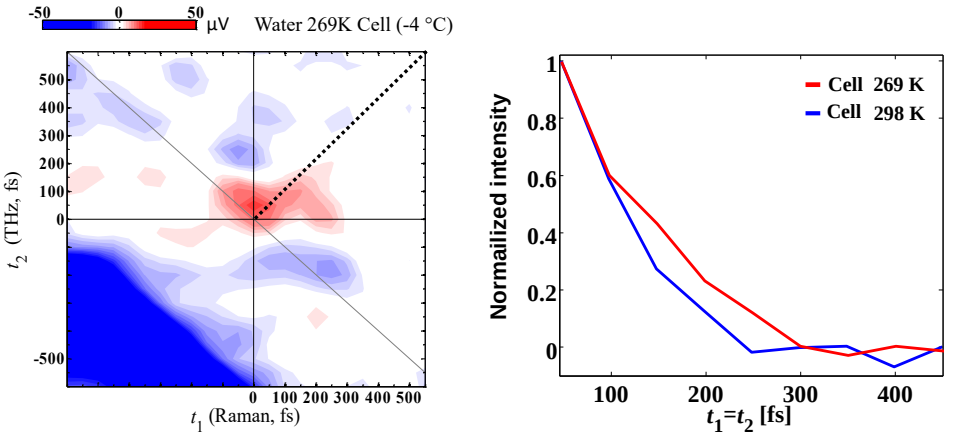

Figure 5.8: 2D Raman-THz response of slightly supercooled water at 269 K and echo decays comparison.

5.3.3 Slightly Supercooled water

The lowest and only temperature at which a 2D Raman-THz response of slightly supercooled water was successfully measured is about 269±1 K, a temperature higher than the lowest achievable (263 K). The reason for this somewhat higher temperature is a consequence of the fact that a single measurement needs an extremely long time to reach an acceptable SNR (on the order of 7-10 days of averaging) and thus the sample needs to remain liquid during the entire data acquisition. 269 K turns out to be the lowest temperature where freezing can avoided on the timescale of the experiment. Fig 5.8 presents the response for the slightly supercooled water sample after subtraction of the window response. Apart from the scattering contribution, which is now further apart from the center of the map since slightly thicker windows were used, the two 2D responses of Fig 5.8 and Fig 5.7 look different around the main peak of the signal and, more importantly, comparing the decays along the echo direction there is a clear extended relaxation component for the 269 K case with respect to the room temperature one.

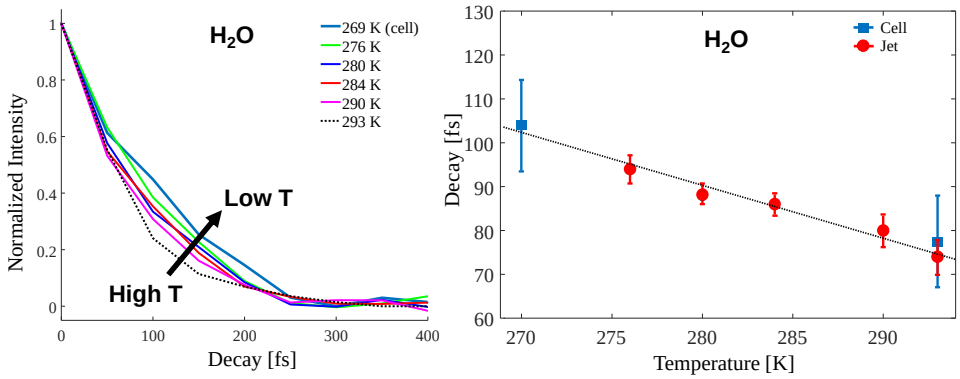

Figure 5.9: Trend of the echo decays for cell and jet measurement as function of temperature. The dashed line on the left-hand side is just to guide the eyes.

5.4 Discussion and Conclusion

The slower dynamics observed for the case of water at 269 K might be a signature of an enhanced structural relaxation of the collective hydrogen bond network. Therefore, it can be connected with the discussion of the previous chapter and Ref[68], thereby taking as a reference the trend of Fig 4.3 for H_2O. The left-hand side of Fig 5.9 compares the normalized diagonal cuts on a visual level, where the decays become slower as temperature is decreased. For a more direct, although still qualitative comparison, on the right-hand side of Fig 5.9 the values of the decays for the cell at room temperature (78±10 fs) and at 269 K (105±10 fs) are plotted together with the ones obtained with the jet as function of temperature. The error bars of the cell points are substantially larger because they have not been evaluated with the standard deviation of the signal-free left-bottom quadrant, as for the jet case (see the section Methods of Ref[68] or previous chapter). The cell responses are contaminated by the scattering signal in that quadrant and thus the error has been calculated by block averaging.

Keeping the analysis qualitative, one can see in Fig 5.9 that trend discussed in Ref[68] can be extended: as water molecules are 'colder', they form

collective intermolecular structures that are stable for longer times, since the extent of the diagonal decay correlates directly with the lifetime of this structures.

Even though, for now, the measurements in the cell can be discussed and compared only on a very qualitative level, they constitute a valuable learning step for further technical improvements. Such knowledge sets a starting point for the development of more efficient methods to achieve lower temperatures and better SNR.

Chapter 6

2D Raman-THz spectroscopy of halogenated liquids

This work has been published in The Journal of Physical Chemistry Letters, see Ref. [69].

Contribution to this paper

Gustavo Ciardi carried out the experiments, analyzed the data and wrote the paper. The experiment, together with the data analysis were performed in collaboration with Dr. Andrey Shalit and Arian Berger.

6.1 Introduction

The spectral properties of liquids in the Terahertz (THz) frequency range reflect the thermally populated ($\leq k_B T$=200 cm^{-1}) intermolecular degrees of freedom, such as, for example, hydrogen bonds and hindered rotation which are ultimately responsible for the bulk properties of liquids and processes like solvation[118, 119]. It is, however, challenging to follow and monitor such properties in detail due to the, generally, ultrafast timescales at which they occur. In one-dimensional spectra, fast dephasing and the large anharmonicity of the modes leads to a significant broadening of any spectral feature, both

in Raman[25, 26, 27] and THz spectroscopy[18, 17, 28], limiting the amount of information that is possible to extract. Multidimensional spectroscopies, whose properties have been discussed in chaprter 2, turned out to be a powerful tool to partly circumvent this problem by spreading the spectra along multiple frequency axes; well-known methods as NMR spectroscopy and 2D infrared spectroscopy have demonstrated this very concept with the help of devised pulse sequences, successfully managing to retrieve detailed structural information and broadening mechanism of nuclear spins[30] and intra-molecular vibrations[29, 120].

In order to understand the capabilities of 2D Raman-THz spectroscopy, we need a model system with sharp and well defined vibrational modes in our detection window. Thanks to their spectral properties, halogenated liquids, as for example chloroform, carbon tetrachloride, bromoform, diiodomethane and dibromomethane, turn out to be a perfect category of compounds for this purpose. In one dimensional low-frequency spectra like the ones shown in Fig 6.1, they show very narrow intramolecular modes (typically symmetric and asymmetric bending modes) in the window 100-600 cm^{-1} together with the intermolecular degrees of freedom, expected in the region 1-100 cm^{-1} for any liquid. The wealth of modes of such compounds in this frequency range can be extremely helpful to shed light on the potential of 2D Raman-THz spectroscopy.

These very liquids are the same that have been investigated by Blake and coworkers with the THz-THz-Raman pulse sequence[56, 60, 61].

6.2 Results and discussion

Fig. 6.2 shows the 2D Raman-THz signal for liquid bromoform ($CHBr_3$), with the color scale saturated such that the oscillating signal stands out. As already outlined in chapter 3, the delay lines' arrangement in our 2D Raman-THz experimental setup allows to generate two distinct pulse sequences: the Raman-THz-THz (RTT) and the THz-Raman-THz (TRT) sequences. Delay t_1 is defined as the time between the first (Raman for RTT sequence and THz for TRT sequence) and the second (THz for the RTT and Raman for the

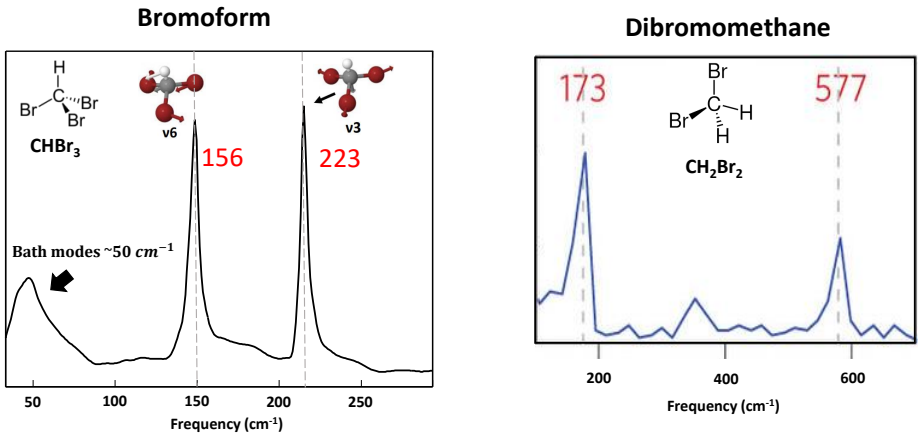

Figure 6.1: One dimensional Raman spectrum of bromoform and dibromomethane. The spectrum on the left-hand side has been digitalized and adapted from Ref[8], the one on the right-hand side from Ref[51].

TRT) excitation pulses, whereas t_2 as the time between the THz excitation pulse and the emitted THz field. The part of the experimental data around $t_1 = t_2 = 0$ up to $t_1 = t_2 = \pm 0.7$ ps is where the two pump-pulses overlap in time.

6.2.1 Raman-THz-THz pulse sequence

For the RTT quadrant (yellow-shaded in Fig 6.2), the signal extends significantly beyond that region along the t_1 direction, even beyond our measurement window, while being very short lived along t_2. This long-lived dynamics allows us to analyze the signal starting from a t_1 delay >0.7 ps (see black vertical dashed line in Fig. 6.2), where we can safely neglect the contribution from the pulse overlap.

Fig. 6.3a shows a 1D cut along t_1 delay where the signal intensity is the highest (i.e. $t_2 = 0.1$ ps). The signal consists of an oscillating component atop of an exponential decay, the latter of which reflects the alignment of molecules along the polarization direction of the Raman pulse and their relaxation to equilibrium. A single exponential fit reveals a timescale of

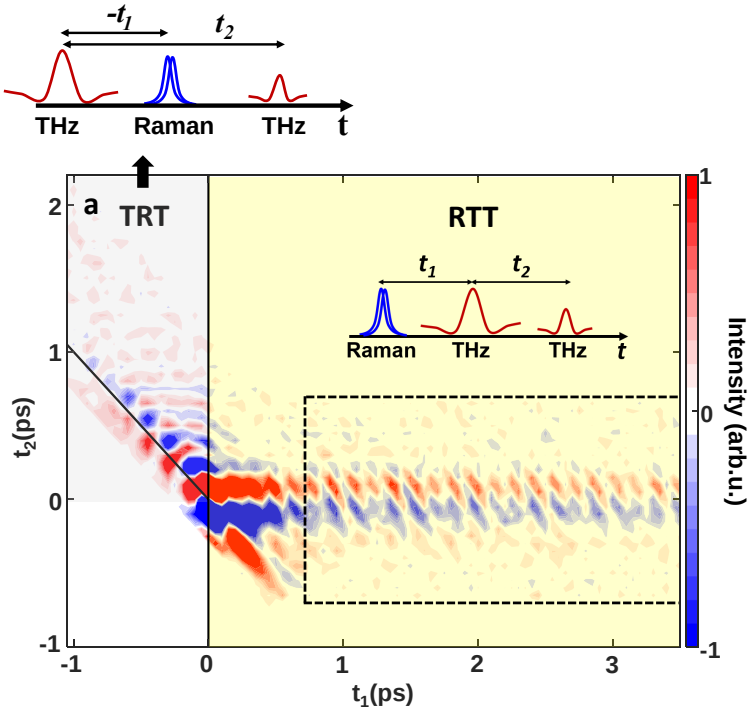

Figure 6.2: Experimental 2D Raman-THz data for bromoform; the region of the Raman-THz-THz sequence is shaded in yellow, that of the THz-Raman-THz in grey.

$\sim$2.5 ps, in agreement with the typical timescales found in optical Kerr effect (OKE) experiments for bromoform[121] or related liquids[122, 123, 27, 124]. By subtracting the single exponential fit from each 1D cut along t_1 direction, we can isolate the vibrational signal (Fig. 6.3b).

Fig. 6.4a shows in red the absolute-value of the 2D Fourier transformation of the data in Fig. 6.3b. Three strong peaks are clearly visible in the non-rephasing quadrant with $f_1, f_2 > 0$, labeled as A, A' and B, together with a weaker one in the rephasing quadrant ($f_1 < 0, f_2 > 0$), labeled as C. The peaks are relatively narrow along the f_1-axis, where the frequency positions correspond to the well-known intramolecular vibrational modes ν_6 ($\sim$4.7 THz for peaks A, A' and C) and ν_3 ($\sim$6.7 THz for peak B) of bromoform. These peaks correspond to the doubly degenerate, asymmetric C-Br bending mode

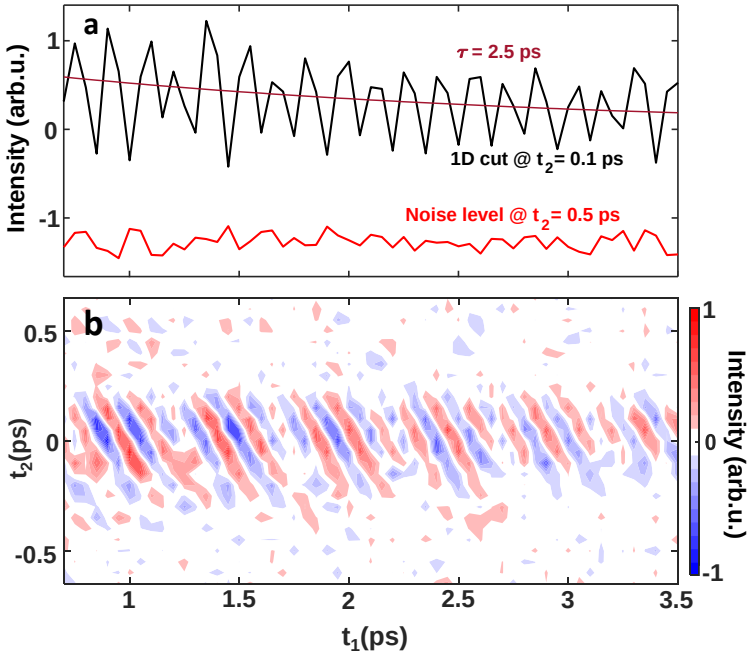

Figure 6.3: (a) 1D-Cut of the signal for $t_1 \geq 0.7$ ps at $t_2 = 0.1$ ps. (c) Zoom of Fig 6.2 with the exponential decays subtracted.

and the symmetric C-Br bending mode, respectively, and are seen both in one-dimensional Raman and THz spectra[60, 8]. Along the f_2-axis, peaks A and B are significantly broader with maxima at ∼3.5 THz. This frequency neither matches any of the fundamental modes of bromoform, nor difference frequencies of modes. Peak C in the rephasing part is about four times weaker than the non-rephasing bands and it peaks at a lower frequency (1.8 THz) along f_2.

To understand and assign this 2D Raman-THz spectrum, we have to consider very explicitly the instrument response function (IRF) of the system shwon in Fig. 3.6(a), starting from Eq.3.7 and Eq.3.8 in chapter 3. We can write Eq. 3.7 as a convolution (i.e., ⊛) of the molecular response function $R(t'', t')$ with the IRF[108]:

$$E^{(3)}(t_1, t_2) = IRF(t_1, t_2) \circledast R(t_1, t_2). \tag{6.1}$$

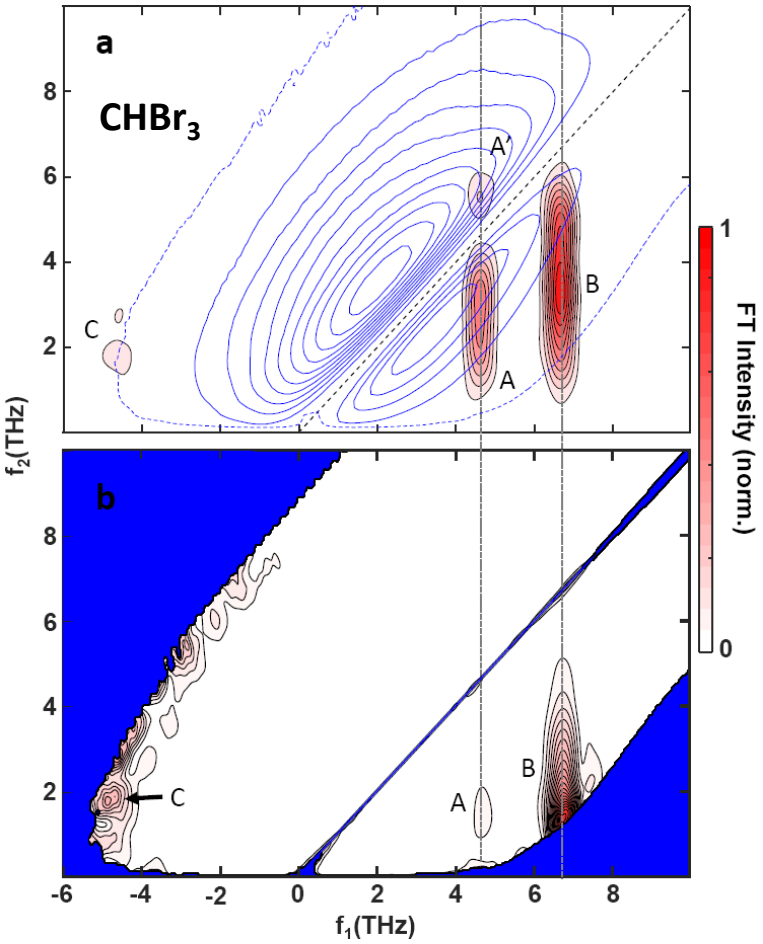

Figure 6.4: (a) Absolute-value of the 2D Fourier transformation for the bromoform data in Fig. 1.1b (filled red contours) overlaid with that of the IRF (the blue solid contour lines are in steps of 10% of the maximum value, and the 1% contour line is added as blue-dashed line). (b) The bromoform data from panel (a) after deconvolution. The blue areas blank out those parts where the IRF is too small to trust the deconvolution, i.e. applying a threshold of 0.5% of the maximum amplitude of the IRF. The arrow marks peak C after deconvolution.

Applying the convolution theorem:

$$\tilde{E}^{(3)}(f_1, f_2) = I\tilde{R}F(f_1, f_2) \cdot \tilde{R}(f_1, f_2), \tag{6.2}$$

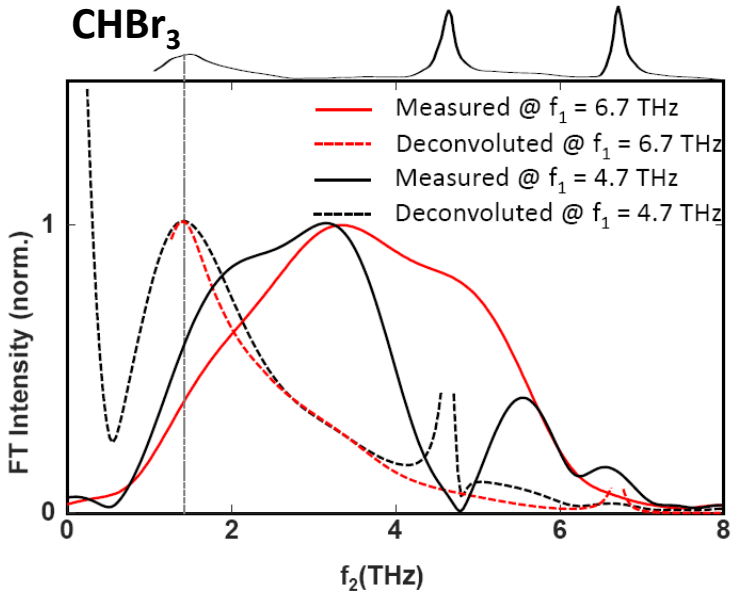

Figure 6.5: Measured (solid lines) and deconvoluted (dashed lines) 1D vertical cuts along the f_2-direction for f_1 corresponding to the fundamental intramolecular vibrations. The 1D-Raman spectrum of bromoform is shown on top (digitized from [8]).

we see that the 2D Raman-THz spectrum in the frequency domain becomes a product of the Fourier transformation of the molecular response function $\tilde{R}(f_1, f_2)$ with that of the instrument response function $I\tilde{R}F(f_1, f_2)$. The absolute-value of the latter is shown in Fig. 6.4a as blue contour lines. Most of its amplitude resides in the non-rephasing quadrant (i.e., $f_1, f_2 > 0$) and it consists of two lobes divided by a nodal line on the diagonal where f_1=f_2; another zero-amplitude line lies along the f_1 axis. It becomes evident from Fig. 6.4a how the spectral shape of the IRF is imprinted on the measured response, especially along the diagonal node (i.e. f_1=f_2) that "splits" the peak at f_1=4.7 THz. In fact, the doublet A and A' originate from one and the same peak, and A' is just the extension of A above the diagonal line.

We can derive the "real" molecular response by dividing the measured spectrum through the IRF (Fig. 6.4b blue contour lines), thereby effectively deconvoluting the data. The deconvolution is defined only in certain parts

of the spectrum, while regions, in which the IRF is too small for the deconvoloution to be reliable, have been blanked out in Fig. 6.4b (blue areas). Three conclusions can be drawn from the deconvoluted spectrum: First, f_1 of peaks A and B do not change; they still encode the fundamental intramolecular modes ν_6 and ν_3. Secondly, the relative intensities of these peaks change significantly, rendering the higher frequency peak B much more intense. Thirdly and most importantly, the peaks shifted significantly in f_2 towards lower frequencies with maxima now around $f_2 \approx 1.3$ THz. This shift becomes even more evident when plotting in Fig. 6.5 1D cuts along the f_2-axis for f_1-positions that correspond to the fundamental modes, i.e., $f_1 = 4.7$ THz and $f_1 = 6.7$ THz. Comparing these cuts with the 1D Raman spectrum (plotted atop of Fig. 6.5)[8], we conclude that they coincide with the broad shoulder that is commonly attributed to the intermolecular modes of the liquid at around ∼1.6 THz. The band is typically assigned to librational motions of the molecule that are seen universally in polar liquids[125, 8]. The cross peaks can thus be assigned to the coupling between the sharp intra- and the much broader intermolecular modes of the liquid. This coupling is much stronger for the higher frequency mode ν_3. Even though we do presently not understand why that might make a difference, we note that ν_6 is a doubly degenerate mode, while ν_3 is singly degenerate. Peak C in the rephasing quadrant is situated very much at the edge where the deconvolution becomes unreliable (marked by an arrow Fig. 6.4b). We can nevertheless conclude that its f_2 peak position is less affected by the convolution with the IRF (we derived 1.8 THz from Fig. 1.2a), since its position is close to the maximum of the IRF in the f_2-direction, i.e., since the 1% contour line (Fig. 1.2a, dashed blue) crosses that peak vertically. To second our interpretation of intra-/inter molecular coupling, we considered other halogenated molecules, with an even simpler 1D spectrum with only one intramolecular mode in our detection window. The first one is diiodomethane (CH_2I_2 with the C-I bending mode ν_4 at 3.7 THz). Applying the same procedure to the data as for bromoform, the measured and deconvoluted spectra are shown in Fig. 6.6a and b, respectively, and the 1D cuts along f_2 in Fig. 6.8. It can be seen again how strongly the IRF affects the data, splitting the peak

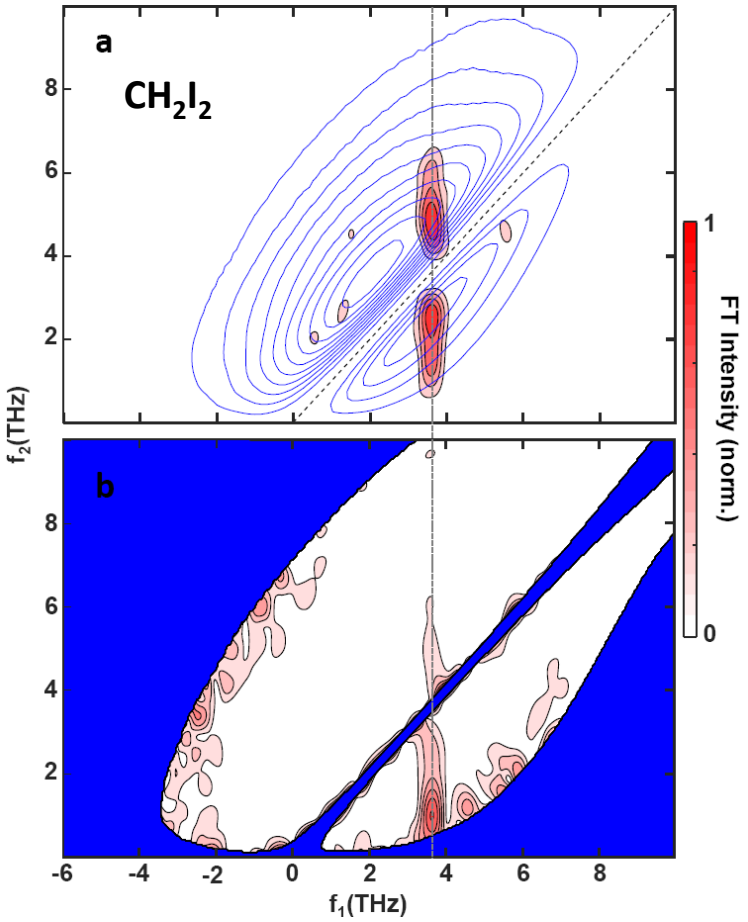

Figure 6.6: Same as Fig. 6.4, but for diiodomethane with only one intramolecular mode in the accessible frequency range. In panel (b), the threshold, above which the deconvolution was deemed to be reliable, was set to 5% of the maximum amplitude of the IRF.

into two parts. This effect is even more pronounced than for bromoform, since the mode is lower in frequency. Analyzing the the spectra before and after deconvolution, we arrive at the same conclusions as for bromoform: the peak position in f_2 is shifted downwards significantly upon deconvolution into a spectral region, in which intermolecular modes are expected (to our

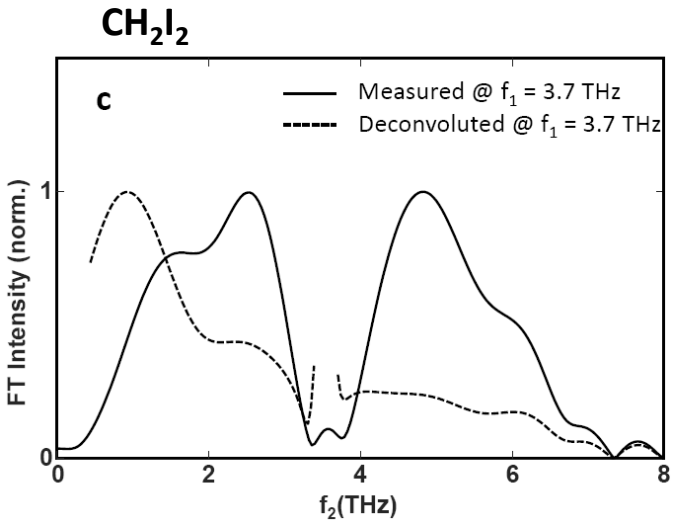

Figure 6.7: 1D cut as in Fig. 6.5, but for diiodomethane.

knowledge, the 1D spectrum of this molecule below 3 THz is not present in literature). The other molecule is dibromomethane (CH_2Br_2, with the C-Br bending mode at 5.7 THz[51]). The non-rephasing part of the measured 2D spectra of this molecule is shown in Fig 6.8. Although the quality of this specific data is not sufficient to exctract realiable deconvoluted spectra (these sample was extremely volatile and have a lower pump-induced damage threshold compared to bromoform and diiodomethane), we can qualitatively see the same behavior with respect to the IRF as for the other molecules, especially looking at the continuation of the peak above the diagonal for dibromomethane. That is, the IRF shapes the spectrum significantly and the frequency position along the f_2-axis is not the real one but it is again an "artifact" of the convolution with IRF. The f_1-positions are still encoding the fundamental vibrational modes. Bromoform, among other molecules, has been investigated by Blake and coworkers with the TTR pulse sequence[60, 61], while our experiment uses an inverted RTT pulse sequence. In either case, one of the interactions must induce a two-quantum transition[42], which would be forbidden in the harmonic approximation. In order to reveal a cross peak between two degrees of freedom, that two-quantum transition must

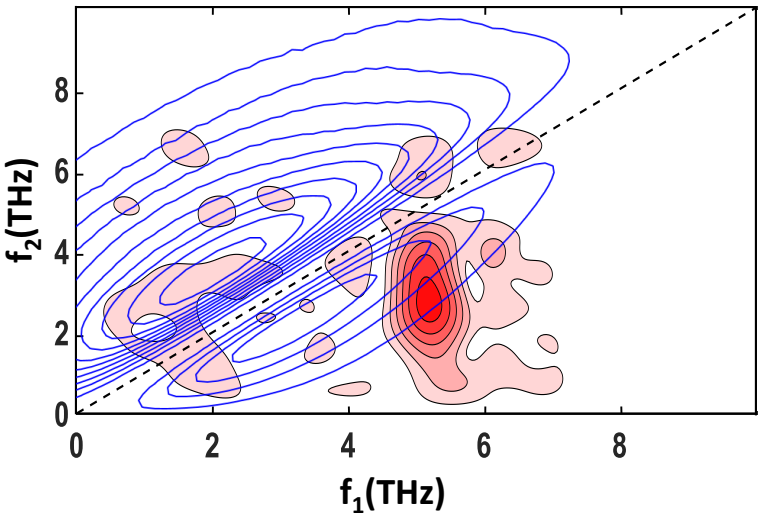

Figure 6.8: Measured 2D Raman-THz spectrum of dibromomethane

be in the middle of the pulse sequence, de-exciting one mode and exciting another one at the same time. Both pulse sequences have a THz interaction in the middle, hence we conclude, just like Blake and coworkers[60, 61], that the source of anharmonicity is mostly related to the dipole function of the system.

Based on their frequency positions, however, Blake and coworkers assigned a sequence of cross peaks to couplings between two intramolecular modes, involving thermally excited states[60, 61], while we assign the one observed cross peak to intra/inter molecular couplings.

The mechanical anharmonicities of the intramolecular modes of bromoform are very small[126], while one might expect that those of intermolecular degrees of freedom are significantly larger. Furthermore, the very fact that the 2D Raman-THz spectrum of diiodomethane (and to certain extent also the one of dibromomethane) shows the same cross peak and rules out any possible intra-/intra molecular coupling, as that molecule has only one mode (ν_4) within the frequency window of our experiment. The next higher in-

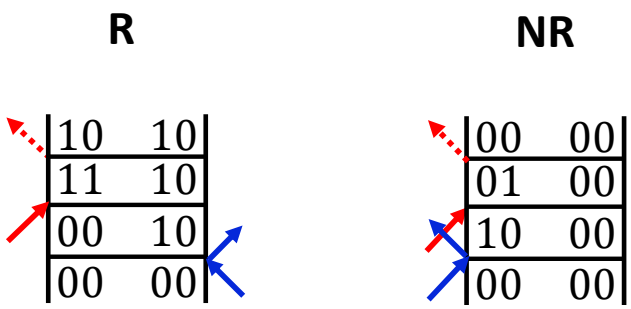

Figure 6.9: The Feynman diagrams describing the peaks in the spectra. The right diagram is common for all the non-rephasing peaks in bromoform, diiodomethane and dibromomethane. The rephasing one refers to peak C in the spectrum of bromoform.

tramolecular mode, ν_3 at $\approx$ 15 THz[24] (17 THz for dibromomethane[51]), is clearly beyond that frequency range, and thermal excitation becomes small (<10%) as well. Apparently, the two techniques, THz-THz-Raman vs Raman-THz-THz-Raman, are complementary, going through different coherence pathways, and are sensitive to a different set of anharmonic couplings.

The pathways that lead to the appearance of the peaks in the spectrum can be visualized with the language of Feynman diagrams described in chapter 2. In this case the notation for the states is made up by two numbers, the first indicating the quanta of excitation in the specific intramolecuar mode, the second ones in the intermolecular degrees of freedom.

6.2.2 THz-Raman-THz pulse sequence

The layout of our experimental setup allows to generate simultaneously the two distinct pulse sequences. For the THz-Raman-THz quadrant, the time ordering is not as in the RTT, where t_1 and t_2 represent the delays between the two pump pulses (Raman-THz) and between the second pump pulse and emitted signal (THz-THz), respectively. Here instead, $-t_1$ is the time between the first and second pump pulses (THz-Raman) and t_2 is still the time between the first THz pump pulse and the emitted signal; this time ordering gives the TRT quadrant a triangular shape, shown gray-shaded in

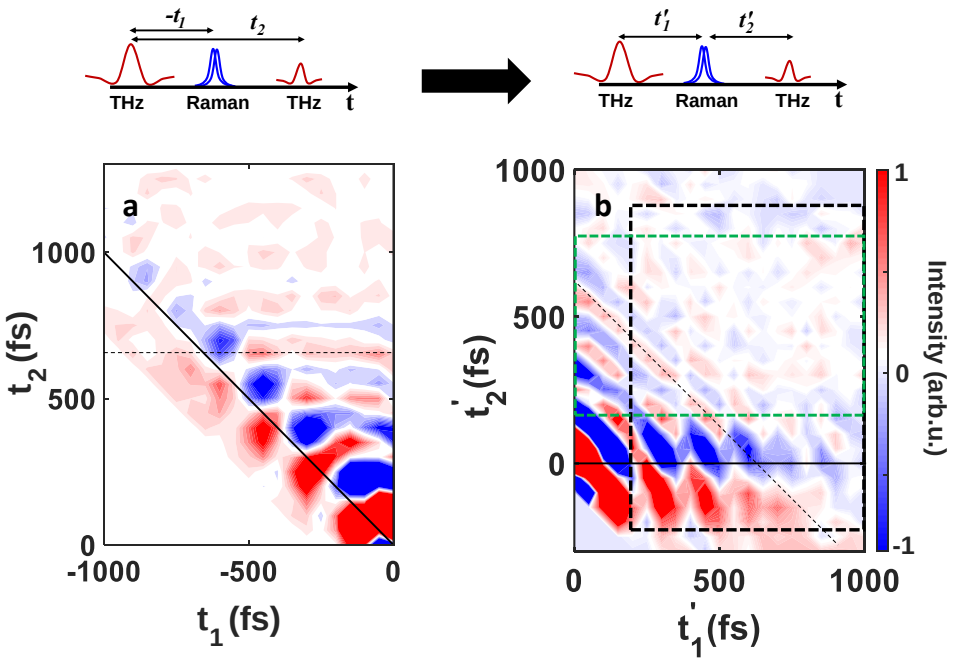

Figure 6.10: In panel (a) the TRT quadrant isolated from the data in Fig 6.2. Panel (b) shows the data after the time coordinate transformation. The black and green boxes refer to different ways to crop the data. See text for details.

Fig 6.2a for bromoform.

In order to visualize the time-domain data of the TRT quadrant in a more intuitive and meaningful manner (i.e. with a consecutive time ordering as for RTT) we need first to apply a time coordinate transformation. We can define two new time coordinates as follows:

$$\begin{aligned} t_1' &= -t_1 \\ t_2' &= t_1 + t_2 \end{aligned} \tag{6.3}$$

The effect of this coordinate transformation on the time-domain data is shown in Fig 6.10. As compared to the RTT sequence, the signal stemming from this quadrant is much shorter lived and confined within the region where the pulse overlap is not yet decayed. This fact renders the proper

extraction of the signal from this quadrant very complicated and less reliable. Nevertheless, we can try to treat the data in the same way as we did for the

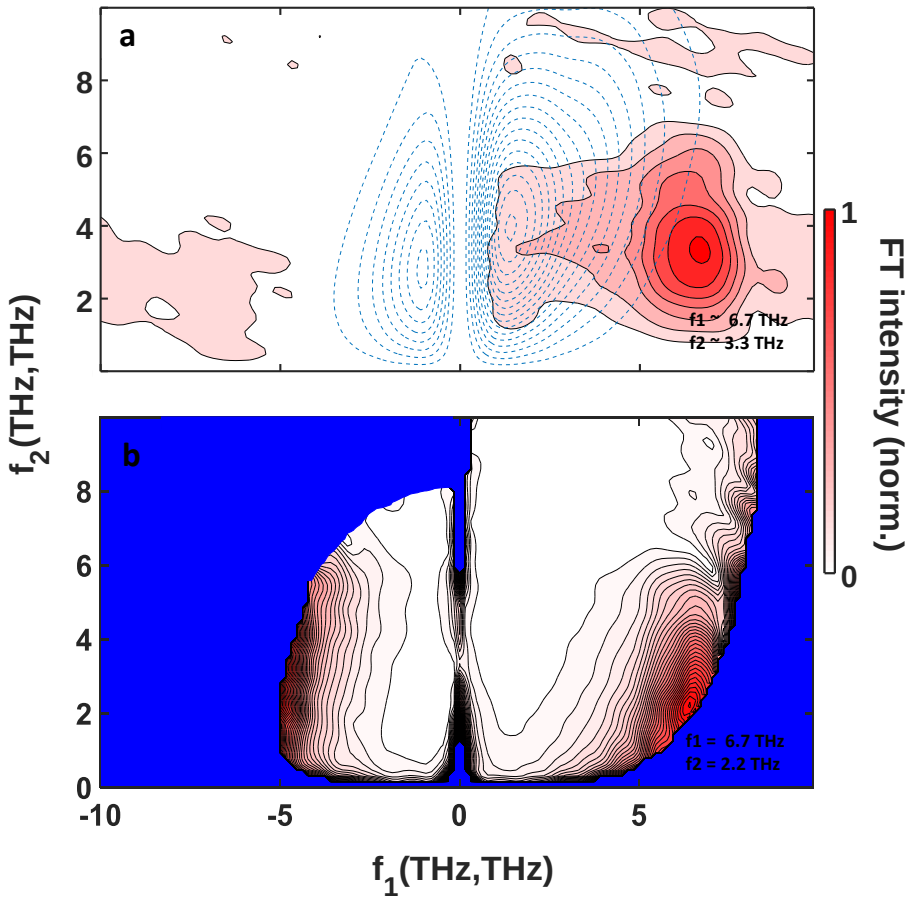

Figure 6.11: In panel (a) the 2D Fourier transform of the data in the black dashed box of Fig 3.6b and in (b) the corresponding deconvolution.

RTT quadrant. The end of pulses' overlap region is harder to define in this quadrant since the IRF extends along t_1' (i.e. the antidiagonal direction in the old time coordinates) to the same extent as the vibrational signal, about 0.7 ps (see Fig 3.6b). If we crop off just the part where the IRF is the most intense (black dashed box) and we apply the same procedure as for the RTT

quadrant, we can plot the absolute value of the 2D Fourier transform, shown in Fig 6.11a, overlaid with the Fourier transform of the IRF (dashed blue lines). Note that both frequency axes now resolve the frequency of the two THz interactions and that the shape of the IRF for the TRT quadrant is different from the one of the RTT quadrant; this is because the above time coordinate transformation affects the time-domain shape of th IRF, and in turn the frequency domain one, in the same way as it affects the measured data. As compared to the RTT, no nodal line is present along the diagonal $f_1 = f_2$ but rather along the $f_1 = 0$ axis, whereas the nodal line along the f_1 axis is present also in this case. Unlike the RTT quadrant, the spectrum shows only a single non-rephasing cross peak and, as expected from the short lifetime of the signal in the time domain, it is very broad in both frequency directions. Despite the significant spectral width, we can find the maximum at $f_1 = 6.7$ THz and $f_2 = 3.3$ THz, almost the same the position of peak B in Fig 6.4. Dividing again by the spectrum of the IRF, we see that the peak shifts downwards, qualitatively resembling the behavior as for the RTT quadrant. The new f_2 position is now ~ 2.3 THz which does not encode any fundamental vibrations and it is too high to be assigned to the intermolecular degrees of freedom, at about 1.6 THz.

At the current stage, the physical process that gives rise to this cross peak is not clear; furthermore the short lifetime gives an high degree of uncertainty and arbitrariness in where it is meaningful to crop the time domain data. That is, different clipping of the full TRT quadrant may give rise to different peak position in the spectrum which in turn lead to different results after deconvolution.

An example of this arbitrariness is given by the spectrum of Fig 6.12 which is the result of the 2D Fourier transformation from the data cropped in the green dashed box of Fig 6.10b. It is very different (now the peak is more diagonal with $f_1 = 6.7$ THz and $f_2 = 6.2$ THz) from the one of Fig 6.11 although the experimental data are the same, just cut out differently. In this case, the deconvoluted data (not shown) turn out to be so noisy that no peak is visible anymore.

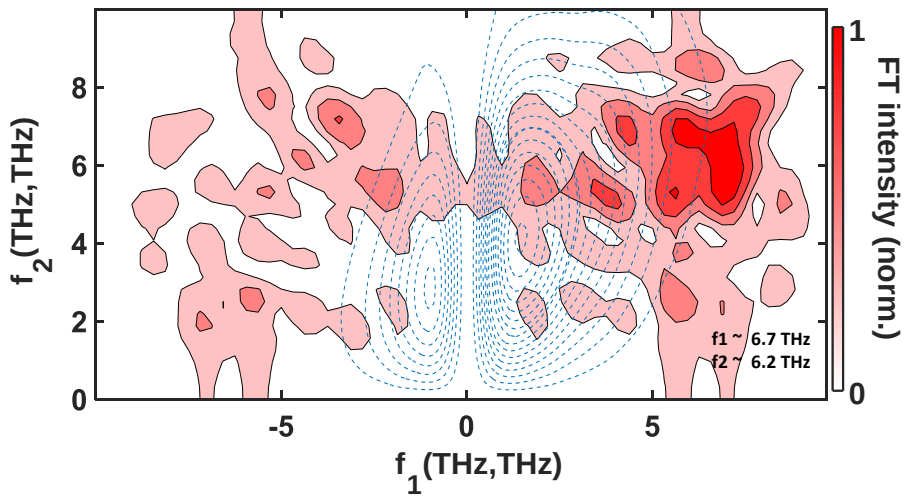

Figure 6.12: Same as for Fig 6.11 but for the data in the green dashed box of Fig 6.10b.

6.3 Conclusion

In conclusion, we have measured the 2D Raman-THz spectrum of different halogenated liquids; in particular the Raman-THz-THz spectra of bromofrom and diiodomethane provide evidence that the observed cross peaks are a signature of coupling between the narrow intramolecular modes of the molecules and the broad continuum related to the intermolecular degrees of freedom of the liquid. The fact that the signal is highly convoluted with the IRF requires a careful analysis in order to extract the real positions of the peaks and in turn the information that these peaks carry. The non-intuitive and complex IRF is related to the intricate shape of THz pulse and therefore it is crucial to take into account the convolution each time the experiments involve one or more THz excitations. The details of the anharmonic coupling between intra- and intermolecular modes are, however, not known at this point and will require significant attention from the theory side. The TTR pulse sequence used by Blake and coworkers[60, 61] and our RTT pulse sequence share a nonlinear THz interaction in the middle as the

one that gives rise to cross peaks, while the third pulse sequence, TRT, does that via a Raman-interaction. Proper extraction and interpretation of that response function will reveal yet another set of anharmonic couplings in these molecular liquids.

Chapter 7

Conclusions and Perspsective

The purpose of this dissertation was to describe, characterize and understand the properties of 2D Raman-THz spectroscopy, a novel two dimensional spectroscopic technique designed to address the information of the low-frequency (< 300 cm^{-1}) modes in liquids. The primary idea was to demonstrate that what one measures with such spectroscopy can be related to the typical information attainable by multidimensional spectroscopies in other frequency regimes (2D NMR, 2D IR).

First, in the context of Fig 2.5, we have resolved the inhomogeneity of the hydrogen bond network induced by the nuclear quantum effects in liquid water through the help of THz photon echoes, as described in chapter 4. The inhomogeneity of the low-frequency modes translates in different structure of these extended hydogen bond networks, whose lifetime is given by the lenght of the echo, that give rise to different vibrations contributing to the broad peak in the 1D spectrum of water in Fig 1.4. Thanks to this and the previous works, this inhomogeneity has been revealed, but the quantification needs participation from the theory side[108]. The ultrafast timescales at which these collective networks interchange have been the primary reason why these dynamics have remained elusive to a large extent. 2D Raman-THz spectroscopy, with its femtosecond time resolution blended with broadband low-frequency sensitivity, has proven itself as the most significant spectroscopy to study the intermolecular structure of water.

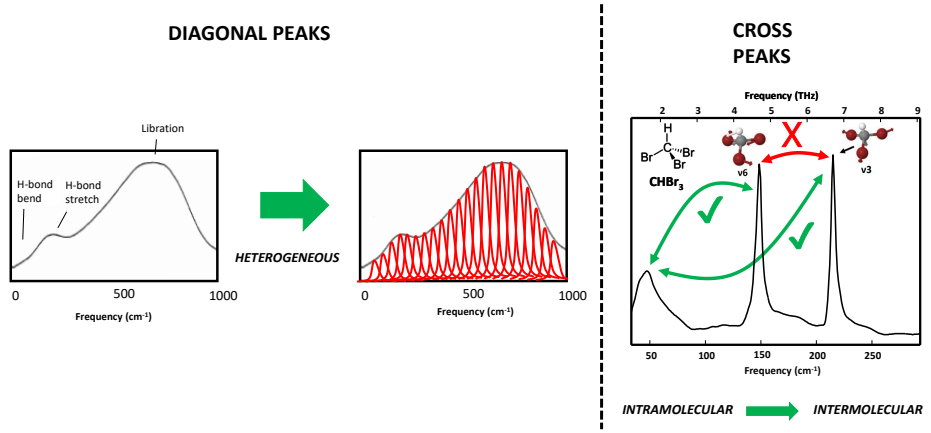

Figure 7.1: "Updated" version of Fig 2.5, summarizing the results that 2D Raman-THz spectroscopy has been able to provide, about the inhomogeneity of water (left) and the coupling mechanism in halogenated liquids (right).

Secondly, we have discovered and characterized the coupling between different types of low-frequency modes in halogenated liquids. The cross peaks in the 2D Raman-THz spectra shown in chapter 6 are a clear signature of the presence of couplings in the low-frequency range, in particular between the intra- and intermolecular degrees of freedom of these molecules: once one excites the sharp intramolecular modes, the energy of these vibrators is subsequently released to the surrounding environment, that is the intermolecular modes of the liquid.

The very fact that one can address and resolve properties, such as inhomogeneity and couplings of various low-frequency vibrations, demonstrates the multidimensional nature of 2D Raman-THz, showing the capabilities of this spectroscopy to reveal in detail many of the molecular properties responsible for the complex dynamics of the liquid-phase to which 1D spectroscopy is blind.

Not less importantly, we have characterized the peculiar Instrument Response function of the system, coming to the conclusion that one can not ignore the effects of the IRF on measured spectra whenever THz pulses are

involved in the experiments. The complicated shape of the IRF, in fact, leads to not intuitive effects that affect both position and intensity of the peaks, whose real nature can only be deduced after having performed the deconvolution. Deconvolution is a delicate operation, as shown in chapter 6 and has to be performed extremely carefully in order to trust the resulting spectra. It comes with an obvious drawback: the quality of the raw experimental data has to be good enough for the deconvoluted spectra to be reliable.

7.1 Outlook

Multidimensional IR vibrational spectroscopy has proved to be a powerful method to gain better understanding of complex liquid-state vibrational dynamics; this knowledge could be extended with multidimensional THz vibrational spectroscopy of liquids to low-frequency molecular vibrations and intermolecular motions that may provide additional insights, for example, into the structural dynamics of water, proteins, and DNA and their chemical properties. In particular, one could study in more detail coupling between water and proteins, eventually extending those measurements in the long run towards relevant biological systems. In this context, 2D Raman-THz spectroscopy has the potential to become an extremely rewarding tool to address fundamental properties of relevant biological systems.

Furthermore, in order to understand even better how the hydrogen bond networks structure water, and in turn to further resolve the intriguing nature of anomalous water behavior, one might target a water regime where low-frequency dynamics are much slower, or even "frozen", than the ones at room temperature. To that end, 2D Raman-THz measurements of deeply supercooled water and/or amorphous ice would prove to be incredibly valuable. A first attempt in this direction has been described in chapter 5. The sueprcooled water experiment turns out to be challenging from all point of views. The introduction of a window material, the cooling system and the need to avoid freezing of the sample combined with the still rather long averaging times allow, currently, to reach only supercooled temperatures right below the freezing point and make the experiment reliable only on a

very qualitative level. Nevertheless, this very attempt sets the foundation for future development of more sophisticated systems that can withstand the technical challenges posed by experiment. The preliminary results, with extended relaxation components along the echo direction as temperature is decreased, already suggest that the insights one might be able address in this water regime could be very fruitful.

From the experimental point of view, the realization of 2D Raman-THz spectroscopy has improved significantly since its first realizations, especially with improvement in the setup, such as the introduction of fast scanning, that have allowed to reduce substantially the acquisition times for each measurement (from about 2 weeks in Ref. [55] to about 1 day in Ref. [68] for the same signal strength). In this regard, a further reduction of acquisition times is possible; our current THz electric fields are quite weak ($\sim$1 kV/cm) and a shift towards generation methods with stronger electric fields, such as plasma generation[127] or organic nonlinear crystals[128] (up to tens of MV/cm), together with higher repetition rate laser sources, could boost acquisition times even more. Along the same line, broader THz excitation spectra would enhance tremendously the amount of information one would be able to address.

Appendix A

Appendix A

A.1 Aqueous solvation from the water perspective

This work has been published in The Journal of Chemical Physics, see Ref[116].

Contribution to the paper

Gustavo Ciardi gave a minor contribution to this paper, performing the temperature dependent THz absorption measurement in Fig. S3 of the supplementary material.

THE JOURNAL OF CHEMICAL PHYSICS **148**, 234505 (2018)

Aqueous solvation from the water perspective

Saima Ahmed, Andrea Pasti, Ricardo J. Fernández-Terán, Gustavo Ciardi, Andrey Shalit, and Peter Hamm
Department of Chemistry, University of Zurich, Zurich, Switzerland

(Received 10 April 2018; accepted 16 May 2018; published online 19 June 2018)

The response of water re-solvating a charge-transfer dye (deprotonated Coumarin 343) after photoexcitation has been measured by means of transient THz spectroscopy. Two steps of increasing THz absorption are observed, a first ~10 ps step on the time scale of Debye relaxation of bulk water and a much slower step on a 3.9 ns time scale, the latter of which reflecting heating of the bulk solution upon electronic relaxation of the dye molecules from the S_1 back into the S_0 state. As an additional reference experiment, the hydroxyl vibration of water has been excited directly by a short IR pulse, establishing that the THz signal measures an elevated temperature within ~1 ps. This result shows that the first step upon dye excitation (10 ps) is not limited by the response time of the THz signal; it rather reflects the reorientation of water molecules in the solvation layer. The apparent discrepancy between the relatively slow reorientation time and the general notion that water is among the fastest solvents with a solvation time in the sub-picosecond regime is discussed. Furthermore, non-equilibrium molecular dynamics simulations have been performed, revealing a close-to-quantitative agreement with experiment, which allows one to disentangle the contribution of heating to the overall THz response from that of water orientation. *Published by AIP Publishing.* https://doi.org/10.1063/1.5034225

I. INTRODUCTION

Dynamic Stokes shift experiments have been among the first ultrafast experiments in the solution phase and have been pursued on numerous molecular systems whenever corresponding nano-,[1] pico-,[2,3] and eventually femtosecond lasers[4,5] became available. This work culminated in a seminal review article by Maroncelli and co-workers.[6] The common picture of the dynamic Stokes shift is shown in Fig. 1. One starts from a thermalized (Gaussian) ensemble in the electronic ground state S_0 of a dye molecule and vertically promotes it to the electronically excited state S_1 with an ultrashort laser pulse according to the Franck-Condon principle. In the S_1, the ensemble will be in a non-equilibrium situation since the free energy curves are displaced with respect to each other. The ensemble therefore relaxes on the S_1 free energy curve on a time scale that we will denote as solvation time τ_S. The relaxation is typically depicted as a reorientation of solvent molecules in the solvation layer. As the ensemble relaxes, the energy gap between the S_1 and S_0 free energy surfaces decreases, which can be observed experimentally as a time-dependent red-shift of the fluorescence or stimulated emission.

For rigid dye molecules with high fluorescence quantum yield in a polar solvent such as water, the dynamic Stokes shift is dominated by the relaxation of solvation degrees of freedom, rather than by intramolecular degrees of freedom, which is why it does not really matter which particular dye is used as a sensor of the solvent response.[7] Even though these experiments measure the dynamics of the solvent, they do it from a solute perspective. On the contrary, here we set out to measure solvation dynamics from the solvent perspective by transient THz spectroscopy. Both perspectives might actually be very different, which can be seen from the in principle well established, but often overlooked and rather non-intuitive fact that the solvation time τ_S and the Debye relaxation time τ_D may deviate significantly. The Debye relaxation time is related to orientational relaxation in the bulk. In the most simple theoretical approach, assuming a continuum model for solvation, a spherical non-polarizable solute molecule, and a single Debye process of the solvent, the solvation time, which sometimes is also called "longitudinal relaxation time," is predicted to be related to the Debye relaxation time[7–12]

$$\tau_S = \frac{2\epsilon_\infty + 1}{2\epsilon_0 + 1}\tau_D, \tag{1}$$

where ϵ_∞ is the dielectric constant from only the electronic polarizability, while ϵ_0 also includes orientational polarizability. In polar solvents, the latter dominates, i.e., $\epsilon_0 \gg \epsilon_\infty$, and Eq. (1) predicts a large separation of time scales between solvation dynamics τ_S and Debye relaxation τ_D. The origin of this time scale separation lies in the very nonlinear dependence of the reaction field R on the dielectric constant ϵ in Onsager's reaction field model

$$R = \frac{2}{r^3}\frac{\epsilon - 1}{2\epsilon + 2}\mu, \tag{2}$$

where r is the radius of the assumed Onsager sphere and μ is the dipole of the molecule. That is, Eq. (1) can be derived from Eq. (2) by plugging in a frequency dependent dielectric constant of a single Debye process,[8]

$$\epsilon(\omega) = \epsilon_\infty + \frac{\epsilon_0 - \epsilon_\infty}{1 - i\omega\tau_D}. \tag{3}$$

In simple words, the nonlinear dependence in Eq. (2) reflects the saturation of the solvent response due to screening; i.e., if the dielectric constant is very much larger than 1 (like for

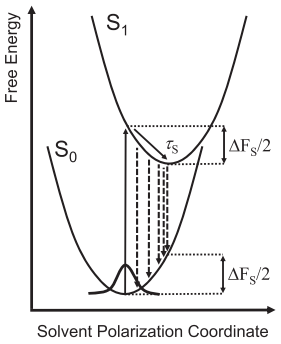

FIG. 1. The textbook picture describing the dynamic Stokes shift of a dye molecule in a polar solvent after electronic excitation. After promoting a thermalized ensemble onto the excited S_1 state, it relaxes with the solvation time τ_S, resulting in a time-dependent red-shift of the fluorescence (dashed arrows).

water), already a thin layer solvates the solute by generating a reaction field R in such a way that the field of the solute's dipole is in essence no longer seen by molecules beyond that layer. If the dielectric constant gets smaller, the size of the solvation layer will get larger, but in such a way that the reaction field will stay almost the same-unless the dielectric constant gets close to 1.

The continuum theory of Eq. (1), obviously, oversimplifies the complexity of the process, which can be seen, for example, from the observed multi-exponential solvation kinetics,[5–7,13] while Eq. (1) would predict a single exponential process. The multi-exponential response has been attributed to many factors, most prominently the failure of the continuum model to account for the discreteness of solvent molecules,[14,15] but also to the fact that the solvent cannot be described by a single Debye process,[16,17] the inertial component of solvation,[9,18] the non-spherical shape of the solute molecule,[16] or translational degrees of freedom that contribute to solvation as well.[9,17,18]

Water is considered to be among the "fastest" solvents with a dominating sub-100 fs inertial component of solvation and a subsequent 800 fs decay, as measured by the dynamic Stokes shift.[5] The solvation dynamics of water have also been measured by a complementary technique, the photon-echo peak shift, revealing three kinetic components (17 fs, 400 fs, and 2.7 ps) and an average solvation time of 400 fs.[13] Given the simplicity of the continuum model, it is remarkable that Eq. (1) predicts a solvation time of 240 fs for water (with $\epsilon_0 \approx 80$, $\epsilon_\infty \approx 1.8$, and $\tau_D = 8.3$ ps[19]), which is quite close to the experimentally observed average solvation time of $\tau_S = 400$ fs (the same semi-quantitative agreement has been found for a wide variety of solvents[6]). From this, one may conclude that the reason for the fast solvation time in water is in fact its large dielectric constant, and not its orientational dynamics *per se*, the latter not being particularly fast with $\tau_D = 8.3$ ps.[19] A recent comprehensive review of the current view of solvation is given in Ref. 7.

To study aqueous solvation from the water perspective, we optically excite a dye molecule and observe the response of the solvent water by transient THz spectroscopy. The THz spectrum of water is related to the dipole-dipole correlation function, whose long-time tail decays exponentially with the Debye relaxation time τ_D. When transiently measuring the THz spectrum of water after exciting a dissolved dye molecule, the expectation is that we observe τ_D rather than τ_S, based on the arguments given above. The present work is in the same spirit as that of Refs. 20 and 21, which, however, studied solvation in organic solvents (probably for reasons of better solubility of the investigated dye molecules), in which case the expected time scale separation according to Eq. (1) is relatively small.

Looking at the problem from a very different angle, the present work is also motivated by the recent observation that solutes, very universally, seem to affect the THz spectrum of a solvation layer that is much larger than commonly assumed (≈10 Å).[22–24] While this interpretation has been strongly challenged, for example by measuring the mobility of individual water molecules with the help of NMR spectroscopy,[25] it has been proposed that the controversy can be resolved by the very delocalized character of THz vibrational modes, which results in correlated motion of many water molecules.[26] If that interpretation is correct, it may be expected that switching the dipole moment of a solute should also affect these delocalized THz modes, resulting in a transient THz signal.

II. METHODS

A. Sample

As sample molecule for this purpose, we chose Coumarin 343, whose solubility in water *per se* is very low (≪ 1 mM). To increase its solubility to 5 mM, we deprotonated, and thereby charged, the dye by the addition of a base (1,4-diazabicyclo[2.2.2]octane, DABCO, 10 mM) to the solution (this base is less nucleophilic than NaOH and thereby prevents degradation of the coumarin due to ring opening). The Stokes shift is 3200 cm^{-1}, as determined from the peaks of the absorption and fluorescence spectra (see Fig. S1 of the supplementary material). The fluorescence quantum yield of a dilute solution of deprotonated Coumarin 343 has been determined to be $\Phi_F = 85\%$ with the help of a Quanta-ϕ integrating sphere calibrated with respect to the reported quantum yield of Coumarin 153 in air-saturated ethanol at room temperature ($\Phi_F = 53\% \pm 4\%$).[27] A fluorescence lifetime of $\tau_F = 4.7$ ns has been measured by time-correlated single photon counting (Horiba Scientific, DeltaDiode DD-395L) in the dilute limit, and we found that it has reduced to $\tau_F = 3.9$ ns at the concentration of the actual THz experiment (5 mM, see Fig. S2 of the supplementary material). We could not reliably measure the quantum yield at these high concentrations due to reabsorption of the emitted light, but we assume that it is reduced by the same factor as the fluorescence lifetime, i.e., $\Phi'_F \approx 70\%$. Finally, we calculated with time-dependent density functional theory at the B3LYP/6-311++G(d,p) level of theory in integral equation formalism polarizable continuum model of water[28] that the

dipole changes by ≈5.3 D when exciting from the ground to the electronically excited state, which agrees well with values reported for the protonated form.[29–31] Note that the absolute dipole moments of the ground and excited states are ill-defined since the molecule is charged; when one chooses the center of nuclear charge as the origin, the dipole increases from 35.2 D in the S_0 to 40.5 D in the S_1 and both are essentially parallel.

B. Transient THz spectroscopy

For the transient THz experiments, we used essentially the same setup as previously described.[32] In brief, pump pulses (400 nm, energy 3.5 μJ) were derived from a 2.5 kHz Ti:S amplifier system (pulse width 120 fs) by frequency doubling in a 0.5 mm thick β-barium borate (BBO) crystal. THz probe pulses were produced by optical rectification in a 0.1 mm thick GaP (110) crystal, generating an almost perfect half-cycle pulse with a FWHM of ≈180 fs (see Fig. S3 of the supplementary material), and detected by electro-optic sampling in a 0.5 mm thick ZnTe (110) crystal, including a recently published concept based on four ZnSe Brewster windows to enhance the detectivity.[33] For a close to diffraction limited imaging of the probe pulses into the sample and into the detection crystal, two computerized numerical control-machined, large-aperture ellipsoidal mirrors have been used. The pump and probe spot sizes in the focus were ≈200 μm. The experimental layout introduces two delay times, the delay t_1 between optical pump-pulse and THz probe pulse and time t_2 that scans the THz pulse. The Coumarin 343/DABCO solution was measured in a 40 μm thick wire-guided water (H_2O) jet[34] to avoid any contamination of the signal from window materials.

As a reference, we also performed an IR-pump-THz-probe experiment, directly exciting the OD band of neat D_2O at 2500 cm^{-1} with 0.7 μJ pulses derived from an IR optical parametric amplifier (OPA).[35] In that case, the sample was held in a cuvette constructed with two 100 μm thin sapphire windows and a spacer of 6 μm. All experiments were performed at room temperature.

Two different pump sources have been used. For experiments with high time resolution, as well as for the IR pump experiment, pump and probe pulses have been derived from the same Ti:S laser system, running the former over an optical delay line. For experiments with long delay times t_1 of up to 50 ns, on the other hand, two Ti:S amplifier systems have been electronically synchronized,[36] revealing an effective time resolution of 10 ps due to the jitter in the synchronization.

C. Simulations

The molecular dynamics (MD) simulation setup is similar to that in Ref. 14 with a large Lennard-Jones sphere solvated in water, thereby mimicking Onsager's solvation model, albeit with a realistic description of the solvent both in terms of its discreteness and dynamics. TIP4P/2005 was used as the water model, whose dielectric constant is $\epsilon_0 = 60$.[37] The Lennard-Jones parameters of the sphere were set to $\epsilon = 0.7794$ kJ/mol and $\sigma = 7.8$ Å, the former being the same as for TIP4P/2005 water and the latter resulting in a sphere radius of 3.9 Å, when considering the corresponding value of TIP4P/2005 (3.2 Å) and the usual combination rule. The sphere was placed in the center of a cubic box of size 25 Å and solvated with 505 water molecules at roughly the experimental density of water. The dipole of the Lennard-Jones sphere was approximated by two point charges separated by 0.8 Å, and the orientation of the dipole was kept fixed during the simulation by restraining these points with harmonic springs. Lennard-Jones interactions were smoothly switched to zero between 10.6 Å and 11.7 Å, and the Coulomb interactions were modelled with the reaction field ($r_c = 10.7$ Å, $\epsilon = \infty$). A time step of 2.5 fs was chosen. The simulation box was equilibrated at 295 K in a 100 ps NVT simulation, thermostated by velocity-rescaling with a coupling constant of 0.5 ps. All simulations were performed with Gromacs.[38]

In order to calculate the non-equilibrium dipole-dipole correlation function of Eq. (4), the following simulation protocol was subsequently used: A 1 ps NVT simulation, introduced to stabilize the temperature, was followed by a 1 ps NVE simulation. From that point on, two 21 ps NVE trajectories were run in parallel: an equilibrium trajectory with the dipole of the Lennard-Jones sphere unchanged and a non-equilibrium trajectory with the dipole changed. In order to accumulate statistics, this protocol was cycled many times (ca. 600 000), continuing from the 21 ps NVE equilibrium trajectory. The simulation parameters were optimized for energy stability during the NVE simulations in order to ensure that the observed temperature change [see Fig. 3(b)] reflects the solvation of the switched dipole, and not any energy drift.

The transient THz response has been calculated from the non-equilibrium dipole-dipole correlation function

$$c(t_1, t_2) = \Delta\langle\dot{\mu}(t_1)\mu(t_1 + t_2)\rangle, \tag{4}$$

where Δ denotes the difference between the non-equilibrium and equilibrium trajectories, t_1 is the pump-probe delay time after switching the dipole of the Lennard-Jones sphere, and t_2 is the time for the THz free induction decay. Time t_1 was evaluated up to 20 ps (of which only 15 ps is shown in Fig. 3) and t_2 up to 1 ps. The dipole $\mu(t)$ contained the contribution of both the Lennard-Jones sphere and all water molecules in the simulation box. This correlation function was subsequently convoluted with the laser pulses to reveal the 3rd-order polarization

$$P^{(3)}(t_1, t_2) = \int_0^\infty \int_0^\infty dt' dt'' E_{THz}(t_2 - t'') \cdot I_{pu}(t_2 + t_1 - t'' - t')c(t', t''), \tag{5}$$

where a Gaussian was assumed for the pump pulse I_{pu} and the second derivative of a Gaussian for the THz pulse E_{THz} (in both cases with a width that matches the experimental pulses). Finally, a time-derivative with respect to t_2 was taken in order to model the emitted 3rd-order THz field,[32]

$$E^{(3)}(t_1, t_2) = \frac{d}{dt_2} P^{(3)}(t_1, t_2). \tag{6}$$

III. RESULTS AND DISCUSSION

Figure 2 (blue) shows the transient THz signal after photoexcitation of the dye molecule, measured at the peak of

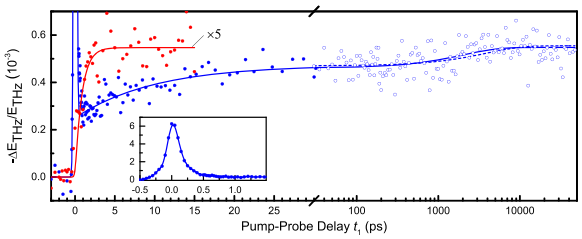

FIG. 2. Relative change of the transmitted THz field E_{THz} measured at the peak of the half-cycle THz pulse. Shown is the response after photoexcitation of Coumarin 343 in water at 400 nm (blue data) or after pumping the hydroxyl vibration of water (D_2O) directly with an IR pulse (red data, smoothed with a 5-point quadratic Savitzky–Golay filter and scaled up by a factor of 5 to match the late time temperature jump in the blue data). The blue filled circles show the data measured with a high time resolution of up to 30 ps plotted on a linear scale, and the blue open circles show those measured with two synchronized laser systems from 30 ps up to 50 ns plotted on a logarithmic scale (both data sets were stitched together by slightly scaling the second one). The solid lines show exponential fits, leaving all time constants as free fit parameters, while the fit shown as the dashed blue line fixes the slowest time constant to 3.9 ns, as determined from the fluorescence decay (see Fig. S2 of the supplementary material). The inset shows the spike around delay zero.

the half-cycle THz pulse ($t_2 = 0$). Two data sets are stitched together in this plot, obtained with the two different pump sources described in Sec. II, thereby covering the time range from 100 fs to 50 ns. Around delay zero, a pulse-width-limited spike of increased THz absorption is observed (see Fig. 2, inset). The spike does not decay to zero completely, but leaves a small pedestal, which is hardly seen in the inset of Fig. 2 and which is what the main panel of Fig. 2 focuses on. This pedestal increases in two steps. The first step, occurring with a time constant of 10 ± 3 ps, agrees within error with the Debye relaxation time of water,[19] while the second step can be fit to a process with 1.9 ns (Fig. 2, solid blue line). The signal stays constant from there on.

It can be safely assumed that water fully thermalizes on a nanosecond time scale over distances, which exceed that between neighboring dye molecules,[39] and we attribute the final pedestal after the second step to the heating of the sample. Indeed, it is known from stationary spectroscopy that the THz absorption cross section of water increases as a function of temperature.[40] To calibrate the effect for our concrete experimental conditions, we measured the transmission of the THz pulse through a thermostated water cuvette of equal thickness at various temperatures and observed a linear dependence with a slope $\Delta T/T = -7.5 \cdot 10^{-3}\ K^{-1}$ (see Fig. S3 of the supplementary material). With that, one can estimate a total temperature jump of ≈0.07 K from the size of the late-time pedestal of the transient THz data (Fig. 2). This number agrees very well with an independent estimate (0.06 K) obtained from the number of absorbed photons per sample volume, their energy, the heat capacity of water, and the fluorescence quantum yield of the dye.

Based on this discussion, we conclude that the second step observed in the transient THz response reflects heating of the bulk solution upon electronic relaxation of the dye molecule from the S_1 state back into the S_0 state. Since the fluorescence quantum of the dye yield is not 100% (we determined a quantum yield of $\Phi_F = 70\%$; see Sec. II), the remaining fraction of dye molecules dissipates their electronic excitation energy into the solvent upon radiationless relaxation, thereby heating the solvent. The fluorescence lifetime, which can be measured much more accurately (3.9 ns; see Fig. S2 of the supplementary material) deviates from the value obtained from the fit of the transient THz data (1.9 ns). We therefore also show in Fig. 2 a fit that fixes the time constant of that process to 3.9 ns (blue dashed line), evidencing that this is still consistent with the relatively poor signal-to-noise ratio of the transient THz data.

In light of the Introduction, we consider the first step, occurring with a time constant that agrees well with the Debye relaxation time of water, the most important result of this study. Before we continue with its discussion, we need to establish the time scale on which the THz absorption responds to an elevated temperature. To this end, we also performed an IR-pump-THz-probe experiment, in which the hydroxyl vibration of water (D_2O) is excited directly (Fig. 2, red data). It is well established from IR-pump-IR-probe as well as from 2D IR experiments that the lifetime of that vibration is ultrafast, in particular, in isotope-pure D_2O as well as H_2O, and that energy thermalizes on a ∼1 ps time scale.[41–48] And, indeed, the THz-absorption rises very quickly with the fit revealing a time constant of 1 ± 0.3 ps (a complementary experiment, THz-pump-IR-probe, highlighting the coherence in the coupling between inter- and intramolecular modes on sub-picosecond time scales, has recently been performed by Bonn and co-workers[49]). Experimental[40] and simulation data (Fig. S4 of the supplementary material) show that the THz absorption increases with temperature throughout the whole frequency range from 0 to 600 cm^{-1}, resulting from a red shift of the librational mode at 600 cm^{-1}. Its low-frequency wing extends into the 100 cm^{-1} regime, where the THz pulses peak, indicating that the mode is almost critically damped. This also explains why the librational mode can respond to an elevated temperature so quickly since a close-to-critical damping is the situation with the fastest possible relaxation. We conclude that the observation of a 10 ps time scale for the first step after photo-excitation of the coumarin dye is not limited by the response time of the THz signal, but rather evidences that the solvent response indeed occurs on that slower time scale.

To get deeper insights into this process, we performed non-equilibrium MD simulations, considering a large Lennard-Jones sphere as solute in water (see Sec. II for details). Figure 3 (blue) shows the result when first equilibrating the system with the dipole of the Lennard-Jones sphere set to zero and then instantaneously switching it on to 7.5 D at $t_1 = 0$, while the red data show the results for the opposite process switching from 7.5 D to 0. When switching the dipole on, the reaction field shown in Fig. 3(a) (blue) can be fit to three exponentials with 7 fs (37%), 210 fs (31%), and 1.6 ps (32%) and an average relaxation time of 590 fs. When switching off the dipole [Fig. 3(a), red], the response is a bit faster with 8 fs (42%), 150 fs (34%), and 1.1 ps (23%) and an average decay time of 310 fs. The slightly different time scale indicates that the system is not quite in a linear response regime, yet, in either case, the result is in very good agreement with the experimental solvation time (400 fs),[13] despite the crudeness of the model.

Figure 3(b) shows the "non-equilibrium temperature" after switching, as determined from the total kinetic energy of the simulation box. When the dipole is switched on (blue), we observe an instantaneous temperature jump followed by a partial decay that can be fit to a single-exponential function with a time constant of 2.2 ps. On the other hand, when switching off the dipole (red), approximately the same initial temperature jump is observed, but the temperature subsequently increases further with a time constant of 3.6 ps. The total amount of dissipated energy upon solvation of the dipole, as measured by the late-time temperature change, is different from that upon re-solvation of the Lennard-Jones sphere without any dipole. Based on Fig. 1, these results might seem surprising. That is, solvation and re-solvation are the equivalents of what would happen on the S_1 electronic state upon electronic excitation and subsequently on the S_0 after emission of a fluorescence photon. Figure 1 would suggest that both events release approximately the same amount of free energy (which is a result of the linear response assumption that renders the curvatures of the S_0 and S_1 free energy surfaces identical). To understand this discrepancy, one must keep in mind that Fig. 1 plots "free energy," while temperature measures "energy." Since solvation is entropy-driven to a significant extent, both terms may be very different. For example, it is a freshman chemistry experiment to observe that dissolution of NaCl in water is endothermic [e.g., temperature may indeed decrease upon solvation, as shown in Fig. 3(b), blue]. Nevertheless, entropy is a function only of the "solvent polarization coordinate" shown in Fig. 1; hence, free energy differences at a given position of that coordinate are in fact the same as energy differences.[9] This is why the dashed arrows in Fig. 1 indeed indicate the energy of the emitted fluorescence photons. Also the total solvation free energy ΔF_S is the same as the Stokes shift ΔE_S. However, while the total solvation free energy splits half/half for the solvation of the excited state and the re-solvation of the ground state, the same is not necessarily true for the splitting of the total solvation energy.

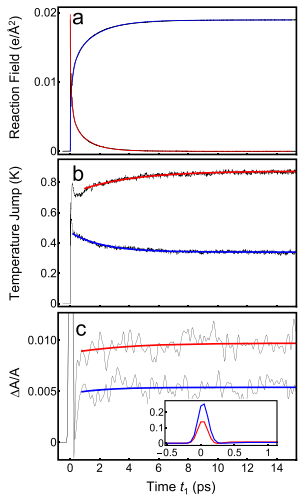

FIG. 3. Simulation results. Panel (a) shows the reaction field $R(t)$ when switching the dipole of the Lennard-Jones sphere on (blue) or off (red), panel (b) shows the solvent temperature in response to the switching (same color code), and panel (c) shows the simulated THz signal in units of relative absorbance change $\Delta A/A$. In either case, the thin black lines present data and the colored lines present single exponential fits. The inset in panel (c) shows the spike around time t_1 zero.

Finally, Fig. 3(c) shows the transient THz response for both switching events, i.e., the result of Eq. (6) along t_1 at the peak of the signal with $t_2 = -50$ fs (the full 2D data set is shown in Fig. S5 of the supplementary material). Around delay zero ($t_1 = 0$), a pulse-width limited spike is observed, just like in experiment [insets of Figs. 3(c) and 2], which represents the electronic contribution from the instantaneous switching of the dipole of the Lennard-Jones sphere. This can be verified by removing its contribution to $\mu(t)$ in Eq. (4), in which case that spike is inverted (and smaller). After the spike, a small pedestal of increased absorbance remains [Fig. 3(c), main panel], which slightly increases further as a function of time in either case [the fit in Fig. 3(c) fixes the time constants to the values obtained from Fig. 3(b) since the data are too noisy and the effect is too small to extract the time scale independently]. While that second step in the simulation results is faster than the Debye relaxation (which is 14 ps for the current simulation setup; see Fig. S6 of the supplementary material), it is still slower than the solvation response [310 fs or 590 fs, see Fig. 3(a)].

Even though Figs. 3(b) and 3(c) resemble each other to a certain extent, evidencing that the THz response can indeed be considered an ultrafast thermometer, they do not do so in all aspects. First, trivially, the initial spike in the THz response is hardly present in the temperature data, as it originates directly from the THz field emitted upon switching the dipole of the Lennard-Jones sphere. Second, while the temperature decreases again after the initial jump when switching on the dipole [Fig. 3(b), blue], the THz absorption continues

to increase [Fig. 3(c), blue]. Third, while the ratio of final temperatures is 2.6 after switching off the dipole [Fig. 3(b), red] *versus* switching it on [Fig. 3(b), blue], the corresponding factor is only 1.8 for the THz response [Fig. 3(c), red, *versus* Fig. 3(c), blue]. Points two and three emphasize that a sizable contribution to the THz response, which reflects the different structuring of water around solutes with different dipoles, exists as well. This is expected since it has been shown that certain solutes affect the THz absorption of solvating water.[22–24,50] For the case when the dipole is switched on, the kinetic response from water orientation actually overcompensates that of the temperature effect. Water reorients on the time scale of Debye relaxation; hence, it appears meaningful that we see that time scale in the THz response. We have no evidence, however, that the orientational response has a different spectral dependence than the temperature response, which would show up as a variation of the t_2-dependence of the THz signal as a function of t_1 (see full 2D data in Fig. S5 of the supplementary material).

With the dipole switched off, the Lennard-Jones sphere is a very hydrophobic particle. Even in that most simple case, the solvation energy and solvation entropy are complicated and not necessarily intuitive functions of parameters such as sphere radius[51] or temperature,[52,53] and one might expect that the situation is even more involved for a real molecule with a complex charge distribution. Anyhow, the simulation of Fig. 3(c) is in very good agreement with the experimental results of Fig. 2, regardless of whether the solute turns into more polar or more apolar upon switching, suggesting that these results are rather universal.

IV. CONCLUSION

In conclusion, we have measured aqueous solvation from a water perspective by means of transient THz spectroscopy. We consider the 10 ps time scale observed for the first step a rather slow process for water. It compares well with the Debye relaxation time, which is the slowest established time scale known for water, suggesting that there is a connection between the two processes. We have also shown that the THz response, for the most part, can be interpreted as an ultrafast thermometer with a response time of ∼1 ps, but the restructured water around the solute contributes as well to a smaller extent. While the sub-picosecond solvation of the excited state of the coumarin dye must imply a partial rearrangement of water molecules in the solvation layer, the time scale separation implies that this happens in a way that strain is built up within the solvation layer. Releasing that strain, apparently, requires an essentially complete reorientation of some of the water molecules in the solvation layer, which is why the Debye relaxation time is the relevant time scale. We consider this experiment to be a direct observation of the very non-intuitive time scale separation between solvation time and Debye relaxation [Eq. (1)].

SUPPLEMENTARY MATERIAL

See supplementary material for absorption and fluorescence spectra of the dye (Fig. S1), a measurement of the excited state lifetime (Fig. S2), the THz pulse after transmitting through a thermalized 40 μm water cuvette as a function of temperature (Fig. S3), simulated absorption spectra of TIP4P/2005 water (Fig. S4), the full simulated THz response as a function of both time coordinates t_1 and t_2 (Fig. S5), and the dipole-dipole correlation function of the simulation box (Fig. S6).

ACKNOWLEDGMENTS

The work has been supported by the Swiss National Science Foundation (SNF) through the NCCR MUST as well as Grant No. 200021_165789/1.

[1]T. Azumi, K.-I. Itoh, and I. Hiroshi, J. Chem. Phys. **65**, 2550 (1976).
[2]L. A. Haliidy and M. R. Topp, J. Phys. Chem. **82**, 2415 (1978).
[3]T. Okamura, M. Sumitani, and K. Yoshihara, Chem. Phys. Lett. **94**, 339 (1983).
[4]W. Jarzeba, G. C. Walker, A. E. Johnson, M. A. Kahlow, and P. F. Barbara, J. Phys. Chem. **92**, 7039 (1988).
[5]R. Jimenez, G. R. Fleming, P. V. Kumar, and M. Maroncelli, Nature **369**, 471 (1994).
[6]M. L. Horng, J. A. Gardecki, A. Papazyan, and M. Maroncelli, J. Phys. Chem. **99**, 17311 (1995).
[7]B. Bagchi and B. Jana, Chem. Soc. Rev. **39**, 1936 (2010).
[8]B. Bagchi, D. W. Oxtoby, and G. R. Fleming, Chem. Phys. **86**, 257 (1984).
[9]G. Van der Zwan and J. T. Hynes, J. Phys. Chem. **89**, 4181 (1985).
[10]R. F. Loring and S. Mukamel, J. Chem. Phys. **87**, 1272 (1986).
[11]D. Kivelson and H. Friedman, J. Phys. Chem. **93**, 7026 (1989).
[12]V. I. Arkhipov and N. Agmon, Isr. J. Chem. **43**, 363 (2003).
[13]M. J. Lang, X. J. Jordanides, X. Song, and G. R. Fleming, J. Chem. Phys. **110**, 5884 (1999).
[14]M. Maroncelli and G. R. Fleming, J. Chem. Phys. **89**, 5044 (1988).
[15]M. Maroncelli, J. Chem. Phys. **94**, 2084 (1991).
[16]B. Bagchi, E. W. Castner, and G. R. Fleming, J. Mol. Struct. **194**, 171 (1989).
[17]L. E. Fried and S. Mukamel, J. Chem. Phys. **93**, 932 (1990).
[18]A. Chandra and B. Bagchi, J. Chem. Phys. **94**, 3177 (1991).
[19]T. Fukasawa, T. Sato, J. Watanabe, Y. Hama, W. Kunz, and R. Buchner, Phys. Rev. Lett. **95**, 197802 (2005).
[20]G. Haran, W. D. Sun, K. Wynne, and R. M. Hochstrasser, Chem. Phys. Lett. **274**, 365 (1997).
[21]R. McElroy and K. Wynne, Phys. Rev. Lett. **79**, 3078 (1997).
[22]S. Ebbinghaus, S. J. Kim, M. Heyden, X. Yu, U. Heugen, M. Gruebele, D. M. Leitner, and M. Havenith, Proc. Natl. Acad. Sci. U. S. A. **104**, 20749 (2007).
[23]M. Heyden, E. Bründermann, U. Heugen, G. Niehues, D. M. Leitner, and M. Havenith, J. Am. Chem. Soc. **130**, 5773 (2008).
[24]K. Meister, S. Ebbinghaus, Y. Xu, J. G. Duman, A. DeVries, M. Gruebele, D. M. Leitner, and M. Havenith, Proc. Natl. Acad. Sci. U. S. A. **110**, 1617 (2013).
[25]L. R. Winther, J. Qvist, and B. Halle, J. Phys. Chem. B **116**, 9196 (2012).
[26]M. Heyden, J. Chem. Phys. **141**, 22D509 (2014).
[27]C. Würth, M. Grabolle, J. Pauli, M. Spieles, and U. Resch-Genger, Nat. Protoc. **8**, 1535 (2013).
[28]M. J. Frisch, G. W. Trucks, H. B. Schlegel, G. E. Scuseria, M. A. Robb, J. R. Cheeseman, G. Scalmani, V. Barone, B. Mennucci, G. A. Petersson, H. Nakatsuji, M. Caricato, X. Li, H. P. Hratchian, A. F. Izmaylov, J. Bloino, G. Zheng, J. L. Sonnenberg, M. Hada, M. Ehara, K. Toyota, R. Fukuda, J. Hasegawa, M. Ishida, T. Nakajima, Y. Honda, O. Kitao, H. Nakai, T. Vreven, J. A. Montgomery, Jr., J. E. Peralta, F. Ogliaro, M. Bearpark, J. J. Heyd, E. Brothers, K. N. Kudin, V. N. Staroverov, R. Kobayashi, J. Normand, K. Raghavachari, A. Rendell, J. C. Burant, S. S. Iyengar, J. Tomasi, M. Cossi, N. Rega, J. M. Millam, M. Klene, J. E. Knox, J. B. Cross, V. Bakken, C. Adamo, J. Jaramillo, R. Gomperts, R. E. Stratmann, O. Yazyev, A. J. Austin, R. Cammi, C. Pomelli, J. W. Ochterski, R. L. Martin, K. Morokuma, V. G. Zakrzewski, G. A. Voth, P. Salvador, J. J. Dannenberg, S. Dapprich, A. D. Daniels, O. Farkas, J. B. Foresman, J. V. Ortiz, J. Cioslowski, and D. J. Fox, GAUSSIAN 09, Revision B.01, Gaussian, Inc., Wallingford, CT, 2009.
[29]N. Nemkovich, H. Reis, and W. Baumann, J. Lumin. **71**, 255 (1997).

[30]R. J. Cave and E. W. Castner, J. Phys. Chem. A **106**, 12117 (2002).
[31]R. Kanya and Y. Ohshima, Chem. Phys. Lett. **370**, 211 (2003).
[32]J. Savolainen, S. Ahmed, and P. Hamm, Proc. Natl. Acad. Sci. U. S. A. **110**, 20402 (2013).
[33]S. Ahmed, J. Savolainen, and P. Hamm, Rev. Sci. Instrum. **85**, 013114 (2014).
[34]M. J. Tauber, R. A. Mathies, X. Chen, and S. E. Bradforth, Rev. Sci. Instrum. **74**, 4958 (2003).
[35]P. Hamm, R. A. Kaindl, and J. Stenger, Opt. Lett. **25**, 1798 (2000).
[36]J. Bredenbeck, J. Helbing, and P. Hamm, Rev. Sci. Instrum. **75**, 4462 (2004).
[37]J. L. Abascal and C. Vega, J. Chem. Phys. **123**, 234505 (2005).
[38]D. Van Der Spoel, E. Lindahl, B. Hess, G. Groenhof, A. E. Mark, and H. J. C. Berendsen, J. Comput. Chem. **26**, 1701 (2005).
[39]T. Lian, B. Locke, Y. Kholodenko, and R. M. Hochstrasser, J. Phys. Chem. **98**, 11648 (1994).
[40]H. R. Zelsmann, J. Mol. Struct. **350**, 95 (1995).
[41]A. J. Lock, S. Woutersen, and H. J. Bakker, J. Phys. Chem. A **105**, 1238 (2001).
[42]A. J. Lock and H. J. Bakker, J. Chem. Phys. **117**, 1708 (2002).
[43]A. Pakoulev, Z. Wang, and D. D. Dlott, Chem. Phys. Lett. **371**, 594 (2003).
[44]T. Steinel, J. B. Asbury, J. Zheng, and M. D. Fayer, J. Phys. Chem. A **108**, 10957 (2004).
[45]M. L. Cowan, B. D. Bruner, N. Huse, J. R. Dwyer, B. Chugh, E. T. J. Nibbering, T. Elsaesser, and R. J. D. Miller, Nature **434**, 199 (2005).
[46]L. Piatkowski, K. B. Eisenthal, and H. J. Bakker, Phys. Chem. Chem. Phys. **11**, 9033 (2009).
[47]J. Lindner, P. Vöhringer, M. S. Pshenichnikov, D. Cringus, D. A. Wiersma, and M. Mostovoy, Chem. Phys. Lett. **421**, 329 (2006).
[48]S. T. Van Der Post, C. S. Hsieh, M. Okuno, Y. Nagata, H. J. Bakker, M. Bonn, and J. Hunger, Nat. Commun. **6**, 8384 (2015).
[49]M. Grechko, T. Hasegawa, F. D'Angelo, H. Ito, D. Turchinovich, Y. Nagata, and M. Bonn, Nat. Commun. **9**, 885 (2018).
[50]D. A. Schmidt, S. Funkner, B. P. Born, R. Gnanasekaran, G. W. Schwaab, D. M. Leitner, and M. Havenith, J. Am. Chem. Soc. **131**, 18512 (2009).
[51]D. Chandler, Nature **437**, 640 (2005).
[52]N. T. Southall, K. A. Dill, and A. D. J. Haymet, J. Phys. Chem. **106**, 521 (2002).
[53]K. A. Dill and T. M. Truskett, Annu. Rev. Biophys. Biomol. Struct. **34**, 173 (2005).

Supplementary Material: Aqueous Solvation from the Water Perspective

Saima Ahmed, Andrea Pasti, Ricardo J. Fernández-Terán, Gustavo Ciardi, Andrey Shalit, Peter Hamm
Department of Chemistry, University of Zurich, Zurich, Switzerland

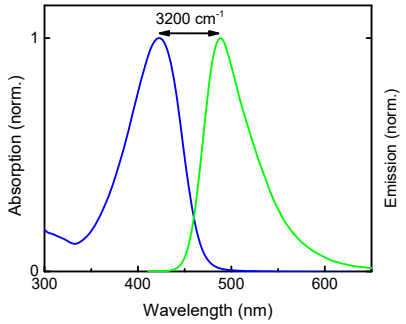

FIG. S1. Normalized absorption (blue) and emission (green) spectra of a solution of deprotonated Coumarin 343 (5 mM) in the presence of 10 mM DABCO in water at room temperature. The Stokes shift, as determined of the peaks of the spectra, is 3200 cm^{-1}.

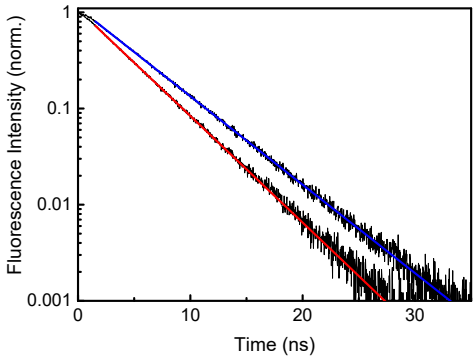

FIG. S2. Fluorescence decay of deprotonated Coumarin 343 in the dilute case (blue) and at the concentration used in the transient THz experiment (red, 5 mM Coumarin 343 and 10 mM DABCO). The data are fit to single exponential functions (thick lines), revealing lifetimes of 4.7 ns and 3.9 ns, respectively.

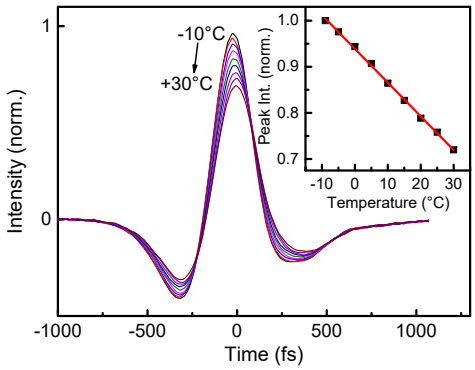

FIG. S3. THz pulse after transmitting through a thermalized 40 μm water cuvette with the temperature varied from -10°C to 30°C in steps of 5°C. The inset shows the peak intensity of the THz pulse together with a linear fit (red line) that reveals a slope of $\Delta T/T = -7.5 \cdot 10^{-3}$ K^{-1}.

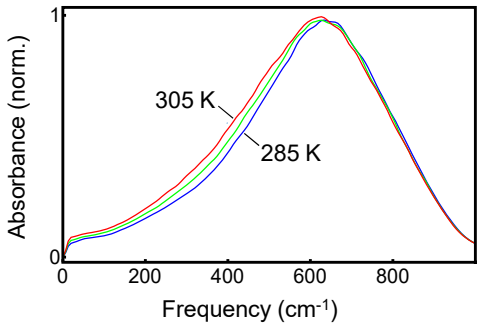

FIG. S4. Normalized THz absorption spectrum of water for the current MD simulation setup with the dipole of the Lennard-Jones sphere set to zero at 285 K (blue), 295 K (green) and 305 K (red). The absorption rise in the 100 cm^{-1} region with temperature results from a red-shift of the librational mode at 600 cm^{-1} due to its anharmonicity, whose wing extends to very low frequencies. This explains why the TIP4P/2005 water model, which as a non-polarizable water model does not reproduce the hydrogen-bond stretching mode at 200 cm^{-1}, still captures the temperature effect reasonably well.

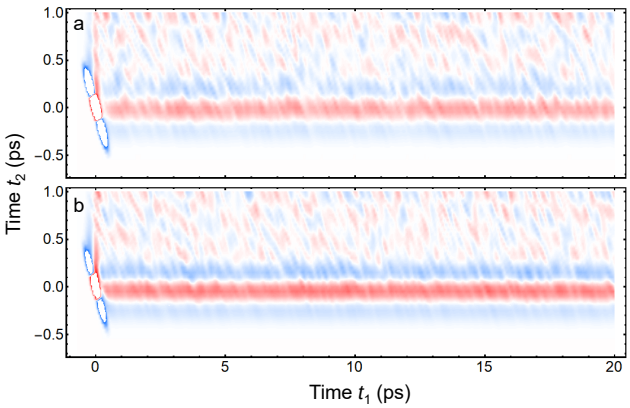

FIG. S5. Full 2D data of the simulation, the result of Eq. 6 along t_1 and t_2 for (a) switching on the dipole of the Lennard Jones sphere and (b) switching if off.

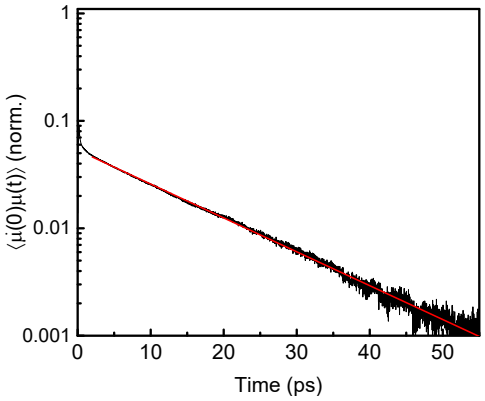

FIG. S6. Dipole-dipole correlation function $\langle\dot{\mu}(0)\mu(t)\rangle$ of water (normalized to the short-time peak, which is not visible on the scale of the plot) for the current MD simulation setup with the dipole of the Lennard-Jones sphere set to zero. An exponential fit of the long-time tail (red line) reveals a Debye relaxation time of 14 ps.

Bibliography

[1] E. P. J. Parrott, Y. Sun, and E. Pickwell-MacPherson, "Terahertz spectroscopy: Its future role in medical diagnoses," *J. Mol. Struct.*, vol. 1006, no. 1, pp. 66 – 76, 2011.

[2] J. E. Bertie and Z. Lan, "Infrared intensities of liquids xx: The intensity of the oh stretching band of liquid water revisited, and the best current values of the optical constants of h2o(l) at 25°c between 15,000 and 1 cm^{-1}," *Appl. Spectrosc.*, vol. 50, no. 8, pp. 1047–1057, 1996.

[3] S. Ahmed, J. Savolainen, and P. Hamm, "Detectivity enhancement in thz electrooptical sampling," *Review of Scientific Instruments*, vol. 85, no. 1, p. 013114, 2014.

[4] A. Shalit, S. Ahmed, and P. Hamm, "Terahertz echoes reveal the inhomogeneity of aqueous salt solutions," *Nat. Chem.*, vol. 9, p. 273–278, 2017.

[5] K. R. Harris and L. A. Woolf, "Temperature and volume dependence of the viscosity of water and heavy water at low temperatures," *Journal of Chemical & Engineering Data*, vol. 49, no. 4, pp. 1064–1069, 2004.

[6] A. Dehaoui, B. Issenmann, and F. Caupin, "Viscosity of deeply supercooled water and its coupling to molecular diffusion," *P.N.A.S.*, vol. 112, no. 39, pp. 12020–12025, 2015.

[7] A. I. Kudish, D. Wolf, and F. Steckel, "Physical properties of oxygen-17

water. absolute viscosity and density of h217o between 15 and 35°c," *J. Chem. Soc., Faraday Trans. 1*, vol. 70, pp. 484–489, 1974.

[8] M. Afsar, J. Hasted, M. Zafar, and J. Chamberlain, "Absorption bands in liquid chloroform and bromoform," *Chem. Phys. Lett.*, vol. 36, no. 1, pp. 69 – 72, 1975.

[9] C. Yu, S. Fan, Y. Sun, and E. Pickwell-Macpherson, "The potential of terahertz imaging for cancer diagnosis: A review of investigations to date," *Quant Imaging Med Surg*, vol. 2, pp. 2223–4306, 2012.

[10] D. Markl, M. T. Ruggiero, and J. A. Zeitler, "Pharmaceutical applications of terahertz spectroscopy and imaging," *European Pharmaceutical Review*, vol. 21, pp. 45–50, 2016.

[11] N. Palka, M. Kowalski, R. Ryniec, M. Szustakowski, and E. Czerwińska, "Thz screening for civil and military security," in *THz and Security Applications*, pp. 211–228, Springer Netherlands, 2014.

[12] T. Bardon, R. K. May, P. F. Taday, and M. Strlič, "Systematic study of terahertz time-domain spectra of historically informed black inks," *Analyst*, vol. 138, pp. 4859–4869, 2013.

[13] L. Xu, X. Zhang, and D. H. Auston, "Terahertz beam generation by femtosecond optical pulses in electro-optic materials," *Applied Physics Letters*, vol. 61, no. 15, pp. 1784–1786, 1992.

[14] P. Kilcullen, I. D. Hartley, E. T. Jensen, and M. Reid, "Terahertz time domain gas-phase spectroscopy of carbon monoxide," *Journal of Infrared, Millimeter, and Terahertz Waves*, vol. 36, no. 4, pp. 380–389, 2015.

[15] R. M. Smith and M. A. Arnold, "Selectivity of terahertz gas-phase spectroscopy," *Analytical Chemistry*, vol. 87, no. 21, pp. 10679–10683, 2015.

[16] D. Grischkowsky, S. Keiding, M. van Exter, and C. Fattinger, "Far-infrared time-domain spectroscopy with terahertz beams of dielectrics and semiconductors," *J. Opt. Soc. Am. B*, vol. 7, no. 10, pp. 2006–2015, 1990.

[17] K. Meister, S. Ebbinghaus, Y. Xu, J. G. Duman, A. DeVries, M. Gruebele, D. M. Leitner, and M. Havenith, "Long-range protein–water dynamics in hyperactive insect antifreeze proteins," *Proc. Natl. Acad. Sci. U.S.A.*, vol. 110, no. 5, pp. 1617–1622, 2013.

[18] T. Fukasawa, T. Sato, J. Watanabe, Y. Hama, W. Kunz, and R. Buchner, "Relation between dielectric and low-frequency Raman spectra of hydrogen-bond liquids," *Phys. Rev. Lett.*, vol. 95, p. 197802, 2005.

[19] B. M. Fischer, M. Walther, and P. U. Jepsen, "Far-infrared vibrational modes of DNA components studied by terahertz time-domain spectroscopy," *Physics in Medicine and Biology*, vol. 47, no. 21, pp. 3807–3814, 2002.

[20] P. Hamm, M. Meuwly, S. L. Johnson, P. Beaud, and U. Staub, "Perspective: Thz-driven nuclear dynamics from solids to molecules," *Struct. Dyn.*, vol. 4, no. 6, p. 061601, 2017.

[21] J. R. Ferraro and K. Nakamoto, *Introductory Raman Spectroscopy (Second Edition)*. Academic Press, 2003.

[22] S. Colaianni and O. Nielsen, "Low-frequency raman spectroscopy," *J. Mol. Struct.*, vol. 347, pp. 267 – 283, 1995.

[23] L. A. Blatz, *Low-Frequency Raman Spectra of Liquids*, pp. 121–140. Springer US, 1970.

[24] T. Ford, "Infrared and Raman spectra and vibrational assignments of diiodomethane and its deuterated analogs," *J. Mol. Spectrosc.*, vol. 58, no. 2, pp. 185 – 193, 1975.

[25] I. A. Heisler and S. R. Meech, "Low-frequency modes of aqueous alkali halide solutions: Glimpsing the hydrogen bonding vibration," *Science*, vol. 327, no. 5967, pp. 857–860, 2010.

[26] C. J. Fecko, J. D. Eaves, and A. Tokmakoff, "Isotropic and anisotropic raman scattering from molecular liquids measured by spatially masked optical Kerr effect spectroscopy," *J. Chem. Phys*, vol. 117, no. 3, pp. 1139–1154, 2002.

[27] B. J. Loughnane, A. Scodinu, R. A. Farrer, J. T. Fourkas, and U. Mohanty, "Exponential intermolecular dynamics in optical Kerr effect spectroscopy of small-molecule liquids," *J. Chem. Phys.*, vol. 111, no. 6, pp. 2686–2694, 1999.

[28] D. F. Plusquellic, K. Siegrist, E. J. Heilweil, and O. Esenturk, "Applications of terahertz spectroscopy in biosystems," *ChemPhysChem*, vol. 8, no. 17, pp. 2412–2431, 2007.

[29] P. Hamm and M. Zanni, *Concepts and methods of 2D infrared spectrsocopy*. Cambridge University Press, Cambridge, 2011.

[30] R. Ernst, G. Bodenhausen, and A. Wokaun, *Principles of Nuclear Magnetic Resonance in One and Two Dimensions*. Clarendon Press, Oxford, 1987.

[31] P. Hamm, M. Lim, and R. M. Hochstrasser, "Structure of the amide i band of peptides measured by femtosecond nonlinear-infrared spectroscopy," *J. Phys. Chem. B*, vol. 102, no. 31, pp. 6123–6138, 1998.

[32] O. Golonzka, M. Khalil, N. Demirdöven, and A. Tokmakoff, "Coupling and orientation between anharmonic vibrations characterized with two-dimensional infrared vibrational echo spectroscopy," *J. Chem. Phys.*, vol. 115, no. 23, pp. 10814–10828, 2001.

[33] D. E. Thompson, K. Merchant, and M. Fayer, "Solute–solvent interactions: two-dimensional ultrafast infrared vibrational echo experiments," *Chem. Phys. Lett.*, vol. 340, no. 3, pp. 267 – 274, 2001.

[34] S. Mukamel, *Principles of Nonlinear optical spectroscopy.* Oxford University Press, 1995.

[35] T. Elsaesser, K. Reimann, and M. Woerner, *Concepts and Applications of Nonlinear Terahertz Spectroscopy.* Morgan and Claypool Publishers, 2019.

[36] Y. Tanimura and S. Mukamel, "Two-dimensional femtosecond vibrational spectroscopy of liquids," *J. Chem. Phys.*, vol. 99, no. 12, pp. 9496–9511, 1993.

[37] T. Kampfrath, K. Tanaka, and K. A. Nelson, "Resonant and nonresonant control over matter and light by intense terahertz transients," *Nat. Photonics*, vol. 7, p. 680, 2013.

[38] W. Kuehn, K. Reimann, M. Woerner, and T. Elsaesser, "Phase-resolved two-dimensional spectroscopy based on collinear n-wave mixing in the ultrafast time domain," *J. Chem. Phys.*, vol. 130, no. 16, p. 164503, 2009.

[39] W. Kuehn, K. Reimann, M. Woerner, T. Elsaesser, and R. Hey, "Two-dimensional terahertz correlation spectra of electronic excitations in semiconductor quantum wells," *J. Phys. Chem. B*, vol. 115, no. 18, pp. 5448–5455, 2011.

[40] J. Lu, Y. Zhang, H. Y. Hwang, B. K. Ofori-Okai, S. Fleischer, and K. A. Nelson, "Nonlinear two-dimensional terahertz photon echo and rotational spectroscopy in the gas phase," *Proc. Natl. Acad. Sci. U.S.A.*, vol. 113, no. 42, pp. 11800–11805, 2016.

[41] C. Somma, G. Folpini, K. Reimann, M. Woerner, and T. Elsaesser, "Phase-resolved two-dimensional terahertz spectroscopy including off-resonant interactions beyond the $\chi(3)$ limit," *J. Chem. Phys.*, vol. 144, no. 18, p. 184202, 2016.

[42] P. Hamm and A. Shalit, "Perspective: Echoes in 2d-Raman-THz spectroscopy," *J. Chem. Phys.*, vol. 146, no. 13, p. 130901, 2017.

[43] J. T. Fourkas, *Multidimensional raman spectroscopy*, pp. 235–274. John Wiley and Sons, Ltd.

[44] L. J. Muller, D. Vanden Bout, and M. Berg, "Broadening of vibrational lines by attractive forces: Ultrafast raman echo experiments in a ch3i:cdcl3 mixture," *J. Chem. Phys.*, vol. 99, no. 2, pp. 810–819, 1993.

[45] D. Vanden Bout, L. J. Muller, and M. Berg, "Ultrafast raman echoes in liquid acetonitrile," *Phys. Rev. Lett.*, vol. 67, pp. 3700–3703, 1991.

[46] A. Tokmakoff, M. J. Lang, D. S. Larsen, G. R. Fleming, V. Chernyak, and S. Mukamel, "Two-dimensional raman spectroscopy of vibrational interactions in liquids," *Phys. Rev. Lett.*, vol. 79, pp. 2702–2705, 1997.

[47] O. Golonzka, N. Demirdöven, M. Khalil, and A. Tokmakoff, "Separation of cascaded and direct fifth-order Raman signals using phase-sensitive intrinsic heterodyne detection," *J. Chem. Phys.*, vol. 113, no. 22, pp. 9893–9896, 2000.

[48] D. A. Blank, L. J. Kaufman, and G. R. Fleming, "Direct fifth-order electronically nonresonant Raman scattering from CS_2 at room temperature," *J. Chem. Phys.*, vol. 113, no. 2, pp. 771–778, 2000.

[49] K. Kubarych, C. Milne, and R. Miller, "Heterodyne detected fifth-order raman response of liquid cs2: 'Dutch Cross' polarization," *Chem. Phys. Lett.*, vol. 369, no. 5, pp. 635 – 642, 2003.

[50] Y. L. Li, L. Huang, R. J. Dwayne Miller, T. Hasegawa, and Y. Tanimura, "Two-dimensional fifth-order raman spectroscopy of liquid formamide: Experiment and Theory," *J. Chem. Phys.*, vol. 128, no. 23, p. 234507, 2008.

[51] H. Frostig, T. Bayer, N. Dudovich, Y. C. Eldar, and Y. Silberberg, "Single-beam spectrally controlled two-dimensional Raman spectroscopy," *Nat. Photonics*, 2015.

[52] J. Lu, X. Li, Y. Zhang, H. Y. Hwang, B. K. Ofori-Okai, and K. A. Nelson, "Two-dimensional spectroscopy at terahertz frequencies," *Topics in Current Chemistry*, vol. 376, 2018.

[53] M. Cho, "Two-dimensional vibrational spectroscopy. iii. theoretical description of the coherent two-dimensional ir-raman spectroscopy for the investigation of the coupling between both ir- and raman-active vibrational modes," *The Journal of Chemical Physics*, vol. 111, no. 9, pp. 4140–4147, 1999.

[54] P. Hamm and J. Savolainen, "Two-dimensional-Raman-terahertz spectroscopy of water: Theory," *J. Chem. Phys.*, vol. 136, no. 9, p. 094516, 2012.

[55] J. Savolainen, S. Ahmed, and P. Hamm, "Two-dimensional Raman-terahertz spectroscopy of water," *PNAS*, vol. 110, no. 51, pp. 20402–20407, 2013.

[56] M. A. Allodi, I. A. Finneran, and G. A. Blake, "Nonlinear terahertz coherent excitation of vibrational modes of liquids," *J. Chem. Phys.*, vol. 143, no. 23, p. 234204, 2015.

[57] M. C. Hoffmann, N. C. Brandt, H. Y. Hwang, K.-L. Yeh, and K. A. Nelson, "Terahertz Kerr effect," *Appl. Phys. Lett.*, vol. 95, no. 23, 2009.

[58] T. Kampfrath, R. K. Campen, M. Wolf, and M. Sajadi, "The nature of the dielectric response of methanol revealed by the terahertz Kerr effect," *J. Phys. Chem. Lett.*, vol. 9, no. 6, pp. 1279–1283, 2018.

[59] M. Sajadi, M. Wolf, and T. Kampfrath, "Transient birefringence of liquids induced by terahertz electric-field torque on permanent molecular dipoles," *Nat. Commun.*, vol. 8, no. 14963, 2017.

[60] I. A. Finneran, R. Welsch, M. A. Allodi, T. F. Miller, and G. A. Blake, "Coherent two-dimensional terahertz-terahertz-raman spectroscopy," *PNAS*, vol. 113, no. 25, pp. 6857–6861, 2016.

[61] I. A. Finneran, R. Welsch, M. A. Allodi, T. F. Miller, and G. A. Blake, "2d THz-THz-raman photon-echo spectroscopy of molecular vibrations in liquid bromoform," *J. Phys. Chem. Letter*, vol. 8, no. 18, pp. 4640–4644, 2017.

[62] I. Wilke and S. Sengupta, "Nonlinear optical techniques for terahertz pulse generation and detection—optical rectification and electrooptic sampling," in *Terahertz Spectroscopy: Principles and Applications*, pp. 41–73, CRC Press, 2007.

[63] M. Bass, P. A. Franken, J. F. Ward, and G. Weinreich, "Optical rectification," *Phys. Rev. Lett.*, vol. 9, pp. 446–448, Dec 1962.

[64] A. Rice, Y. Jin, X. F. Ma, X. Zhang, D. Bliss, J. Larkin, and M. Alexander, "Terahertz optical rectification from 110 zinc-blende crystals," *Applied Physics Letters*, vol. 64, no. 11, pp. 1324–1326, 1994.

[65] P. C. M. Planken, H.-K. Nienhuys, H. J. Bakker, and T. Wenckebach, "Measurement and calculation of the orientation dependence of terahertz pulse detection in znte," *J. Opt. Soc. Am. B*, vol. 18, no. 3, pp. 313–317, 2001.

[66] C. A. Schmuttenmaer, "Exploring dynamics in the far-infrared with terahertz spectroscopy," *Chem. Rev.*, vol. 104, no. 4, pp. 1759–1780, 2004.

[67] S. Ahmed, J. Savolainen, and P. Hamm, "The effect of the gouy phase in optical-pump-thz-probe spectroscopy," *Opt. Express*, vol. 22, no. 4, pp. 4256–4266, 2014.

[68] A. Berger, G. Ciardi, D. Sidler, P. Hamm, and A. Shalit, "Impact of nuclear quantum effects on the structural inhomogeneity of liquid water," *PNAS*, 2019.

[69] G. Ciardi, A. Berger, P. Hamm, and A. Shalit, "Signatures of intra- and intermolecular vibrational coupling in halogenated liquids revealed

by two-dimensional raman-terahertz spectroscopy," *The Journal of Physical Chemistry Letters*, pp. 4463–4468, 2019.

[70] S. M. Teo, B. K. Ofori-Okai, C. A. Werley, and K. A. Nelson, "Invited article: Single-shot thz detection techniques optimized for multidimensional thz spectroscopy," *Rev. Scient. Instr.*, vol. 86, no. 5, p. 051301, 2015.

[71] E. L. Hahn, "Spin echoes," *Phys. Rev.*, vol. 80, pp. 580–594, 1950.

[72] A. Tokmakoff and M. D. Fayer, "Homogeneous vibrational dynamics and inhomogeneous broadening in glass-forming liquids: Infrared photon echo experiments from room temperature to 10 k," *The Journal of Chemical Physics*, vol. 103, no. 8, pp. 2810–2826, 1995.

[73] W. P. de Boeij, M. S. Pshenichnikov, and D. A. Wiersma, "Ultrafast solvation dynamics explored by femtosecond photon echo spectroscopies," *Annual Review of Physical Chemistry*, vol. 49, no. 1, pp. 99–123, 1998.

[74] W. N. Baker, "A new comparison of the viscosity of d2o with that of h2o," *J. Chem. Phys.*, vol. 4, no. 4, pp. 294–295, 1936.

[75] M. Ceriotti, W. Fang, P. G. Kusalik, R. H. McKenzie, A. Michaelides, M. A. Morales, and T. E. Markland, "Nuclear quantum effects in water and aqueous systems: Experiment, theory, and current challenges," *Chemical Reviews*, vol. 116, no. 13, pp. 7529–7550, 2016.

[76] P. G. Debenedetti, "Supercooled and glassy water," *Journal of Physics: Condensed Matter*, vol. 15, no. 45, pp. R1669–R1726, 2003.

[77] A. Nilsson and L. G. M. Pettersson, "The structural origin of anomalous properties of liquid water," *Nat. Commun.*, vol. 6, p. 8998, 2015.

[78] F. Steckel and S. Szapiro, "Physical properties of heavy oxygen water. part 1.—density and thermal expansion," *Trans. Faraday Soc.*, vol. 59, pp. 331–343, 1963.

[79] C. H. Cho, J. Urquidi, S. Singh, and G. W. Robinson, "Thermal offset viscosities of liquid h2o, d2o, and t2o," *J. Phys. Chem. B*, vol. 103, no. 11, pp. 1991–1994, 1999.

[80] K. R. Harris, "Isotope effects and the thermal offset effect for diffusion and viscosity coefficients of liquid water," *Phys. Chem. Chem. Phys.*, vol. 4, pp. 5841–5845, 2002.

[81] R. T. Hart, C. J. Benmore, J. Neuefeind, S. Kohara, B. Tomberli, and P. A. Egelstaff, "Temperature dependence of isotopic quantum effects in water," *Phys. Rev. Lett.*, vol. 94, p. 047801, Feb 2005.

[82] A. K. Soper and C. J. Benmore, "Quantum differences between heavy and light water," *Phys. Rev. Lett.*, vol. 101, p. 065502, 2008.

[83] S. Habershon, T. E. Markland, and D. E. Manolopoulos, "Competing quantum effects in the dynamics of a flexible water model," *J. Chem. Phys.*, vol. 131, no. 2, p. 024501, 2009.

[84] K. Röttger, A. Endriss, J. Ihringer, S. Doyle, and W. F. Kuhs, "Lattice constants and thermal expansion of H_2O and D_2O ice I*h* between 10 and 265 K," *Acta Cryst.*, vol. 50, no. 6, pp. 644–648, 1994.

[85] B. Pamuk, J. M. Soler, R. Ramírez, C. P. Herrero, P. W. Stephens, P. B. Allen, and M.-V. Fernández-Serra, "Anomalous nuclear quantum effects in ice," *Phys. Rev. Lett.*, vol. 108, p. 193003, 2012.

[86] B. Pamuk, P. B. Allen, and M.-V. Fernández-Serra, "Insights into the structure of liquid water from nuclear quantum effects on the density and compressibility of ice polymorphs," *J. Phys. Chem. B*, vol. 122, no. 21, pp. 5694–5706, 2018.

[87] T. E. Markland and B. J. Berne, "Unraveling quantum mechanical effects in water using isotopic fractionation," *P.N.A.S.*, vol. 109, no. 21, pp. 7988–7991, 2012.

[88] D. Chandler, *Introduction to Modern Statistical Mechanics*. Oxford University Press, 1987.

[89] R. A. Kuharski and P. J. Rossky, "A quantum mechanical study of structure in liquid h2o and d2o," *J. Chem. Phys.*, vol. 82, no. 11, pp. 5164–5177, 1985.

[90] G. S. Fanourgakis, G. K. Schenter, and S. S. Xantheas, "A quantitative account of quantum effects in liquid water," *J. Chem. Phys.*, vol. 125, no. 14, p. 141102, 2006.

[91] F. Paesani, S. Iuchi, and G. A. Voth, "Quantum effects in liquid water from an ab initio-based polarizable force field," *J. Chem. Phys.*, vol. 127, no. 7, p. 074506, 2007.

[92] P. Hamm, G. S. Fanourgakis, and S. S. Xantheas, "A surprisingly simple correlation between the classical and quantum structural networks in liquid water," *J. Chem. Phys.*, vol. 147, no. 6, p. 064506, 2017.

[93] K. H. Kim, H. Pathak, A. Späh, F. Perakis, D. Mariedahl, J. A. Sellberg, T. Katayama, Y. Harada, H. Ogasawara, L. G. M. Pettersson, and A. Nilsson, "Temperature-independent nuclear quantum effects on the structure of water," *Phys. Rev. Lett.*, vol. 119, p. 075502, 2017.

[94] C. Rønne, P.-O. Åstrand, and S. R. Keiding, "Thz spectroscopy of liquid H_2o and D_2o," *Phys. Rev. Lett.*, vol. 82, pp. 2888–2891, 1999.

[95] H. J. Bakker, Y. L. A. Rezus, and R. L. A. Timmer, "Molecular reorientation of liquid water studied with femtosecond midinfrared spectroscopy," *J. Phys. Chem. B A*, vol. 112, no. 46, pp. 11523–11534, 2008.

[96] F. Paesani, S. S. Xantheas, and G. A. Voth, "Infrared spectroscopy and hydrogen-bond dynamics of liquid water from centroid molecular dynamics with an ab initio-based force field," *J. Phys. Chem. B*, vol. 113, no. 39, pp. 13118–13130, 2009.

[97] F. Paesani, S. Yoo, H. J. Bakker, and S. S. Xantheas, "Nuclear quantum effects in the reorientation of water," *J. Phys. Chem. Lett.*, vol. 1, no. 15, pp. 2316–2321, 2010.

[98] D. M. Wilkins, D. E. Manolopoulos, S. Pipolo, D. Laage, and J. T. Hynes, "Nuclear quantum effects in water reorientation and hydrogen-bond dynamics," *J. Phys. Chem. Lett.*, vol. 8, no. 12, pp. 2602–2607, 2017.

[99] Y. Amo and Y. Tominaga, "Low-frequency raman study of water isotopes," *Physica A: Statistical Mechanics and its Applications*, vol. 276, no. 3, pp. 401 – 412, 2000.

[100] R. F. Loring and S. Mukamel, "Selectivity in coherent transient raman measurements of vibrational dephasing in liquids," *J. Chem. Phys.*, vol. 83, no. 5, pp. 2116–2128, 1985.

[101] J. B. Asbury, T. Steinel, K. Kwak, S. A. Corcelli, C. P. Lawrence, J. L. Skinner, and M. D. Fayer, "Dynamics of water probed with vibrational echo correlation spectroscopy," *J. Chem. Phys.*, vol. 121, no. 24, pp. 12431–12446, 2004.

[102] W. D. Yeremenko S, Pshenichnikov MS, "Hydrogen-bond dynamics in water explored by heterodyne-detected," *Chem. Phys. Lett.*, vol. 369, no. 1, pp. 107 – 113, 2003.

[103] M. L. e. a. Cowan, "Ultrafast memory loss and energy redistribution in the hydrogen bond network of liquid h2o," *Nature*, 2005.

[104] J. D. Eaves, J. J. Loparo, C. J. Fecko, S. T. Roberts, A. Tokmakoff, and P. L. Geissler, "Hydrogen bonds in liquid water are broken only fleetingly," *P.N.A.S.*, vol. 102, no. 37, pp. 13019–13022, 2005.

[105] F. Perakis, S. Widmer, and P. Hamm, "Two-dimensional infrared spectroscopy of isotope-diluted ice ih," *J. Chem. Phys.*, vol. 134, no. 20, p. 204505, 2011.

[106] M. Grechko, T. Hasegawa, F. D'Angelo, H. Ito, D. Turchinovich, Y. Nagata, and M. Bonn, "Coupling between intra- and intermolecular motions in liquid water revealed by two-dimensional terahertz-infrared-visible spectroscopy," *Nat. Communication*, vol. 9, no. 885, 2018.

[107] S. Palese, S. Mukamel, R. J. D. Miller, and W. T. Lotshaw, "Interrogation of vibrational structure and line broadening of liquid water by raman-induced kerr effect measurements within the multimode brownian oscillator model," *J. Phys. Chem.*, vol. 100, no. 24, pp. 10380–10388, 1996.

[108] D. Sidler and P. Hamm, "Feynman diagram description of 2d-raman-thz spectroscopy applied to water," *The Journal of Chemical Physics*, vol. 150, no. 4, p. 044202, 2019.

[109] P. Hamm, "2d-raman-thz spectroscopy: A sensitive test of polarizable water models," *J. Chem. Phys.*, vol. 141, no. 18, p. 184201, 2014.

[110] T. Steffen and K. Duppen, "Population relaxation and non-markovian frequency fluctuations in third- and fifth-order raman scattering," *Chemical Physics*, vol. 233, no. 2, pp. 267 – 285, 1998.

[111] D. Laage and J. T. Hynes, "A molecular jump mechanism of water reorientation," *Science*, vol. 311, no. 5762, pp. 832–835, 2006.

[112] Z. Sun, L. Zheng, M. Chen, M. L. Klein, F. Paesani, and X. Wu, "Electron-hole theory of the effect of quantum nuclei on the x-ray absorption spectra of liquid water," *Phys. Rev. Lett.*, vol. 121, p. 137401, 2018.

[113] T. Hasegawa and Y. Tanimura, "Calculating fifth-order raman signals for various molecular liquids by equilibrium and nonequilibrium hybrid molecular dynamics simulation algorithms," *J. Chem. Phys.*, vol. 125, no. 7, p. 074512, 2006.

[114] A. Taschin, P. Bartolini, R. Eramo, R. Righini, and R. Torre, "Evidence of two distinct local structures of water from ambient to supercooled conditions," *Nature Communications*, vol. 4, p. 2401, Sep 2013.

[115] R. Torre, P. Bartolini, and R. Righini, "Structural relaxation in supercooled water by time-resolved spectroscopy," *Nature*, vol. 428, pp. 296–299, 2004.

[116] S. Ahmed, A. Pasti, R. J. Fernández-Terán, G. Ciardi, A. Shalit, and P. Hamm, "Aqueous solvation from the water perspective," *J. Chem. Phys.*, vol. 148, no. 23, p. 234505, 2018.

[117] M. Sajadi, M. Wolf, and T. Kampfrath, "Terahertz-field-induced optical birefringence in common window and substrate materials," *Opt. Express*, vol. 23, no. 22, pp. 28985–28992, 2015.

[118] B. Bagchi and B. Jana, "Solvation dynamics in dipolar liquids," *Chem. Soc. Rev.*, vol. 39, pp. 1936–1954, 2010.

[119] M. L. Horng, J. A. Gardecki, A. Papazyan, and M. Maroncelli, "Subpicosecond measurements of polar solvation dynamics: Coumarin 153 revisited," *J. Phys. Chem.*, vol. 99, no. 48, pp. 17311–17337, 1995.

[120] P. Hamm, M. Lim, and R. M. Hochstrasser, "Non-markovian dynamics of the vibrations of ions in water from femtosecond infrared three-pulse photon echoes," *Phys. Rev. Lett.*, vol. 81, pp. 5326–5329, 1998.

[121] H. Shirota and T. Kato, "Intermolecular vibrational spectra of C3v CXY3 molecular liquids, $CHCl_3$, $CHBr_3$, $CFBr_3$, and $CBrCl_3$," *J. Phys. Chem. A*, vol. 115, no. 32, pp. 8797–8807, 2011.

[122] N. T. Hunt, A. A. Jaye, and S. R. Meech, "Ultrafast dynamics in complex fluids observed through the ultrafast optically-heterodyne-detected optical-Kerr-effect (ohd-oke)," *Phys. Chem. Chem. Phys.*, vol. 9, pp. 2167–2180, 2007.

[123] P. P. Wiewiór, H. Shirota, and E. W. Castner, "Aqueous dimethyl sulfoxide solutions: inter- and intra-molecular dynamics," *J. Chem. Phys.*, vol. 116, no. 11, pp. 4643–4654, 2002.

[124] Q. Zhong and J. T. Fourkas, "Optical kerr effect spectroscopy of simple liquids," *J. Phys. Chem. B*, vol. 112, no. 49, pp. 15529–15539, 2008.

[125] M. Davies, G. W. F. Pardoe, J. E. Chamberlain, and H. A. Gebbie, "Character of absorption in far infra-red by polar molecules in liquid state," *Trans. Faraday Soc.*, vol. 64, pp. 847–860, 1968.

[126] M. P. Fernández-Liencres, A. Navarro, J. J. López, M. Fernández, V. Szalay, T. de los Arcos, J. V. García-Ramos, and R. M. Escribano, "The force field of bromoform:a theoretical and experimental investigation," *J. Phys. Chem.*, vol. 100, no. 40, pp. 16058–16065, 1996.

[127] K. Y. Kim, J. H. Glownia, A. J. Taylor, and G. Rodriguez, "Terahertz emission from ultrafast ionizing air in symmetry-broken laser fields," *Opt. Express*, vol. 15, no. 8, pp. 4577–4584, 2007.

[128] H. A. Hafez, X. Chai, A. Ibrahim, S. Mondal, D. Férachou, X. Ropagnol, and T. Ozaki, "Intense terahertz radiation and their applications," *J. Opt.*, vol. 18, no. 9, 2016.

Acknowledgments

This 5 years long journey at the University of Zurich have been crucial for my personal growth, giving me an incredible opportunity to gain insight for the future of my life and career.

The first person I want to acknowledge is my mentor, Prof. Dr. Peter Hamm. I have learned a lot from him over the years, both from his incredible scientific culture and his experienced way of dealing with problems of any sort. The thing I have appreciated the most is the direct, yet thoughtful and open, approach with which he communicates and relates to people. From the scientific perspective, the message he has always put forward is that high-quality research needs patience and that one can always learn something useful also from 'unsuccesful' (which in this context just means 'unpublished') attempts: as he often used to say "We learn what we can learn".

The everyday practical support of Dr. Jan Helbing has been incredibly valuable: his help and friendliness have made things run smoothly in every aspect of the routine lab life in the whole K floor.

I want to give a special thank the two people I have spent more time with throughout my time at UZH: Dr. Andrey Shalit and Arian Berger. We have been a great team together and we have managed to pull out great results from a very, using an understatement, challenging experiment. Even in moments when things were not going as intended and was it hard to keep the motivation high, we kept fighting and always found a way through.

Arian, in particular, has become much more than a colleague: it is now a real friend with whom I have shared many of the best moments of my Swiss

experience. He took me to unforgettable climbing and skiing adventures and I am looking forward to enjoying many more of them even if we don't share the same lab anymore.

Thanks also to Jabbar and all the newcomers that will come and take the legacy of the Raman-THz experiment: I am sure we the future is bright!

It has been a lot of fun to share these years with all the members (past present and future) of the Hamm group. Working and spending time off work with you all has been a really fun and enriching experience that I will certainly remember for a long time.

A huge acknowledgment also to all the staff members of UZH, especially the human resources and technicians, that makes this huge machine running as smooth as it can. A special thank goes to Roland Zehnder, whose incredible and efficient efforts in the workshop make possible almost all the research going on in the group.

The CMSZH graudate school, with all the activities (brilliant retreats, aperos, doktorandentag) and its valuable financial support, has proven itself to be a great tool to establish enthusiasms and promote an enjoyable atmosphere among the PhD students at the department of chemistry. It has been a pleasure to be one of your members!

Last but far from being the least, I want to thank my family and my girlfriend: Luca, Carla, Sofia and Francesca. You were, are and will be the best team I could wish for: few words can't be enough to describe what your support and your love means to me. My deepest gratitude to you.